ABSTRACT

Title of Dissertation: MEASUREMENT OF THE STRANGE MAGNETIC FORM FACTOR OF THE PROTON USING ELASTIC ELECTRON SCATTERING

Damon T. Spayde, Doctor of Philosophy, 2001

Dissertation directed by: Professor Elizabeth J. Beise
Department of Physics

The SAMPLE experiment at the MIT-Bates Linear Accelerator Center measured the elastic $\vec{e}$-p cross section asymmetry A_p and the quasielastic $\vec{e}$-d cross section asymmetry A_d at a Q^2 of 0.1 (GeV/c)^2. The strange magnetic form factor of the nucleon G_M^s has been extracted from this data in a way that is relatively insensitive to electroweak radiative corrections. This form factor constitutes a probe of the strange quark contributions to the nucleon's magnetic moment, and of the low energy properties of the quark-antiquark sea.

MEASUREMENT OF THE STRANGE MAGNETIC FORM FACTOR OF THE PROTON USING ELASTIC ELECTRON SCATTERING

by

Damon T. Spayde

Dissertation submitted to the Faculty of the Graduate School of the
University of Maryland, College Park in partial fulfillment
of the requirements for the degree of
Doctor of Philosophy
2001

Advisory Committee:

Professor Elizabeth J. Beise, Chairperson/Advisor
Doctor Herbert Breuer
Professor Thomas D. Cohen
Professor Wendell T. Hill, III
Professor Philip G. Roos

DEDICATION

To my wife Jessica

ACKNOWLEDGEMENTS

There are many people whom I should thank for helping me get to this point in my life. My parents, Ted and Ruth, and my brother Kirby have provided a wonderful, loving environment in which to grow and pursue goals; I will be forever grateful for that. I also wish to thank the relatives on both sides of my family tree, Spaydes and Cheffeys, as well as my in-laws, the Henrys. They may not completely understand what I do for a living, but they have always been supportive and encouraging.

From my primary and secondary education in the Fayette school district to my undergraduate days at Grinnell College to my graduate career at the University of Maryland there have been many excellent teachers who have inspired me to continue my education; they must have been pretty good at their jobs to keep me in school for 22 years, I thank them for that. In all phases of my life I have enjoyed the companionship of good friends, though they are not listed here I think of them often with gratitude.

I have truly enjoyed my time as a graduate student at the University of Maryland, College Park and this is due in no small part to the group of people that I have primarily interacted with, the faculty, staff, and students of the Experimental Nuclear Physics group. Betsy Beise, Herbert Breuer, Nick Chant, George

Chang, Jim Kelly, and Phil Roos are all people with whom I have enjoyed eating lunch and socializing. The group would not be able to function without Judy Myrick to keep everyone and everything in line. Many students, graduate and undergraduate, have been in the group during my time here and I am very happy to have known them all: Andrés Collinucci, Chad Galley, Kenneth Gustafsson, Mary Claire Herda, Chafiq Halli, Tanja Horn, Jianglai Liu, Rick Mohring, Jesse Stone, Nikolai Savvinov, and Doug Strachan. In particular I would like to express my appreciation to Rick and Kenneth who I consider to be two of the best friends I have ever had. Thanks for everything guys.

I would like to thank the members of my doctoral defense committee for the time they spent reading this work. In particular I appreciate the excellent job Betsy did of proofreading it three times. Herbert also did a meticulous job of editing, resulting in a much improved final document.

My advisor, Betsy, has been teacher, mentor, and friend throughout my five years at Maryland. It has been a pleasure to work with her on SAMPLE and I appreciate the opportunity she has given me to travel to Boston for extended periods of time and to other exotic locales. She has been very understanding of the demands of life outside of physics and has allowed me to work where and when I have needed to. Thank you Betsy.

I wish to thank my fellow collaborators on the SAMPLE experiment, the finest group of people that I have ever had the opportunity to work with; they

are all top-notch physicists as well as being good people. I would particularly like to thank Bob McKeown and Doug Beck for allowing me to use data from their experiment for my dissertation. In all collaborations, the graduate students play a very important role in keeping the experiment running from day to day; my appreciation goes to Silviu Covrig, Joe DelCorso, Richard Hasty, and Raphael Tieulent for filling that role for SAMPLE. The efforts of the mighty army of Caltech, Illinois, and Maryland undergraduates in keeping the data replay and tape copying going, as well as providing a refreshing perspective on life, are greatly appreciated. The various postdocs associated with this experiment have all made meaningful contributions and should be recognized: Todd Averett, Juncai Gao, Alice Hawthorne-Allen, Takeyasu Ito, and Johannes Ritter. I would also like to thank Mark Pitt for all of his work on the experiment and for the many e-mails we exchanged as I was writing this dissertation. Thank you to all the collaborators listed in Appendices C and D for their efforts in making SAMPLE such a success.

The staff of the MIT-Bates Linear Accelerator Center has done a wonderful job of providing beam of extremely high caliber and creating a positive working environment. From the vacuum technicians sacrificing their Memorial Day weekend in order to disassemble the target to the polarized source guys coming in at all hours of the day or night to put the half wave plate in, they have all done excellent work and I thank them for it.

Last, but certainly not least, I wish to thank my wife Jessica for being my

primary source of support and inspiration throughout my career at Maryland. I am in complete awe of her for everything she has already accomplished in her life. She is an incredible woman with who I am honored to share the rest of my life. Thank you Jess.

TABLE OF CONTENTS

LIST OF TABLES

LIST OF FIGURES

Chapter 1

Introduction and Theory

1.1 Introduction

In the non-relativistic quark model, the proton is understood to consist of three point particles: a pair of up quarks and a down quark. These constituent quarks are massive particles, approximately 300 MeV/c^2 in mass, and possess the proper attributes of spin and charge to describe the proton. This description of the proton is at loggerheads with the fundamental theory that describes all composite particles in the universe, quantum chromodynamics or QCD. In this theory the quarks are still point-like particles but are far less massive, of order 10 MeV/c^2. Furthermore, in this fundamental theory protons are no longer composed of only three quarks; they consist of an unknown number of quark-antiquark pairs that bubble in and out of existence as determined by the Heisenberg uncertainty principle. QCD allows other quark flavors to exist in the proton, namely the strange

flavored quarks.

A major focus of nuclear physics is to reconcile the successes of the non-relativistic quark model with the fundamental theory of QCD. Many recent experiments have probed the quark structure of the proton and the neutron attempting to elucidate how the valence and sea quarks contribute to the properties of the nucleon. This dissertation reports on one such experiment, the SAMPLE experiment at the MIT-Bates Linear Accelerator Facility in Middleton, Massachusetts [McK89a]. In SAMPLE parity violating elastic scattering of longitudinally polarized electrons from protons ($\vec{e}$-p) is used to measure the neutral weak magnetic moment of the proton μ_p^Z, the neutral weak analogue of the electromagnetic magnetic moment μ_p. Knowledge of μ_p^Z makes it possible to decompose μ_p into contributions from the three lightest quark flavors up u, down d, and strange s.

The remainder of this chapter provides motivation and theory for the experiment. It begins with a brief discussion of the structure of the proton and the role of the strange quark. This is followed by a discussion of the formalism and derivations of important theoretical results. Finally, various predictions for the strange quark contribution to the proton's magnetic moment μ_s are presented.

Chapter 2 describes the experimental apparatus used to collect data during the SAMPLE experiment. Chapter 3 discusses the procedures used to analyze the collected data. In Chapter 4, final results for the experiment are extracted and a comparison to the predictions of Chapter 1 is performed. Appendix A

contains the details of various feedback mechanisms used during the experiment to stabilize the electron beam. Appendix B contains tables of detector yield correlations with beam parameters (see Section 3.2) Appendices C and D lists the members of the SAMPLE collaboration for the 1998 and 1999 data taking periods.

1.1.1 Structure of the Proton

In the 1930s, physicists were convinced that the proton was an elementary particle, i.e. that it had no internal structure and was therefore indivisible [Wei72]. As such, the proton was expected to obey the Dirac equation for a point particle of spin $\frac{1}{2}$ [HM84]:

$$H\psi = (\boldsymbol{\alpha}\cdot\mathbf{P} + \beta M_p)\psi. \tag{1.1}$$

where $\mathbf{P}$ is the proton's momentum, M_p is the proton's mass, and $\boldsymbol{\alpha}$ and β are undetermined coefficients*. Proceeding from this assumption, theorists predicted that the proton's magnetic moment (the response of the proton to an applied magnetic field) must be exactly one nuclear magneton (n.m.), $\frac{e\hbar}{2M_pc}$. In 1933, the German scientists Frisch and Stern carried out the first measurement of the proton's magnetic moment μ_p [FS33]. They reported that μ_p was "between 2 and

*The requirement that the relativistic energy-momentum relation $H^2\psi = (\mathbf{P}^2 + M_p^2)\psi$ be satisfied means that $\boldsymbol{\alpha}$ and β have to be 4×4 matrices, which is what allows the Dirac equation to describe a spin $\frac{1}{2}$ particle and its antiparticle.

3 nuclear magnetons", forcing a reconsideration of theories about the proton.

Frisch and Stern's result for μ_p was the first experimental evidence that the proton possesses internal structure, that it is not a Dirac point particle. Forty years would pass before there would be an experiment that directly observed the proton's constituent particles. What we now know as the proton's quark structure was observed in experiments at the Stanford Linear Accelerator Center (SLAC) in the late 1960's and early 1970's [FK72]. The development of quantum chromodynamics (QCD) and the Standard Model (SM) followed soon thereafter. QCD and the SM give physicists the tools necessary to describe the physical composite particles, hadrons such as the proton and neutron, in terms of their constituent elementary particles, the quarks, and the carriers of the strong force, the gluons.

In principle, it should be possible to calculate μ_p from first principles in QCD in the same way that the electron's magnetic moment μ_e has been calculated in quantum electrodynamics (QED) [KL81]. The measured value of μ_e is 1.001159652187(4) Bohr magnetons $\mu_B = \frac{e\hbar}{2M_e c}$ [Gro00] while theory predicts a value of 1.001159652460(147) μ_B [KL81]. It is a measure of QED's success as a theory that the theoretical and experimental values for the electron's magnetic moment agree to nine decimal places. Precise calculations in QED are possible because perturbation theory can be applied at low energies, the coupling constants of the theory are weak in this regime. The same cannot be said of QCD

where the couplings do not become small until high energies are attained, well above the mass of the proton. As a result, the value of μ_p determined from theory lags far behind the experimental value in the level of precision attained.

The inability of theory to make precise predictions for μ_p means that for the moment an understanding of the proton's structure has to come from experiment. It will be shown in Section 1.2 that it is possible to experimentally determine the contributions of the different quark flavors to the magnetic moment of the proton. Such a measurement has taken on added significance in recent years due to surprising evidence that has come to light about the role of the strange quark in the proton.

1.1.2 The Role of the Strange Quark

There is substantial evidence that strange quarks play a significant role in determining the low energy properties of the proton. A compelling piece of evidence comes from the deep inelastic scattering (DIS) of polarized leptons from targets of polarized nuclei with atomic number $A \leq 3$. The observables in this type of experiment are the cross section asymmetries for longitudinally polarized leptons and target nuclei and for longitudinally polarized leptons and transversely

polarized nuclei:

$$A_{\parallel} = \frac{\sigma^{\uparrow\downarrow} - \sigma^{\uparrow\uparrow}}{\sigma^{\uparrow\downarrow} + \sigma^{\uparrow\uparrow}} \tag{1.2}$$

$$A_{\perp} = \frac{\sigma^{\downarrow\rightarrow} - \sigma^{\uparrow\rightarrow}}{\sigma^{\downarrow\rightarrow} + \sigma^{\uparrow\rightarrow}} \tag{1.3}$$

where $\sigma^{\uparrow\downarrow}$ $\left(\sigma^{\uparrow\uparrow}\right)$ is the cross section when the lepton and nuclear spins are anti-aligned (aligned) and $\sigma^{\downarrow\rightarrow}$ $\left(\sigma^{\uparrow\rightarrow}\right)$ is the cross section for longitudinally polarized leptons and transversely polarized nuclei. Such experiments have been carried out using polarized electrons at the Stanford Linear Accelerator Center (SLAC) in California and by the European (EMC) and Spin Muon Collaborations (SMC) using polarized muons at CERN in Switzerland (for more information see Ref. [FJ01] and the references listed therein).

These asymmetries are used to extract the g_1 polarized structure function of the proton g_1^p and the neutron g_1^n*. The g_1 structure function is analogous in polarized DIS to the F_1 structure function in unpolarized DIS and the form factors discussed in Section 1.2.1 for elastic scattering; their purpose is to parameterize the unknown substructure of nucleons. The g_1 structure functions can be related to the individual quark spin distributions in the nucleon $\Delta q_i(x) = q_i^{\uparrow}(x) - q_i^{\downarrow}(x)$ where $q_i^{\uparrow(\downarrow)}$ is the number of quarks of flavor i (u, $\bar{u}$, d, $\bar{d}$, etc.) polarized along the direction of the nucleon's polarization. The variable $x \equiv \frac{Q^2}{2M_N\nu}$ is the fraction of

*The g_1^p structure function is derived from experiments using proton targets (A=1) while the g_1^n function comes from experiments using deuteron and ^{3}He targets (A=2 and 3) [FJ01]. The extraction of g_1^n involves the subtraction of g_1^p from g_1 of the deuteron or ^{3}He [FJ01].

the nucleon's momentum carried by the struck quark; Q^2 is the four-momentum transferred to the target by the scattering process and ν is the energy carried by the virtual boson exchanged by the lepton and nucleon.

The Ellis-Jaffe sum rule connects $g_1^{p(n)}$ to individual quark spin distributions [EJ74a, EJ74b]:

$$\Gamma_1^p \equiv \int_0^1 g_1^p(x)\mathrm{d}x = \frac{3}{36}a_3 + \frac{1}{36}a_8 + \frac{4}{36}a_0 \tag{1.4}$$

$$\Gamma_1^n \equiv \int_0^1 g_1^n(x)\mathrm{d}x = -\frac{3}{36}a_3 + \frac{1}{36}a_8 + \frac{4}{36}a_0 \tag{1.5}$$

where

$$a_0 = (\Delta u + \Delta\bar{u}) + (\Delta d + \Delta\bar{d}) + (\Delta s + \Delta\bar{s}) \tag{1.6}$$

$$a_3 = (\Delta u + \Delta\bar{u}) - (\Delta d + \Delta\bar{d}) \tag{1.7}$$

$$a_8 = (\Delta u + \Delta\bar{u}) + (\Delta d + \Delta\bar{d}) - 2(\Delta s + \Delta\bar{s}) \tag{1.8}$$

assuming SU(3) flavor symmetry. Ellis and Jaffe also assumed that there is no contribution from strange or sea quarks ($\Delta s = \Delta\bar{q}_i = 0$) so that $a_0 = a_8$; values for a_3 and a_8 could then be extracted from nucleon and hyperon beta decay. By measuring $g_1^{p(n)}$ over a range of x the SLAC and CERN experiments could determine $\Gamma_1^{p(n)}$ to compare with theory and verify the validity of the Ellis-Jaffe sum rule*. It was found that the sum rule was violated quite strongly and one

*The g_1 structure functions have a dependence on Q^2 that is not shown here. One of the sources of error in these types of experiments is the evolution of g_1 measured at various values of Q^2 to a common Q^2 point.

reason suggested for the violation was that the constraint $\Delta s = \Delta \bar{q}_i = 0$ was too stringent. It is possible to extract values for the individual quark helicity distributions by relaxing that constraint and assuming the validity of the Ellis-Jaffe sum rule [FJ01]:

$$\Delta u + \Delta \bar{u} = 0.78 \pm 0.03 \tag{1.9}$$

$$\Delta d + \Delta \bar{d} = -0.48 \pm 0.03 \tag{1.10}$$

$$\Delta s + \Delta \bar{s} = -0.14 \pm 0.03. \tag{1.11}$$

This is a surprising result for two reasons. It suggests that the total contribution of the quark spins to the total spin of the nucleon $\Delta\Sigma = \sum_i \Delta q_i$ is approximately 16% (0.16 ± 0.08). Also, contributions from the strange quarks are significantly different from zero. Both of these results contradict the prediction of the non-relativistic quark model discussed earlier.

It should be noted that in recent years the assumptions that go into the Ellis-Jaffe sum rule and the above calculation have come into question; modern analyses do not attempt to extract individual quark spin distributions using this sum rule. The next generation of experiments by the SMC as well as new experiments by the HERMES collaboration at DESY in Germany use semi-inclusive polarized lepton DIS where an outgoing hadron is detected in coincidence with the scattered lepton in order to directly measure Δq_i [FJ01]. Early results from these collaborations are not sensitive to $\Delta s + \Delta \bar{s}$ because of the lack of particle identification in their experiments, however by making assumptions about the

structure of the quark-antiquark sea the HERMES collaboration was able to extract a result of $\Delta s + \Delta \bar{s} = -0.01 \pm 0.03 \pm 0.04$ from their initial measurements [Ack99]. A similar result can be extracted from a recent SMC measurement by assuming an SU(3) symmetric sea of quarks:

$$\Delta \bar{q} = \Delta \bar{u} = \Delta \bar{d} = \Delta s = \Delta \bar{s}. \tag{1.12}$$

The collaboration determined that $\Delta \bar{q} = 0.01 \pm 0.04 \pm 0.03$ leading to $\Delta s + \Delta \bar{s} = 0.02 \pm 0.06 \pm 0.04$ [Ade98]. The weighted average of these three determinations of $\Delta s + \Delta \bar{s}$ is -0.086 ± 0.024.

Another piece of evidence for substantial strange quark contributions to static proton properties is the measurement of the so-called π-N sigma term, $\Sigma_{\pi N}$. The π-N sigma term is proportional to the isospin even amplitude for scattering of pions from nucleons, $\bar{D}^+(t)$ [GLS91]:

$$\Sigma_{\pi N} = F_\pi^2 \bar{D}^+(t = 2m_\pi^2) \tag{1.13}$$

where F_π is the pion decay constant and m_π is the mass of the pion. The variable t is a Mandelstam variable equal to $(p_A + p_C)^2$ where $p_A(p_C)$ is the incoming (outgoing) momentum of a scattered particle. The point $t = 2m_\pi^2$ is known as the Cheng-Dashen point [CD71]. It is unphysical, but the experimental data can be extrapolated to it using phase-shift analysis. A low-energy theorem of current

algebra relates $\Sigma_{\pi N}$ to the σ-term matrix element [GLS91]:

$$\sigma = \frac{1}{2m}\langle p|\hat{m}(\bar{u}u + \bar{d}d)|p\rangle \tag{1.14}$$

$$\hat{m} = \frac{1}{2}(m_u + m_d) \tag{1.15}$$

where m is the mass of the proton. The theorem states that $\frac{\Sigma_{\pi N}}{\sigma} \to 1$ in the chiral limit, i.e. as $m_u, m_d \to 0$. There are corrections to the theorem due to finite quark masses and the evolution of σ and $\Sigma_{\pi N}$ from $t = 0$ to the Cheng-Dashen point. After these corrections have been taken into account $\sigma(t = 2m_\pi^2) = 45 \pm 7$ MeV [GLS91].

Approximate SU(3) symmetry can be used to extract a theoretical value for σ in terms of a strange quark matrix element of the proton [GLS91]:

$$\sigma = \frac{\sigma_0}{1 - y} \tag{1.16}$$

$$\sigma_0 = \frac{1}{2m}\langle p|\bar{u}u + \bar{d}d - 2\bar{s}s|p\rangle \tag{1.17}$$

$$y = 2\frac{\langle p|\bar{s}s|p\rangle}{\langle p|\bar{u}u + \bar{d}d|p\rangle}. \tag{1.18}$$

The coefficient $\sigma_0 = 35 \pm 5$ MeV leading to a value of $y \simeq 0.2$. This result indicates that the scalar strange quark matrix element of the proton, $\langle p|\bar{s}s|p\rangle$ is non-zero. (The result for g_1^p discussed previously can be written in terms of a non-zero strange quark matrix element, the axial vector element $\langle p|\bar{s}\gamma^5\gamma^\mu s|p\rangle$.) The implication is that the strange quarks constitute a significant portion of the mass of the proton, approximately 130 out of 938 (MeV/c^2) [GLS91].

The discovery that a pair of strange quark matrix elements, $\langle p|\bar{s}s|p\rangle$ and

$\langle p|\bar{s}\gamma^5\gamma^\mu s|p\rangle$, are non-zero provided motivation to question whether there might be other non-zero elements. Kaplan and Manohar suggested that it would be possible to determine the proton's vector strange matrix element $\langle p|\bar{s}\gamma^\mu s|p\rangle$ by measuring the neutral weak magnetic moment of the proton $G^p_{M,Z}$ [KM88]. Shortly thereafter McKeown and Beck provided a means for measuring $G^p_{M,Z}$ by the elastic scattering of polarized electrons from protons [McK89b, Bec89]. The following section will discuss this technique for extracting $\langle p|\bar{s}\gamma^\mu s|p\rangle$.

1.2 Theory and Formalism

The vector strange matrix element is determined via a measurement of the neutral weak form factor of the proton, $G^p_{M,Z}$. Section 1.2.1 will discuss the various form factors of interest in this experiment and their relation to static properties of the nucleon* such as the charge and magnetic moment. Section 1.2.2 will show how the form factors can be rewritten in terms of contributions from individual quark flavors. Section 1.2.3 will describe the experimental observables that are measured in order to extract $G^s_M \propto \langle p|\bar{s}\gamma^\mu s|p\rangle$. Section 1.2.4 will discuss the various electroweak radiative corrections that have to be made to the tree level expressions found in the other sections.

*Throughout this work, the term nucleon (N) will be used to refer to protons (p) and neutrons (n) interchangeably. Thus, any constants labeled by a superscript N are actually a pair of constants: one for the proton and one for the neutron.

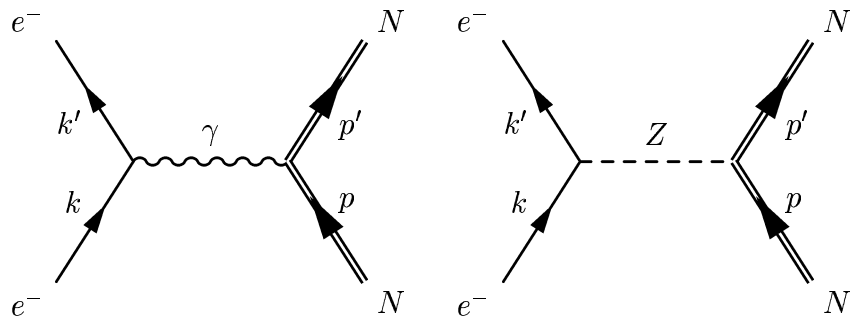

(a) $\gamma-$exchange (b) $Z-$exchange

Figure 1.1: First order diagrams for the elastic scattering of an electron from a nucleon. The incoming (outgoing) four-momentum of the electron is denoted k (k'). The same quantities for the nucleon are denoted p (p'). The four-momentum of the exchanged boson is defined as $q \equiv p' - p = k - k'$ and $Q^2 \equiv -q^2 > 0$.

1.2.1 Form Factors and Static Properties

To first order, or tree level, the interaction between an electron and a nucleon is described by the two Feynman diagrams of Figure 1.1: single photon (γ) exchange for the electromagnetic interaction and single vector boson (Z) exchange for the neutral weak interaction. Each diagram has an associated invariant amplitude, $\mathfrak{M}_\gamma$ or $\mathfrak{M}_Z$ respectively, which are summed to form the total invariant amplitude for the reaction $\mathfrak{M}$. Following the notation of Ref. [Mus94], the couplings of fundamental fermions to the γ and the Z are written in the following way:

$$iee_f\gamma^\mu \tag{1.19}$$

$$i\frac{gM_Z}{4M_W}\gamma^\mu(g_V^f + g_A^f\gamma_5) \tag{1.20}$$

where e (g) is the EM (weak) coupling strength, $M_{Z(W)}$ is the mass of the Z (W) boson, e_f is the fermion's EM charge, and $g^f_{V(A)}$ is the fermion's vector (axial

Fermion	e_f	g_V^f	g_A^f
ν_e, ν_μ, ν_τ	0	1	-1
e^-, μ^-, τ^-	-1	$-1+4\sin^2\theta_W$	1
u, c, t	$\frac{2}{3}$	$1-\frac{8}{3}\sin^2\theta_W$	-1
d, s, b	$-\frac{1}{3}$	$-1+\frac{4}{3}\sin^2\theta_W$	1

Table 1.1: The electromagnetic and weak charges of the fundamental fermions [Mus94].

vector) weak charge. The various fermion charges can be found in Table 1.1.

Armed with the EM and weak couplings of equations 1.19 and 1.20 it is a simple matter to write the invariant amplitudes in terms of leptonic currents l of the electron and hadronic currents J of the nucleon:

$$\mathfrak{M}_\gamma = \frac{4\pi\alpha}{q^2} e_l l^\mu J_{\gamma\mu} \tag{1.21}$$

$$\mathfrak{M}_Z = -\frac{G_F}{2\sqrt{2}}(g_V^l l^\mu + g_A^l l^{\mu 5})(J_{Z\mu} + J_{Z\mu 5}) \tag{1.22}$$

where $q \equiv p' - p = k - k'$, $k(k')$ is the four-momentum of the incident (scattered) electron, and $p(p')$ is the four-momentum of the target (recoil) nucleon*. The weak coupling constant and W boson mass of equation 1.20 have been combined into one constant, the Fermi coupling constant [Mus94]

$$G_F = \frac{g^2}{4\sqrt{2}M_W^2} \tag{1.23}$$

and the fine structure constant $\alpha = \frac{e^2}{4\pi\hbar c}$ has been substituted for e^2†. There is no

*This is a point of departure from the formalism of Ref. [Mus94] where $Q \equiv k - k'$. In this work $Q^2 \equiv -q^2 > 0$.

†Unless otherwise noted the equations in this work have been derived in a set of units where $\hbar c = 1$.

q^2 in the denominator of $\mathfrak{M}_Z$ due to the Z propagator because the invariant amplitudes are derived in a kinematic regime where $q^2 \ll M_Z$. The lepton currents l^μ and $l^{\mu 5}$ have a particularly simple form since they involve only fundamental particles:

$$l^\mu \equiv \bar{u}_l \gamma^\mu u_l \tag{1.24}$$

$$l^{\mu 5} \equiv \bar{u}_l \gamma^\mu \gamma_5 u_l \tag{1.25}$$

where u_l is the lepton spinor. This spinor depends on the four-momentum of the lepton, k or k', and on the spin state, s or s'.

Unfortunately the hadronic currents do not have forms as simple as the leptonic currents because the nucleon is a composite particle. Under the assumptions of Lorentz and gauge invariance, the hadronic vector currents of the EM and weak interactions can be cast in a general form [HM84]:

$$J_V^\mu = \bar{\mathcal{U}}_N \left[F_1^{VN}(q^2)\gamma^\mu + F_2^{VN}(q^2)\frac{i\sigma^{\mu\nu}q_\nu}{2M} \right] \mathcal{U}_N \tag{1.26}$$

where $\mathcal{U}_N$ is a nucleon spinor, V denotes the interaction type (either electromagnetic γ or neutral weak Z), and N is the hadron (p or n). The factors F_1^{VN} and F_2^{VN} are known as the Dirac and Pauli form factors, respectively. In the context of elastic $\vec{e}$-p scattering there are two sets of these form factors: $F_{1/2}^{\gamma N}$ from the EM interaction and $F_{1/2}^{ZN}$ from the weak interaction.

It is useful to exchange the Dirac and Pauli form factors defined above for

another set of form factors [HM84]:

$$G_M^{VN}(Q^2) = F_1^{VN}(Q^2) + F_2^{VN}(Q^2) \tag{1.27}$$

$$G_E^{VN}(Q^2) = F_1^{VN}(Q^2) - \tau F_2^{VN}(Q^2) \tag{1.28}$$

$$\tau = \frac{-q^2}{4M_N} = \frac{Q^2}{4M_N}. \tag{1.29}$$

These are known as the Sachs form factors and their physical meaning is easier to discern. In the limit as $Q^2 \to 0$ the magnetic and electric form factors reduce to the magnetic moment and electric charge respectively: $G_M^{\gamma N} \to \mu_N$ and $G_E^{\gamma N} \to e_N$. The same is true of the neutral weak electric and magnetic form factors except that they reduce to the neutral weak magnetic moment μ_N^Z and neutral weak charge e_N^Z. When boosted to the Breit frame ($\mathbf{p}' = -\mathbf{p}$) the Sachs form factors are the Fourier transforms of the nucleon charge and magnetic moment distributions [HM84].

There is an additional hadronic current for Z exchange due to the axial vector component of the weak interaction. This current gives rise to another form factor G_A^{eN}:

$$J_Z^{\mu 5} = \bar{\mathcal{U}}_N G_A^{eN} \gamma^\mu \gamma_5 \mathcal{U}_N. \tag{1.30}$$

The factor G_A^{eN} is known as the nucleon's neutral weak axial form factor. The total hadronic neutral weak current is the sum of the neutral weak vector current (equation 1.26) and the axial current (equation 1.30:

$$J_Z^\mu = \bar{\mathcal{U}}_N \left[F_1^{ZN} \gamma^\mu + F_2^{ZN} \frac{i\sigma^{\mu\nu} q_\nu}{2M} + G_A^{eN} \gamma^\mu \gamma_5 \right] \mathcal{U}_N. \tag{1.31}$$

As mentioned previously the various Sachs form factors, EM and neutral weak, as well as the axial vector form factor have a dependence on the momentum transferred by the exchanged boson Q^2.

1.2.2 Quark Decomposition of the Form Factors

Thus far the hadronic currents have been written without any thought to their underlying structure, the form factors have been used to parameterize that structure. However, the nucleon is composed of quarks and it is possible to write a current for each quark flavor. The quark currents are written as follows:

$$\hat{J}^{\mu}_{\gamma} = \sum_{q} e_q \bar{u}_q \gamma^{\mu} u_q \tag{1.32}$$

$$\hat{J}^{\mu}_{Z} = \sum_{q} g^q_V \bar{u}_q \gamma^{\mu} u_q \tag{1.33}$$

$$\hat{J}^{\mu 5}_{Z} = \sum_{q} g^q_A \bar{u}_q \gamma^{\mu} \gamma_5 u_q \tag{1.34}$$

where u_q is a quark spinor of flavor q. The EM and weak charges e_q and $g^q_{V/A}$ are given in Table 1.1. Nominally, the sum runs over all six quark flavors, but it is sufficient to include only the three lightest quarks u, d, and s [KM88]. The masses of the three heaviest quarks c, b, and t are greater than the mass of the proton resulting in a strong suppression of their contributions to nucleonic properties.

The nucleon currents of the previous section can be expressed in terms of the

quark currents from equations 1.32 to 1.34 [Mus94]:

$$\begin{aligned} J^{\mu}_{\gamma} &= \left\langle N \left| \hat{J}^{\mu}_{\gamma} \right| N \right\rangle \\ &= \left\langle N \left| \sum_{q} e_q \bar{u}_q \gamma^{\mu} u_q \right| N \right\rangle \end{aligned} \tag{1.35}$$

$$J^{\mu}_{\gamma} = \sum_{q} e_q \bar{\mathcal{U}}_N \left[F_1^{qN} \gamma^{\mu} + F_2^{qN} \frac{i\sigma^{\mu\nu} q_{\nu}}{2M} \right] \mathcal{U}_N$$

$$J^{\mu}_{Z} = \sum_{q} g_V^q \bar{\mathcal{U}}_N \left[F_1^{qN} \gamma^{\mu} + F_2^{qN} \frac{i\sigma^{\mu\nu} q_{\nu}}{2M} \right] \mathcal{U}_N \tag{1.36}$$

$$J^{\mu 5}_{Z} = \sum_{q} g_A^q \bar{\mathcal{U}}_N G_A^{qN} \gamma^{\mu} \gamma_5 \mathcal{U}_N. \tag{1.37}$$

In these equations, q represents a quark flavor and q_{ν} represents one component of the four-momentum transferred by the exchanged boson. It is important to note that the quark form factors F_1^{qN} and F_2^{qN} are the same in equations 1.35 and 1.36, there is no dependence on the type of interaction (EM or neutral weak) like there was in the hadronic case. The nucleon form factors $F_1^{\gamma/Z}$ and $F_2^{\gamma/Z}$* can be written in terms of the quark form factors by equating the EM current equations and neutral weak current equations:

$$F^{\gamma}_{1/2} = \sum_{q} e_q F^q_{1/2} \tag{1.38}$$

$$F^{Z}_{1/2} = \sum_{q} g_V^q F^q_{1/2} \tag{1.39}$$

$$G^{e}_{A} = \sum_{q} g_A^q G^q_A. \tag{1.40}$$

*The superscript N denoting the type of nucleon involved in the interaction will be dropped except where it is necessary to avoid confusion.

Clearly $F_{1/2}^{\gamma}$ and $F_{1/2}^{Z}$ can be expressed as Sachs form factors as defined in equations 1.28 and 1.27. The EM and neutral weak form factors are then written as follows:

$$G_{E/M}^{\gamma} = \sum_{q} e_q G_{E/M}^{q} \tag{1.41}$$

$$G_{E/M}^{Z} = \sum_{q} g_V^q G_{E/M}^{q}. \tag{1.42}$$

The result is a set of five nucleon form factors written in terms of six unknown quark form factors for each nucleon.

The number of unknown quantities in these equations can be greatly reduced by assuming isospin symmetry. Under this assumption the distribution of u and $\bar{u}$ quarks in the proton is the same as the distribution of d and $\bar{d}$ quarks in the neutron, and vice versa*. In terms of quark form factors isospin symmetry means the following:

$$G_{E/M}^{u,p} = G_{E/M}^{d,n} \equiv G_{E/M}^{u}, \quad G_{E/M}^{d,p} = G_{E/M}^{u,n} \equiv G_{E/M}^{d}, \quad G_{E/M}^{s,N} \equiv G_{E/M}^{s}, \tag{1.43}$$

$$G_{A}^{u,p} = G_{A}^{d,n} \equiv G_{A}^{u}, \qquad G_{A}^{d,p} = G_{A}^{u,n} \equiv G_{A}^{d}, \qquad G_{A}^{s,N} \equiv G_{A}^{s}. \tag{1.44}$$

Recall that it is sufficient to consider only the lightest three quarks.

The well-known electromagnetic form factors of the proton and neutron can be written in terms of just three quark form factors in light of these relations and

*The distributions of u, d, $\bar{u}$, and $\bar{d}$ quarks in a given nucleon are not required to be the same.

equation 1.41:

$$G_{E/M}^{\gamma p} = \frac{2}{3}G_{E/M}^{u} - \frac{1}{3}G_{E/M}^{d} - \frac{1}{3}G_{E/M}^{s} \tag{1.45}$$

$$G_{E/M}^{\gamma n} = -\frac{1}{3}G_{E/M}^{u} + \frac{2}{3}G_{E/M}^{d} - \frac{1}{3}G_{E/M}^{s}. \tag{1.46}$$

This forms a set of two equations with three unknowns for the electric and magnetic factors separately. An additional equation with the same set of unknowns can be written using the neutral weak form factor of the proton:

$$\begin{aligned} G_{E/M}^{Zp} &= \left(1 - \frac{8}{3}\sin^2\theta_W\right) G_{E/M}^{u} + \left(-1 + \frac{4}{3}\sin^2\theta_W\right) G_{E/M}^{d} \\ &\quad + \left(-1 + \frac{4}{3}\sin^2\theta_W\right) G_{E/M}^{s} \\ &= \left(1 - 4\sin^2\theta_W\right) G_{E/M}^{\gamma p} - G_{E/M}^{\gamma n} - G_{E/M}^{s}. \end{aligned} \tag{1.47}$$

It is clear that a measurement of $G_{E/M}^{Zp}$ would make it possible to decompose the electric or magnetic form factors of the proton and neutron into contributions from the individual quark flavors:

$$G_{E/M}^{u} = (3 - 4\sin^2\theta_W)G_{E/M}^{\gamma p} - G_{E/M}^{Zp} \tag{1.48}$$

$$G_{E/M}^{d} = (2 - 4\sin^2\theta_W)G_{E/M}^{\gamma p} + G_{E/M}^{\gamma n} - G_{E/M}^{Zp} \tag{1.49}$$

$$G_{E/M}^{s} = (1 - 4\sin^2\theta_W)G_{E/M}^{\gamma p} - G_{E/M}^{\gamma n} - G_{E/M}^{Zp}. \tag{1.50}$$

Under the assumption of isospin symmetry the axial form factors of the proton and neutron are written as

$$G_A^{ep} = -(G_A^{u} - G_A^{d}) + G_A^{s} \tag{1.51}$$

$$G_A^{en} = (G_A^{u} - G_A^{d}) + G_A^{s}. \tag{1.52}$$

By rewriting the combination $G_A^u - G_A^d$ as a third isovector form factor $G_A = (G_A^u - G_A^d)$ the two equations above can be simplified into one:

$$G_A^e = -G_A\tau_3 + G_A^s \tag{1.53}$$

where $\tau_3 = +1(-1)$ for a proton (neutron). The form factor G_A can be related to the coupling constants g_A and g_V measured in neutron beta decay: $G_A(Q^2 = 0) \equiv -\frac{g_A}{g_V} = 1.2670 \pm 0.0035$ [Gro00]. The strange axial form factor G_A^s comes from the axial vector strange matrix element $\langle p|\bar{s}\gamma_\mu\gamma_5 s|p\rangle$ measured in the deep inelastic scattering experiments discussed in Section 1.1.2: $G_A^s(Q^2 = 0) = \Delta s + \Delta\bar{s} = -0.086 \pm 0.024$ [FJ01, Ack99, Ade98].

The EM and axial form factors depend on momentum transfer. In this work the Galster dipole form is assumed, which is [Gal71]:

$$G_E^{\gamma p}(Q^2) = G_D^V(Q^2), \qquad G_E^{\gamma n}(Q^2) = -\frac{\mu_n\tau G_D^V(Q^2)}{1 + \lambda_n\tau}, \tag{1.54}$$

$$G_M^{\gamma p}(Q^2) = \mu_p G_D^V(Q^2), \qquad G_M^{\gamma n}(Q^2) = \mu_n G_D^V(Q^2), \tag{1.55}$$

$$G_A^e(Q^2) = G_A^e(0) G_D^A(Q^2) \tag{1.56}$$

where $G_D^{V/A} \equiv \left(1 + \frac{Q^2}{M_{V/A}}\right)^{-2}$ and $\lambda_n = 5.6$. The vector dipole mass $M_V = 0.843$ (GeV/c^2) [Höh76] and the axial dipole mass $M_A = 1.069 \pm 0.016$ (GeV/c^2) [Lie99]. Due to the unknown Q^2 dependence of G_A^s the $Q^2 = 0$ value is used with a 100% error bar. A 2% error bar is assigned to the determination of $G_E^{\gamma p}$, $G_M^{\gamma p}$, and $G_M^{\gamma n}$ and a 50% error bar is assigned to $G_E^{\gamma n}$. The Q^2 dependence of the form factors will not be shown throughout this work.

1.2.3 Observables

The results of the previous section make it clear that a measurement of the proton's neutral weak form factor would be very useful. As equations 1.21 and 1.22 indicate such a measurement could be done by scattering electrons from a proton because the cross section is proportional to the square of the tree-level diagrams in Figure 1.1, $\sigma \propto |\mathfrak{M}_\gamma + \mathfrak{M}_Z|^2$. However, the neutral weak current that yields G_M^{Zp} is strongly suppressed relative to the electromagnetic current in an absolute cross section measurement. In order to access G_M^{Zp} it is necessary to use the parity violating nature of the weak interaction.

The parity operation causes a total spatial inversion of an operator or wave function, all three space axes invert through the origin: $x \to -x$, $y \to -y$, and $z \to -z$. Parity violation can be probed using longitudinally polarized electrons because the two states of electron polarization correspond to the two states of parity. Parity violation is built into the neutral weak current via the vector - axial vector form of the interaction (the axial vector portion leads to parity violation). The neutral weak invariant amplitude of equation 1.22 can be rewritten as the sum of two amplitudes, a parity conserving (PC) amplitude $\mathfrak{M}_{PC}$ and a parity violating (PV) amplitude $\mathfrak{M}_{PV}$:

$$\mathfrak{M}_Z = \mathfrak{M}_{PC} + \mathfrak{M}_{PV} \tag{1.57}$$

where

$$\mathfrak{M}_{PC} = -\frac{G_F}{2\sqrt{2}}\left(g_V^l l^\mu J_{Z\mu} + g_A^l l^{\mu 5} J_{Z\mu 5}\right) \tag{1.58}$$

$$\mathfrak{M}_{PV} = -\frac{G_F}{2\sqrt{2}}\left(g_V^l l^\mu J_{Z\mu 5} + g_A^l l^{\mu 5} J_{Z\mu}\right). \tag{1.59}$$

Operators formed from a vector and an axial vector operator are parity violating while operators formed from squares of either one are parity conserving.

The parity violating cross section asymmetry for the scattering of longitudinally polarized electrons from unpolarized protons is defined as the difference in the cross section for positive and negative helicity states divided by the sum:

$$A_N \equiv \frac{\sigma_+ - \sigma_-}{\sigma_+ + \sigma_-} \tag{1.60}$$

$$= \frac{|\mathfrak{M}_\gamma + \mathfrak{M}_Z|_+^2 - |\mathfrak{M}_\gamma + \mathfrak{M}_Z|_-^2}{|\mathfrak{M}_\gamma + \mathfrak{M}_Z|_+^2 + |\mathfrak{M}_\gamma + \mathfrak{M}_Z|_-^2} \tag{1.61}$$

$$= \frac{|\mathfrak{M}_\gamma + \mathfrak{M}_{PC} + \mathfrak{M}_{PV}|_+^2 - |\mathfrak{M}_\gamma + \mathfrak{M}_{PC} + \mathfrak{M}_{PV}|_-^2}{|\mathfrak{M}_\gamma + \mathfrak{M}_{PC} + \mathfrak{M}_{PV}|_+^2 + |\mathfrak{M}_\gamma + \mathfrak{M}_{PC} + \mathfrak{M}_{PV}|_-^2} \tag{1.62}$$

$$\approx 2\frac{\mathfrak{M}_\gamma^* \mathfrak{M}_{PV}}{|\mathfrak{M}_\gamma|^2} \tag{1.63}$$

$$A_N = \left(-\frac{G_F Q^2}{4\sqrt{2}\pi\alpha}\right)\left(g_V^l l^\mu J_{Z\mu 5} + g_A^l l^{\mu 5} J_{Z\mu}\right). \tag{1.64}$$

When expanding equation 1.62, terms of order G_F^2 in the numerator and of order G_F in denominator are discarded. Parity conserving terms, those that are not linear in $\mathfrak{M}_{PV}$, cancel out of the numerator but add together in the denominator. The parity violating terms have the opposite behavior which is how equation 1.63 follows from equation 1.62. This asymmetry is clearly sensitive at leading order to the neutral weak interaction through $\mathfrak{M}_{PV}$, which is desirable for extracting

neutral weak form factors.

After a bit of manipulation equation 1.64 reduces to

$$A_N = \left(\frac{-G_F Q^2}{4\sqrt{2}\pi\alpha}\right) \frac{\epsilon G_E^\gamma G_E^Z + \tau G_M^\gamma G_M^Z - (1 - 4\sin^2\theta_W)\epsilon' G_M^\gamma G_A^e}{\epsilon \left(G_E^\gamma\right)^2 + \tau \left(G_M^\gamma\right)^2} \tag{1.65}$$

where τ is defined by equation 1.29 and

$$\epsilon = \frac{1}{1 + 2(1+\tau)\tan^2\frac{\theta}{2}} \tag{1.66}$$

$$\epsilon' = \sqrt{\tau(1+\tau)(1-\epsilon^2)}. \tag{1.67}$$

The quantities τ, ϵ, and ϵ' are purely kinematic in origin. By appropriate choice of kinematics in a given $\vec{e}$-p scattering experiment it is possible to enhance or reduce sensitivity to a given set of neutral weak form factors. In an experiment at backward scattering angles the first term of equation 1.65 goes to zero, leaving sensitivity only to G_M^Z and G_A^e. This is the kinematic regime in which the SAMPLE experiment is performed.

At this point it would appear that a measurement of A_p would fully constrain G_M^{Zp} because G_A^e has been measured in other experiments (equation 1.53). However, the expressions for the form factors have been derived to first order, only the single boson exchange diagrams have been considered (Figure 1.1). There are higher order electroweak radiative corrections to these diagrams that must be taken into account. These corrections will be discussed in Section 1.2.4, but

for reference the full expressions for the form factors are listed below:

$$G_{E/M}^{Zp} = (1 - 4\sin^2\theta_W)(1 + R_V^p)G_{E/M}^{\gamma p} - (1 + R_V^n)G_{E/M}^{\gamma n} - (1 + R_V^{(0)})G_{E/M}^{s} \tag{1.68}$$

$$G_{E/M}^{Zn} = -(1 + R_V^p)G_{E/M}^{\gamma p} + (1 - 4\sin^2\theta_W)(1 + R_V^n)G_{E/M}^{\gamma n} - (1 + R_V^{(0)})G_{E/M}^{s} \tag{1.69}$$

$$G_A^e = -(1 + R_A^1)G_A\tau_3 + R_A^0 + (1 + R_A^{(0)})G_A^s \tag{1.70}$$

where R_V^N, $R_V^{(0)}$, R_A^1, R_A^0, and $R_A^{(0)}$ are the electroweak radiative corrections. The vector radiative corrections can be calculated reliably and are small in size, but this is not true of the axial vector corrections. As a result, it is desirable to constrain G_A^e experimentally.

Another equation with the same pair of unknowns is necessary, and the parity violating neutron asymmetry A_n would seem like a logical choice, but the lack of a high density target of free neutrons makes A_n very difficult to measure. However, high density targets of deuterons are possible and measuring the asymmetry in quasielastic scattering of polarized electrons from deuterons A_d would yield another equation with the necessary unknowns. In the static approximation the neutron and proton in the deuteron are treated as free, non-interacting particles [HPD92]. The proton and neutron asymmetries add incoherently, resulting in the following expression for A_d:

$$A_d = \frac{\sigma_p A_p + \sigma_n A_n}{\sigma_d} \tag{1.71}$$

where σ_N is the cross section for elastic e-N scattering and $\sigma_d = \sigma_p + \sigma_n$. At the same kinematics as the A_p measurement A_d is sensitive to the same two form factors G_M^s and G_A^e, but with different weightings. (Actually, the combination of A_p and A_d is sensitive to G_M^s and the isovector portion of the axial form factor $G_A^e(T=1)$.)

The fact that the deuteron is a nucleus means that nuclear structure effects ignored in the static approximation could have an impact on A_d. Hadjimichael, Poulis, and Donnelly assessed the effects of nuclear structure on A_d at the SAMPLE kinematics in 1992 [HPD92]. They determined that the asymmetry is sensitive to the presence of final state interactions, but that there is very little dependence on the model of the nucleon-nucleon (NN) interactions used to perform the calculations at the quasielastic peak. The difference between the static approximation and realistic models of nuclear structure appear to be about 2-3%. A more recent paper by Diaconescu, Schiavilla, and van Kolck used a more realistic model for the NN interaction (Argonne v_{18}) and performed a calculation in chiral perturbation theory [DSvK01]. They found that nuclear structure effects on the asymmetry are about 0.2% at the quasielastic peak and grow to about 3% away from the peak. This large change away from the peak is offset by the smallness of the cross section relative to the quasielastic peak. The expectation is that the inclusion of nuclear structure effects in the calculation of the asymmetry would affect the extraction of G_M^s and $G_A^e(T=1)$ at the 1% level.

1.2.4 Electroweak Radiative Corrections

As discussed in the previous section, the neutral weak and axial form factors contain correction factors due to higher order electroweak processes. There are three effects that contribute to a given electroweak radiative correction [Mus94]: one quark processes, many quark processes, and heavy quark renormalization of light quark operators. The total radiative correction is the sum of the contributions from each process, as indicated here*

$$R_V^{T=0} = R_V^{T=0}(1q) + R_V^{T=0}(\text{many } q) - \Delta_V \tag{1.72}$$

$$R_V^{T=1} = R_V^{T=1}(1q) + R_V^{T=1}(\text{many } q) \tag{1.73}$$

$$R_V^{(0)} = R_V^{(0)}(1q) + R_V^{(0)}(\text{many } q) - \Delta_V \tag{1.74}$$

$$R_A^{T=0} = R_A^{T=0}(1q) + R_A^{T=0}(\text{many } q) + 2\Delta_A \tag{1.75}$$

$$R_A^{T=1} = R_A^{T=1}(1q) + R_A^{T=1}(\text{many } q) \tag{1.76}$$

$$R_A^{(0)} = R_A^{(0)}(1q) + R_A^{(0)}(\text{many } q) + \frac{4}{3}\Delta_A. \tag{1.77}$$

The factors Δ_V and Δ_A come from the heavy quark renormalization of light quark operators, they account for the fact that contributions from the c, b, and

*The vector proton and neutron corrections are extracted from the isovector and isoscalar corrections via the following equations [Mus94]:

$$R_V^p = \frac{(1 - 2\sin^2\theta_W)R_V^{T=1} - 2\sin^2\theta_W R_V^{T=0}}{1 - 4\sin^2\theta_W}$$

$$R_V^n = (1 - 2\sin^2\theta_W)R_V^{T=1} + 2\sin^2\theta_W R_V^{T=0}.$$

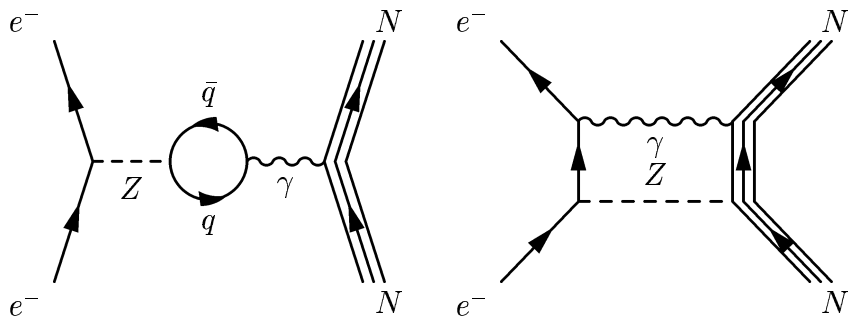

(a) Vacuum Polarization (b) Box

Figure 1.2: Some representative one-quark diagrams that contribute to electroweak radiative corrections.

t quark flavors have been ignored throughout the form factor derivations of the previous section. The contributions from these factors can be safely ignored in practice because $\Delta_V \lesssim 10^{-4}$ and $\Delta_A \lesssim 10^{-2}$ [KM88]. These are very minor contributions compared to the remaining two (see Table 1.2).

The second class of contributions to the electroweak radiative corrections are the one quark diagrams, like those depicted in Figure 1.2. The defining element of these diagrams is that they involve interactions with only one of the quarks in the target hadron. The diagrams of Figure 1.2 are only a sampling of the many possibilities in this class of correction. These are purely electroweak corrections that are calculable in the standard model; uncertainties due to hadronic structure are confined to the final class of contributions, the many quark corrections.

The many quark correction diagrams involve interactions between multiple quarks in the hadron, particularly the exchange of Z bosons between quarks. This set of corrections is particularly difficult to address because the strong cou-

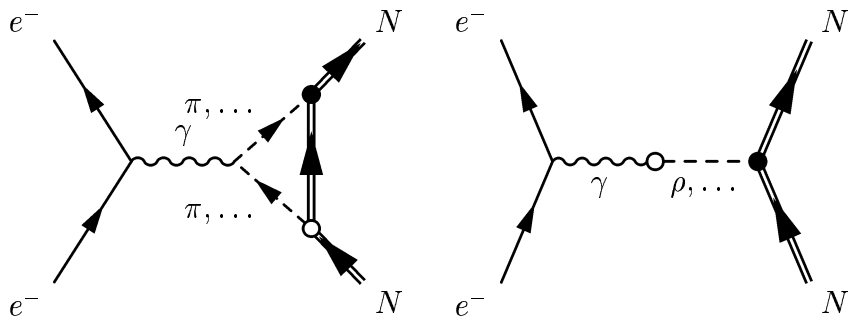

(a) Pion Loop (b) Rho Meson Pole

Figure 1.3: Some representative many quark diagrams that contribute to the electroweak radiative corrections. Filled circles represent parity violating meson nucleon vertices; open circles represent parity conserving vertices.

pling constant α_S is too strong in this kinematic regime to apply perturbative quantum chromodynamics (PQCD); hadronic models must be used to perform the calculations. Some representative diagrams used to model these corrections are shown in Figure 1.3.

The axial radiative corrections $R_A^{T=(0,1)}$ were originally calculated by Musolf and Holstein [MH90] and that calculation has since been updated [Zhu00]. In the latter paper the authors use heavy baryon chiral perturbation theory (HBχPT) to calculate the radiative corrections. They also include a number of diagrams not assessed in the original work. The authors of these papers chose to work in the "on-shell", or OSR, renormalization scheme. Their results have been broken down into contributions from one and many quark effects and can be found in Table 1.2* [Bei00].

*All radiative corrections used in this work are quoted in the modified minimal substitution, or $\overline{\text{MS}}$, scheme. The axial radiative corrections that appear in equation 1.70 are related to

Correction	One q	Many q	Heavy q	Total
$R_V^p(\overline{\rm MS})$	-0.054 ± 0.033	N/A	$\lesssim 10^{-4}$	-0.054 ± 0.033
$R_V^n(\overline{\rm MS})$	-0.0143 ± 0.0004	N/A	$\lesssim 10^{-4}$	-0.0143 ± 0.0004
$R_V^{(0)}(\overline{\rm MS})$	N/A	N/A	-10^{-4}	N/A
$R_A^{T=1}(\overline{\rm MS})$	-0.187	-0.04 ± 0.24	–	-0.227 ± 0.24
$R_A^{T=0}(\overline{\rm MS})$	0.072	0.01 ± 0.14	0.02	0.102 ± 0.14
$R_A^{(0)}(\overline{\rm MS})$	N/A	N/A	0.013	N/A

Table 1.2: Electroweak radiative corrections to the vector and axial vector nucleon form factors. The $R_V^N(\overline{\rm MS})$ come from Ref. [Mus94] and $R_A(\overline{\rm MS})$ come from Ref. [Bei00]. The radiative corrections evaluated in the $\overline{\rm MS}$ renormalization scheme are used in this work. The factors $R_V^{(0)}$ and $R_A^{(0)}$ are absorbed into the values of G_M^s and $G_A^e(T=1)$ reported in this work.

The vector corrections R_V^N were extracted from Ref. [MR90] by the authors of Ref. [Mus94]. Only one quark diagrams were evaluated, but an error was assigned based on a consideration of the many quark effects. These results are shown in Table 1.2. The authors of this calculation worked in the modified minimal substitution ($\overline{\rm MS}$) renormalization scheme; the axial vector results have been recast into this same scheme. No calculation of $R_V^{(0)}$ or $R_A^{(0)}$ has been performed as far as one or many quark effects are concerned; these corrections are absorbed into the values of G_M^s and $G_A^e(T=1)$ reported in this work.

Table 1.3 contains all the information necessary to calculate the weak and electromagnetic form factors at finite Q^2. Under the assumption of SU(3) flavor symmetry, the SU(3) octet axial form factor G_A^8 is determined by hyperon beta decay [Mus94]. The form factor is given by the ratio of axial vector to vector

the axial corrections of this section in the following way: $R_A^1 \equiv R_A^{T=1}$ and $R_A^0 = \sqrt{3} R_A^{T=0} G_A^8$ [Mus94].

Quantity	Value	Reference
μ_p	2.792847337(29) n.m.	[Gro00]
μ_n	$-1.9130427(5)$ n.m.	[Gro00]
$G_A(Q^2=0)$	1.2670(35)	[Gro00]
$G_A^8(Q^2=0)$	0.217(43)	[Mus94, FJ01, Gro00]
$G_A^s(Q^2=0)=\Delta s+\Delta\bar{s}$	$-0.086(24)$	[FJ01, Ack99, Ade98]
M_V	0.843 (GeV/c^2)	[Höh76]
M_A	1.069(16) (GeV/c^2)	[Lie99]
λ_n	5.6	[Mus94]
$\sin^2\theta_W$	0.23117(16)	[Gro00]
G_F	1.16639×10^{-5} (GeV^{-2})	[Gro00]
α	$7.297352533(27)\times10^{-3}$	[Gro00]

Table 1.3: This table contains the quantities necessary to calculate the weak and electromagnetic form factors, A_p, and A_d.

coupling constants in the decay process $\Xi^- \to \Lambda + e^- + \bar{\nu}_e$: $G_A^{(8)} \equiv -\frac{\sqrt{3}}{2}\frac{g_A(\Xi^-)}{g_V(\Xi^-)} = -\frac{\sqrt{3}}{2}(-0.25\pm0.05) = 0.217\pm0.043$ [Mus94, FJ01, Gro00]. This factor is evolved to $Q^2 = 0.1$ (GeV/c)^2 according to equation 1.56.

1.3 Predictions

There have been many predictions for $\mu_s \equiv G_M^s(Q^2=0)$ using a variety of models as is obvious from Figure 1.4 and Table 1.4. Figure 1.4 plots several theoretical predictions for μ_s, the values and references of which are listed in Table 1.4. The figure also shows the first published experimental result for μ_s based on low statistics data taken by the SAMPLE collaboration in 1995 and 1996 and using the Q^2 dependence of Hemmert *et al.* [Mue97a, HMS98]. This section will present an overview of the various models used to calculate μ_s. An

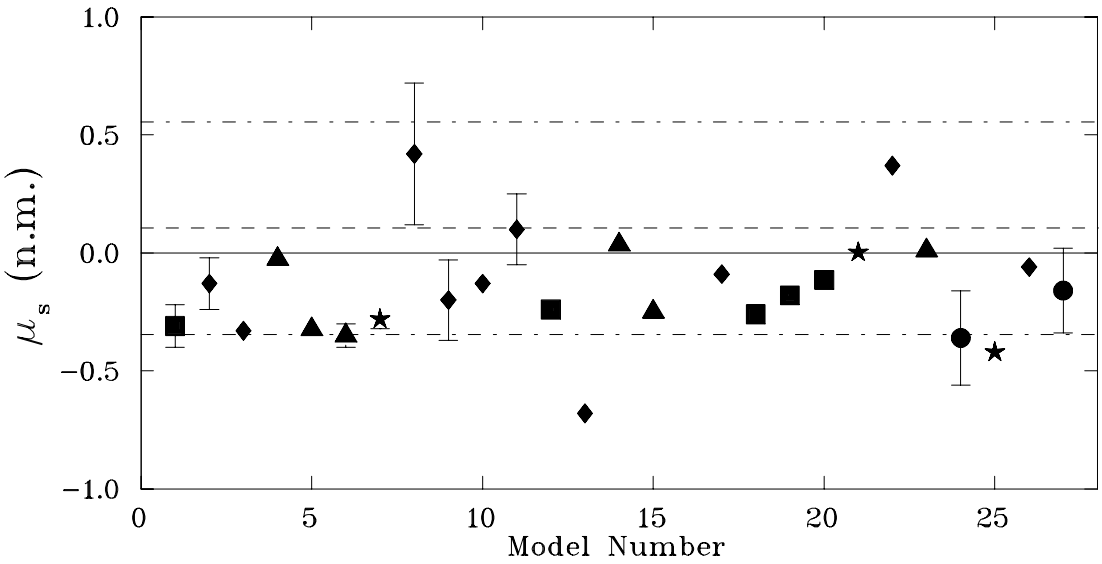

Figure 1.4: A graph of various model predictions for $\mu_s \equiv G_M^s(Q^2 = 0)$. Squares are poles model predictions, triangles are loops model predictions, stars are loops and poles model predictions, diamonds are predictions from other models, and circles are lattice QCD predictions. See Table 1.4 for the models and values of particular data points. The dashed line corresponds to the original SAMPLE result for G_M^s evolved to $Q^2 = 0$ [Mue97a, HMS98]. The dotted-dashed lines are the statistical, systematic, and theoretical errors added in quadrature.

alternative interpretation of the axial electroweak radiative corrections in terms of the nucleon's anapole moment will be discussed in Section 1.3.2.

1.3.1 G_M^s

The models used to make predictions about μ_s can be broken down into two broad categories that indicate where the nucleon strangeness originates: poles and loops. As shown in Table 1.4 there is a wide range of results between categories and between results in a given category. Most of the models discussed are variants of chiral perturbation theory (χPT) where the chiral symmetry of QCD for the three

Model Type	Reference	Model Number	μ_s (n.m.)
Poles	[Jaf89]	1	-0.31 ± 0.09
Poles	[HMD96]	12	-0.24 ± 0.03
Poles	[RMI97]	16	1.85 ± 2.2
Poles (3)	[For97]	18	-0.26
Poles (4)	[For97]	19	-0.18
Poles (6)	[For97]	20	-0.114
Loops (CBM)	[KHP92]	4	-0.0260
Loops (NRQM)	[KHP92]	5	-0.0324
Loops	[MB94]	6	$-0.31 \rightarrow 0.40$
Loops	[RMI97]	15	-0.25
Loops	[MM97]	23	0.010
Loops	[GI97]	14	0.035
Loops and Poles	[CFN93]	7	$-0.24 \rightarrow -0.32$
Loops and Poles	[Mei97]	21	0.003
Loops and Poles	[HRM99]	27	-0.42
SU(3) Skyrme (broken)	[PSW91]	2	-0.13
SU(3) Skyrme (unbroken)	[PSW91]	3	-0.33
SU(3) Chiral Hyperbag	[HP93]	8	0.42 ± 0.30
SU(3) Chiral Hyperbag	[HPM97]	22	0.37
SU(3) Chiral Color Dielectric	[PS94]	9	$-0.030 \rightarrow -0.20$
NJL Soliton	[Wei95]	11	$-0.05 \rightarrow 0.25$
SU(3) Chiral Quark-Soliton	[KWG97]	13	-0.68
Light-Cone Quark	[Ito95]	10	$-0.125 \rightarrow -0.146$
Chiral Quark	[RMI97]	17	-0.09
Chiral Quark	[HRG00]	26	-0.05
Lattice QCD	[DLW98]	24	-0.36 ± 0.20
QCD Equalities	[LT00]	27	-0.16 ± 0.18

Table 1.4: Predictions for μ_s from various models. The numbers in the third column give the corresponding data points in Figure 1.4.

lightest quark flavors is exploited to relate observables or use certain measured quantities to predict others.

In addition to the predictions based on nucleon models there are a few results from lattice QCD. This method probably offers the best hope for a strong prediction in the future once the computational power and techniques have evolved to the point of being able to make reliable calculations of low Q^2 quantities.

Most of the theoretical work on G_M^s has focused on the $Q^2 = 0$ limit. In order to compare the experimental result with theory it is necessary to know the Q^2 dependence of G_M^s. A recent calculation by Hemmert *et al.* provides upper and lower bounds on the Q^2 dependence; their result will be discussed at the end of the section [HMS98].

Poles Models

In the class of models known as poles, the nucleon strangeness arises not from the nucleon itself, but from its coupling to strange mesons. A representative Feynman diagram associated with these calculations is shown in Figure 1.5. The main idea is that the exchanged boson fluctuates into an isoscalar meson, an ω or a ϕ, which then interacts with the nucleon. The ϕ and the ω can both carry strangeness since they are linear combinations of strange ($\phi_0 = |s\bar{s}\rangle$) and

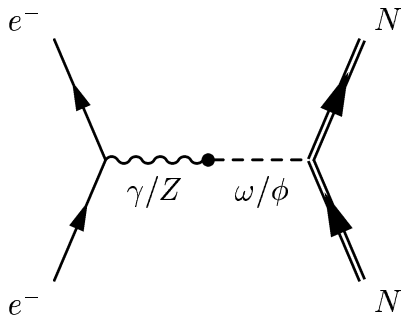

Figure 1.5: The primary Feynman diagram in poles models calculations.

non-strange $\left(\omega_0 = \frac{1}{\sqrt{2}}(|u\bar{u}\rangle + |d\bar{d}\rangle)\right)$ base states [Jaf89]:

$$|\omega\rangle = \cos\eta|\omega_0\rangle - \sin\eta|\phi_0\rangle \tag{1.78}$$

$$|\phi\rangle = \sin\eta|\omega_0\rangle + \cos\eta|\phi_0\rangle \tag{1.79}$$

where the mixing angle η has been measured and is quite small (0.053 ± 0.005) [Jai88].

The poles models, or dispersion analysis, calculations are based on the work of Höhler *et al.* from the 1970s [Höh76]. The central idea is to parameterize the isoscalar Dirac and Pauli form factors $F_i^{T=0} \equiv (F_i^p - F_i^n)/2$ with a three pole fit to experimental data:

$$F_i^{T=0} = \frac{a_i(\omega)}{m_\omega^2 - q^2} + \frac{a_i(\phi)}{m_\phi^2 - q^2} + \frac{a_i(V)}{m_V^2 - q^2} \tag{1.80}$$

The first and second terms are identified with the coupling of nucleons to $\omega(780)$ and $\phi(1020)$ mesons. The third term is an effective term summarizing contributions from unknown higher mass singularities. The various fit parameters $a_i(V)$ and m_V were extracted by the authors of Ref. [Höh76]. The three pole form is motivated by the success of dipole fits to the Q^2 dependence of the isoscalar

Dirac form factors, the same dependence used in equations 1.54 and 1.55:

$$F_i^{T=0}(Q^2) = \frac{F_i^{T=0}(0)}{(1 - Q^2/M_V^2)^2} + O(\frac{q^2}{4M_N^2}). \tag{1.81}$$

While M_V is very close in mass to that of $\omega(780)$, considering the ω as the sole meson contribution would only lead to a monopole form, the other two terms are necessary to get the dipole form. It should be pointed out that the primary advantage of poles models are their independence from any model of the nucleon and their strong grounding in experimental data.

Jaffe was the first to use the work of Höhler *et al.* to calculate μ_s [Jaf89]. He wrote dispersion relations for the nucleon matrix elements of the isoscalar electromagnetic current, $J_\mu^{T=0} = \frac{1}{6}(\bar{u}\gamma_\mu u + \bar{d}\gamma_\mu d) - \frac{1}{3}\bar{s}\gamma_\mu s$, $(F_i^{T=0})$ and the strange vector current, $J_\mu^s = \bar{s}\gamma_\mu s$, (F_i^s). Combining the information on $F_i^{T=0}$ from Höhler's three pole fit with some asymptotic constraints on the Q^2 behavior of the form factors, Jaffe was able to solve for all of the parameters in his dispersion relations and extract numbers for F_i^s. The strange magnetic moment is simply equal to $F_2^s(Q^2 = 0)$. In 1996 Mergell, Meißner, and Drechsel [MMD96] updated Höhler's fits of electromagnetic nucleon form factors to include new experimental data and theoretical refinements. Chief among the improvements was improved information on $\rho - \omega$ mixing and large-Q^2 constraints suggested by perturbative quantum chromodynamics (PQCD), as well as the improved data set on the isoscalar form factor. Hammer, Meißner, and Drechsel [HMD96] updated Jaffe's results for μ_s based on the updated Höhler fits. They also used input from PQCD

to implement new asymptotic constraints on the F_i:

$$F_i^{(T=0)}(q^2) = \left(\sum_j \frac{a_i(j) L^{-1}(m_j^2)}{m_j^2 - q^2} \right) L(q^2) \tag{1.82}$$

$$L(q^2) = \left[\ln \left(\frac{\Lambda^2 - q^2}{Q_0^2} \right) \right]^{-\lambda} \tag{1.83}$$

where $\Lambda = 9.73(GeV/c)^2$, $Q_0^2 = 0.35(GeV/c)^2$, and $\lambda = 2.148$ are parameters from QCD.

Ramsey-Musolf and Ito performed a poles model calculation using only the lowest two poles of the Höhler fits, the ones most likely to be associated with real resonances [RMI97]. This made it unnecessary to employ large-Q^2 constraints to determine the residue of the unknown pole, but the dipole Q^2 dependence at low Q^2 was preserved.

Forkel also released a result based on the updated fits [For97]. He implemented new asymptotic constraints from QCD as well, but chose to do so by extending the three pole fit to higher numbers of terms. The author opted to work with a four pole and a six pole set, in addition to simply updating the three pole results. The motivation for the four pole and six pole forms is the differing asymptotic Q^2 constraints of extrinsic and intrinsic radiative corrections. It is unclear which set of constraints should dominate. This is unfortunate because of the wide variation in results between the two (see Table 1.4).

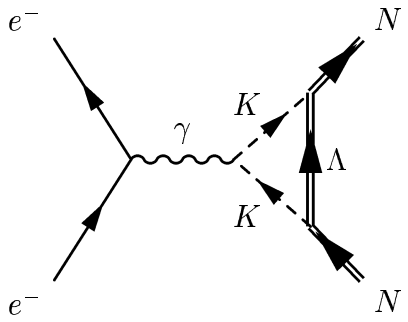

Figure 1.6: The primary Feynman diagram in loop model calculations.

Kaon Loop Models

A great deal of work has been done in predicting μ_s on the basis of kaon loop models. The primary shared feature of these models are Feynman diagrams where a nucleon combines with a $q\bar{q}$ pair to form a meson and an intermediate baryon state. The meson and baryon later recombine as the $q\bar{q}$ pair annihilates and the original nucleon is left in the final state. This class of models is known as kaon loops because the only Feynman diagrams that contribute to strange matrix elements are those involving K mesons (kaons) and strange baryon states. Figure 1.6 shows the relevant Feynman diagram. The primary difference between calculations of this type is the model used to describe the nucleon.

Koepf, Henley, and Pollock [KHP92] used models that incorporated bag-like hadrons, hadrons with finite extent and internal structure. They examined two different models that differ in their description of the structure and size of the nucleon: the cloudy bag model (CBM) and the non-relativistic quark model (NRQM). The physical extent of the nucleon enters in a renormalization of the baryon wave function. A form factor $v(k)$ containing information on the size and

structure of the nucleon bag was used to describe the two different models. The cloudy bag model used this form factor [TTM80, TTM81]

$$v(k) = \frac{3j_1(kR)}{kR} \approx \exp[-0.106(kR)^2] \tag{1.84}$$

whereas the non-relativistic quark model used this one [NO82]

$$v(k) = \exp\left[-\frac{1}{6}(kr)^2\right]. \tag{1.85}$$

The sizes of the bag, r and R, were the only unknowns in the two models. These parameters were extracted from fits to the nucleon magnetic moments and charge radii. After fixing r and R the kaon loop calculations were performed.

Musolf and Burkhardt also performed a calculation based on kaon loops using the linear σ model [MB94]. Their calculation differed from those of Koepf *et al.* in two respects. First, they did not attempt to fit to existing electromagnetic form factor results. Instead, they used what data they needed to perform the calculation and extracted the electromagnetic form factors for comparison. Second, they framed their calculation in such a way that the Ward-Takahashi identity was satisfied. This involved the application of form factors and new Feynman diagrams (known as "seagull" diagrams) at the meson-nucleon vertices. The addition of the seagull diagrams implies that four diagrams must be calculated for each meson-intermediate baryon combination: two diagrams where the boson probe couples to the meson or baryon individually and two (the seagull diagrams) where the probe couples at the meson-baryon vertices. The meson-

baryon vertex form factors used were the ones that determine the Bonn potential from baryon-baryon scattering:

$$F(k^2) = \left[\frac{m^2 - \Lambda^2}{k^2 - \Lambda^2}\right] \tag{1.86}$$

where m and k are the mass and momentum of the meson. The cutoff factor, Λ, from the Bonn potential is 1.2 – 1.4 GeV. Ramsey-Musolf and Ito updated this result using the nonlinear σ model [RMI97].

Malheiro and Melnitchouk investigated the effects of relativistic covariance on the kaon cloud model [MM97]. The kaon cloud models generally consider single meson loops only and omit contributions from many-body currents. Lorentz invariance is violated by the latter assumption and the violation leads to the appearance of unphysical form factors. The authors formulated a technique for removing the effects of the spurious form factors.

One of the more recent results based on this model was put forth by Geiger and Isgur [GI97]. The main difference between this model and earlier ones is that all possible strange intermediate states are included in the sum, not just the lowest-lying ones. The authors claim that this sum over all states is necessary in order to preserve the OZI rule and retain the simple quark model's success in explaining the observed hadron energy spectrum.

Loops and Poles Models

Cohen, Forkel, and Nielsen linked the poles and loops calculations together using vector meson dominance (VMD) [CFN93]. In the VMD model the nucleon form factors are expressed in the following way:

$$\begin{pmatrix} F_n^0(q^2) \\ F_n^s(q^2) \end{pmatrix} = \hat{f}_v(q^2, \eta) \begin{pmatrix} F_{ni}^0(q^2) \\ F_{ni}^s(q^2) \end{pmatrix} \tag{1.87}$$

where $\hat{f}_v(q^2, \eta)$ is a 2×2 matrix containing vector meson propagators and the F_{ni} are intrinsic form factors that describe the coupling of the vector meson to the nucleon. The variable η describes the mixing between the ω and the ϕ. The pole description comes in the vector meson propagators, which look like the first two poles (ω, ϕ) of that model. The kaon loops come in the intrinsic form factors F_{ni}; the authors used the work of Musolf and Burkhardt [MB94] as a basis for their calculation of these factors.

Meißner *et al.* also performed a calculation that joined the poles and loops models together. The authors did not incorporate ω-ϕ mixing in their model, but did consider Σ loops in addition to kaon loops. In the end their calculation only included contributions from two poles, ω and a generic one denoted S at higher mass.

A recent calculation by Hammer and Ramsey-Musolf further refined the loops-poles model [HRM99]. The VMD approximation was dropped allowing contributions from multi-meson intermediate states in the dispersion relations. Again,

only kaon loops were included in the calculation.

Other Models

There are other model predictions for μ_s that defy easy categorization into loops or poles. These models tend to be related to the loop models in that measured strangeness arises from kaons or other strange mesons in the nucleon. The predictions are differentiated by the model of the nucleon that is employed to perform the calculation. Several of these predictions are listed in Table 1.4.

Lattice Quantum Chromodynamics

In recent years lattice quantum chromodynamics (lattice QCD) calculations have begun to make predictions for μ_s. Lattice QCD is a computational technique for performing calculations from first principles of QCD on a lattice of spacetime points. Dong, Liu, and Williams performed a calculation using a $16^3 \times 24$ lattice in the quenched approximation [DLW98], and a few other calculations have been performed to date. However, lattice calculations are still regarded as being in their infancy for making predictions of μ_s.

Another approach to using lattice QCD as a predictor of μ_s is the so-called QCD equalities approach [Lei95, Lei96, LT00]. By exploiting the symmetries inherent in the QCD path integral it is possible to extract a set of sum rules, or equalities, that express the magnetic moments of the SU(3) octet baryons in terms of contributions from valence and sea quarks, including G_M^s [LT00]. Lattice

QCD calculations provide some of the inputs used to solve the sum rules for G_M^s. This technique has been refined several times therefore only the most recent value is shown in Table 1.4 [LT00].

Q^2 Dependence

The SAMPLE experiment is performed at a finite Q^2 of 0.1 (GeV/c)^2, so it is necessary to know the Q^2 dependence of G_M^s in order to compare the result with the predictions. A recent calculation by Hemmert *et al.* uses heavy baryon χPT (HBχPT) to place limits on the Q^2 dependence [HMS98, HKM99]. The lower bound determined by their calculation is given by

$$G_{M,L}^s(Q^2) = \mu_s + \frac{\pi m_N M_K}{(4\pi F_M)^2}\frac{2}{3}(5D^2 - 6DF + 9F^2)f(Q^2) \tag{1.88}$$

$$f(Q^2) = -\frac{1}{2} + \frac{4 + Q^2/M_K^2}{4\sqrt{Q^2/M_K^2}}\arctan\left(\frac{\sqrt{Q^2}}{2M_K}\right) \tag{1.89}$$

where m_N and M_K are the nucleon and kaon mass, respectively, F and D are the conventional axial meson-baryon couplings, and the meson decay constant $F_M \equiv \frac{1}{2}(F_\pi + F_K) = 102$ MeV*. The function $f(Q^2)$ is approximately linear for $Q^2 \lesssim 0.5$ (GeV/c)^2. The authors also place an upper bound on the dependence via the following equation:

$$G_{M,U}^s(Q^2) = \mu_s + \mu^{T=0} - G_M^{T=0}(Q^2) \tag{1.90}$$

*The pion and kaon decay constants quoted here are related to their values quoted by the Particle Data Group via $F_i = \frac{1}{\sqrt{2}} f_i^{\mathrm{PDG}}$ [Gro00].

where $\mu^{T=0} \equiv \mu_p + \mu_n$ and $G_M^{T=0} \equiv G_M^p + G_M^n$. Hemmert and colleagues used the first published SAMPLE result [Mue97a]

$$G_M^s(Q^2 = 0.1\text{GeV}^2) = 0.23 \pm 0.37 \pm 0.15 \pm 0.19 \tag{1.91}$$

to make their prediction for μ_s. They applied the corrections due to equations 1.88 and 1.90 to the central value of the SAMPLE result in order to place an upper and lower bound on μ_s, 0.03 – 0.18 n.m.

1.3.2 G_A^e

The expression for the nucleon's axial form factor G_A^e from equation 1.70 can be rewritten in the following way [Has00a]:

$$G_A^e = -(1 + R_A^1)G_A\tau_3 + R_A^0 + (1 + R_A^{(0)})G_A^s \tag{1.92}$$

$$G_A^e = G_A^Z + \eta F_A + R^e \tag{1.93}$$

where G_A^Z is a contribution from single Z exchange, R^e is a radiative correction, $\eta = \frac{8\pi\sqrt{2}\alpha}{1-4\sin^2\theta_W}$, and F_A is the intrinsic anapole moment of the nucleon. The anapole moment is a parity violating electromagnetic coupling of an electron to a nucleon [Zel57]. The existence of an anapole moment was first suggested by Zeldovich shortly after the discovery of parity violation in the weak interaction in the 1950s. This moment, as indicated above, arises from a parity odd, but time reversal even, electromagnetic interaction. One mechanism for generating an anapole moment is the exchange of weak bosons between quarks in the nucleon

at the same time that a photon is exchanged between the nucleon and electron. Operationally the anapole moment arises from an axial vector coupling of the photon to the nucleon and a vector coupling to the electron.

To date the nuclear anapole moment has been the subject of more scientific interest than the nucleon anapole moment. In 1980 Flambaum and Khriplovich suggested that electromagnetic interactions between atomic electrons and nuclei would result in a nuclear-spin dependence that could be measured in atomic parity violation experiments [FK80]. This spin dependence could arise from the anapole moment or from direct exchange of a Z^0 boson between the electron and the nucleus, however the anapole moment contribution is expected to dominate in nuclei with large atomic number A. In direct Z^0 exchange only the last unpaired nucleon contributes to the axial vector coupling at the nucleus and the vector electron coupling is suppressed by $(1 - 4\sin^2\theta_W)$ [Hax97]. More importantly the anapole moment grows as $A^{2/3}$, thus for large A nuclei the parity violating electromagnetic interaction can overshadow the parity violating weak interaction [FKS84].

Since the publication of Flambaum and Khriplovich's paper three atomic parity violation experiments have reported on the nuclear anapole moment. The first was a measurement of the parity violating electric dipole transition between the $6S$ and $7S$ states of atomic cesium [NMW88]. They reported a value of 0.72(39) for κ_a, a dimensionless coupling constant directly proportional to the anapole

moment. A later experiment that measured parity violating optical rotation near the $6P_{1/2} \rightarrow 6P_{3/2}$ magnetic dipole transition in thallium reported a result of κ_a consistent with zero (-0.22 ± 0.30) [Vet95]. Definitive evidence for the existence of the nuclear anapole moment came in 1997 from another measurement of the electric dipole transition $6S \rightarrow 7S$ in cesium with improved statistical and systematic precision [Woo97]. Their result was $\kappa_a = 0.114 \pm 0.019$, a 6σ deviation from zero [Hax97].

As indicated in equation 1.93, the SAMPLE measurements are potentially sensitive to the nucleon's intrinsic anapole moment. The diagrams that contribute to the anapole moment are the many quark diagrams discussed in Section 1.2.4; the anapole moment shows up as an electroweak radiative correction to the tree level G_A^e. Zhu *et al.* derive the following expressions in chiral perturbation theory for the axial corrections due to the anapole moment [Zhu00]:

$$R_A^{T=0}|_{\text{anapole}} = -\frac{8\sqrt{2}\pi\alpha}{G_F\Lambda_\chi^2}\frac{1}{1-4\sin^2\theta_W}\frac{a_s}{g_A} \tag{1.94}$$

$$R_A^{T=1}|_{\text{anapole}} = -\frac{8\sqrt{2}\pi\alpha}{G_F\Lambda_\chi^2}\frac{1}{1-4\sin^2\theta_W}\frac{a_v}{g_A} \tag{1.95}$$

where $\Lambda_\chi = 4\pi F_\pi$ is the chiral symmetry breaking scale and the anapole moment is given by the quantity $a_s + \tau_3 a_v$. The values of these axial, many quark corrections are listed in Table 1.2. The combination of A_p and A_d is sensitive to $G_A^e(T=1) \propto R_A^{(T=1)} \propto a_v$. A deviation from the theoretical value of -0.83 ± 0.26 could possibly signal a stronger than expected nucleon anapole moment or physics beyond the standard model [Zhu00].

1.4 Summary

Measurements of the parity violating cross section asymmetry for the scattering of longitudinally polarized electrons from protons and deuterons A_p and A_d make it possible to extract the proton's neutral weak magnetic form factor G_M^{Zp} and the nucleon's isovector axial form factor $G_A^e(T=1)$. The neutral weak magnetic form factor is as important and fundamental as the magnetic form factor due to the electromagnetic interaction. Under the assumption of isospin symmetry it is possible to determine the strange magnetic form factor of the proton G_M^s from G_M^{Zp}. This form factor probes the contribution of strange quarks to low energy properties of the nucleon and, by extension, the contribution of the quark-antiquark sea. The form factor $G_A^e(T=1)$ is potentially sensitive to the parity violating electromagnetic interaction known as the anapole moment.

Chapter 2

Experiment

2.1 Overview

The SAMPLE experiment is located at the MIT–Bates Linear Accelerator Center in Middleton, MA. This facility consists of a linear accelerator (linac) and two experimental halls for the installation of detectors and targets: the North Hall and the South Hall. The linac is capable of providing pulses of polarized electrons at a rate of 600 per second (Hz) with energies up to approximately 10^9 electron-Volts (1 GeV). The SAMPLE target and detector were installed in the North Hall in 1993. Data have been taken in several periods in 1995, 1996, 1998, and 1999. Results from the data collected in 1995 and 1996 were published in Ref. [Mue97a]. The data upon which this dissertation is based comes from a measurement of the elastic $\vec{e}$-p asymmetry A_p performed in 1998 and represents 115 Coulombs of electrons delivered to the SAMPLE target [Spa00]. In 1999, the quasielastic $\vec{e}$-d

asymmetry A_d was measured for the first time [Has00a].

The experimental technique is very simple: measure the yield* in the detector as the beam polarization is flipped between states of positive and negative helicity. The yield asymmetry A_Y can be calculated by taking the difference in yields over the sum:

$$A_Y = \frac{Y^+ - Y^-}{Y^+ + Y^-} \tag{2.1}$$

where Y^+/Y^- is the yield for positive/negative helicity electrons. The yield is proportional to the cross section, therefore the yield asymmetry is proportional to the parity violating cross section asymmetry, $A_Y \propto A_p$. The extraction of A_p from A_Y is the subject of Chapter 3.

Despite the simplicity of the technique the experiment is challenging because A_Y is only a few parts in 10^6 (ppm). To make a meaningful measurement of such a small asymmetry it is necessary to limit possible sources of systematic error to the 10^{-7} level and collect enough data to get the statistical error down to the same level. Some potentially large sources of systematic errors are helicity correlated beam parameter differences. These are changes in a beam quality, size, shape, position, charge, etc., as a function of helicity. If the yield in the detector changes as a function of some beam parameter and that parameter exhibits a helicity correlated difference, then the detector will measure a false asymmetry which can

*All yields in this experiment are normalized to the incident beam charge therefore when yield is used in this dissertation it is short for "yield normalized to incident charge".

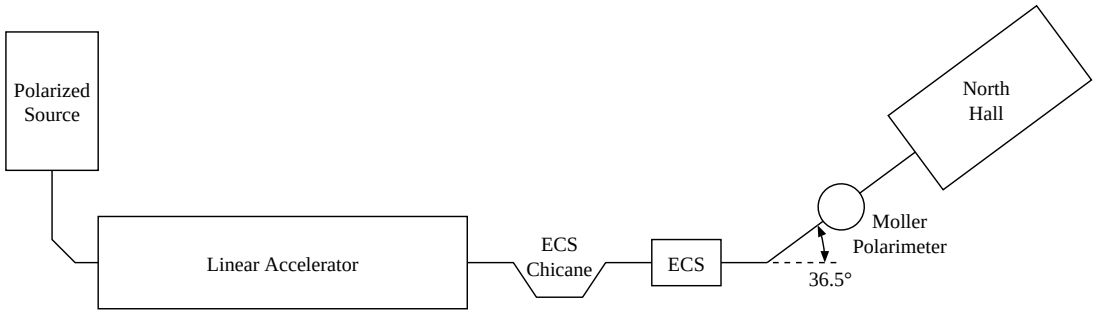

Figure 2.1: A schematic of the Bates accelerator facility.

dilute or obscure the parity violating asymmetry. The experimental apparatus has been designed to limit helicity correlated beam parameter differences, the measures taken are discussed in this chapter and Appendix A. The question of how to deal with residual false asymmetries is addressed in Section 3.2.

Figure 2.1 contains a schematic of the accelerator layout important to the SAMPLE experiment. Section 2.2 describes the polarized source, accelerator, energy compression system (ECS), and the beam monitors. The Møller polarimeter is discussed in Section 2.3. The contents of the North Hall, the target and the detector, are described in Sections 2.4 and 2.5 and the data acquisition electronics are described in Section 2.6. Section 2.7 discusses several supplemental measurements that are necessary to support or extract the physics asymmetry.

2.2 Polarized Source and Accelerator

In order to perform this experiment, the accelerator must deliver a stable, high intensity beam of 200 MeV polarized electrons to the North Hall. Section 2.2.1

describes the apparatus used to generate the polarized electrons. In Section 2.2.2, the details of the accelerator that are pertinent to the SAMPLE experiment are discussed. The various devices used to measure the properties of the beam are the subject of Section 2.2.3.

2.2.1 Polarized Source

The technique used to generate polarized electron beams is fundamentally different from the one used to generate unpolarized, or thermionic, beams. As the name suggests, thermionic beams are produced by heating a filament and accelerating the electrons that boil off while polarized electrons are generated via the photoelectric effect. Circularly polarized photons with a wavelength of approximately 750 nm are made incident on a gallium arsenide (GaAs) crystal. The photons penetrate into the interior of the crystal and are absorbed by electrons whose energies are raised into the conduction band. These electrons have a net polarization due to the transitions allowed by the incident photon's polarization. In bulk GaAs the theoretical maximum polarization is 50%, but as the electrons diffuse to the surface of the crystal the polarization is reduced to less than 40% [Far99]. The fraction of electrons that escape the crystal, or the quantum efficiency (QE), is increased by a thin layer of cesium (Cs) deposited on the crystal surface [Far99].

A schematic of the Bates polarized electron source is shown in Figure 2.2.

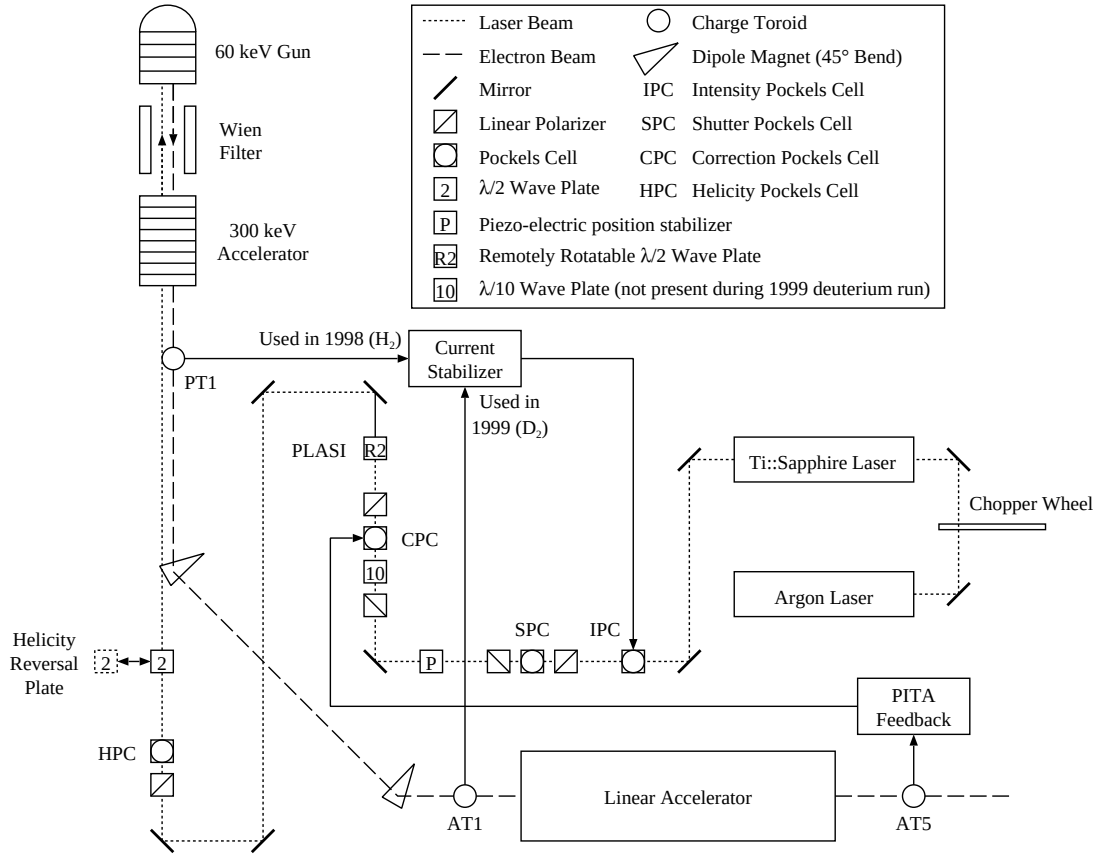

Figure 2.2: A schematic of the polarized electron source at the MIT–Bates Linear Accelerator.

The photon source is a titanium(Ti)::sapphire laser pumped by a continuous wave (CW) argon (Ar) ion laser. The beam from the Ar laser passes through a mechanical shutter wheel consisting of a metal disk pierced by 10 identical slits spaced equidistant around the rim. A motor spins the shutter wheel at 60 Hz resulting in a train of evenly spaced Ar laser pulses at 600 Hz, the operational frequency of the linear accelerator (Section 2.2.2). The pulses are approximately 280 μs long. The pulsed Ar laser beam pumps the Ti::sapphire laser and 750 nm, linearly polarized photons are emitted. The peak output power of the Ti::sapphire laser is 8 Watts, but the maximum power available at the crystal is approximately 3.5 W due to losses in the laser transport [Far99].

The polarized source uses several Pockels cells and linear polarizers in combination to generate circularly polarized light and to modulate the laser intensity. A Pockels cells is a birefringent crystal, a crystal with different indices of refraction n along the three orthogonal axes ($n_x \neq n_y \neq n_z$ where z points in the direction of light propagation) [Fow75]. The indices of refraction of a Pockels cell vary in direct proportion to an applied electric field which means that the phase difference $\Delta\phi$ between the x and y electric field components of the transmitted light is directly proportional to the applied electric field ΔV:

$$\Delta\phi = P\Delta V \tag{2.2}$$

where P is a known constant. When $\Delta\phi = \frac{N\pi}{2}$, where N is a positive or negative integer, and the incident linearly polarized light forms a 45° angle with the x and

y axes, the Pockels cell acts as a quarter wave plate and circularly polarized light is emitted. When $\Delta\phi = N\pi$ the Pockels cell acts as a half wave plate and the linear polarization is rotated by 90°. Any other value of $\Delta\phi$ results in a mix of linearly and circularly, or elliptically, polarized light.

The first Pockels cell in the polarized source is the intensity Pockels cell (IPC). The purpose of the IPC is to stabilize the electron beam current within a pulse by modulating the laser intensity. The beam current is measured in a charge toroid (PT1 in 1998 and AT1 in 1999) and the difference between the toroid signal and a reference signal is amplified and applied to the IPC. This has the effect of introducing a component of circular polarization to the laser light. The fraction of the light intensity corresponding to the induced circular polarization is absorbed in the first linear polarizer downstream of the IPC. The beam current stabilizer system* has a gain bandwidth of 100 MHz [Far99].

The next Pockels cell is the shutter Pockels cell (SPC). It is sandwiched between a pair of crossed linear polarizers and is set to function as a half wave plate. When the proper electric field is applied to the cell the incident light is transmitted otherwise the power is dumped in the downstream linear polarizer. The SPC is used to block all the laser light for 20 out of every 600 pulses while the rest of the source, accelerator, and detector fires normally. These blank pulses, which

*This system replaces the Conoptics LassII laser stability system that was used during 1995 and 1996 [Mue97b, For98].

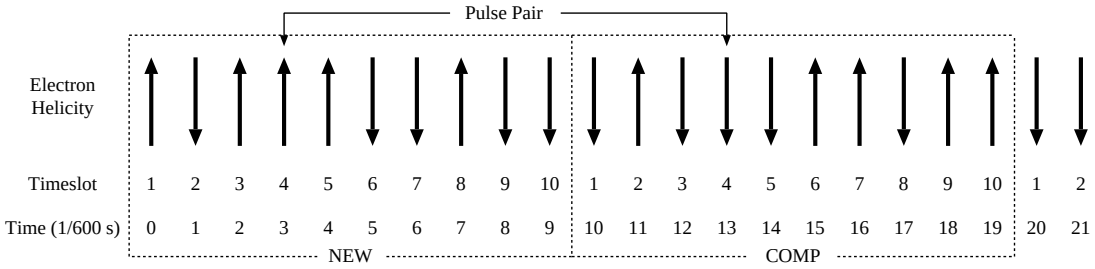

Figure 2.3: An example NEW and COMP sequence.

contain no electrons, are used to measure offsets in the electronics, or "pedestals", that are later subtracted from the signals due to pulses with electrons. The SPC is also used to shorten the length of pulses from the Ti::Sapphire laser from 280 μs to 25 μs.

The final Pockels cell operates as a quarter wave plate and generates the circularly polarized light necessary to knock polarized electrons out of the GaAs crystal. A pair of power supplies with opposite polarities is used to apply positive and negative fields to the helicity Pockels cell (HPC) and select the circular polarization of the light, left- or right-handed. The polarization can be switched on a pulse-to-pulse basis, at 600 Hz. The polarized source computer pseudorandomly selects the helicity of each pulse in a set of ten pulses, known as the NEW sequence, that spans exactly one cycle of the 60 Hz AC line frequency. The next set of ten pulses, known as the complement or COMP sequence, is chosen to have the opposite helicity of the corresponding pulse in the NEW sequence as shown in Figure 2.3. The yield asymmetry is formed between corresponding pulses in adjoining NEW and COMP sequences so that the two members of a pulse pair

are always separated by 1/60 s. By forming asymmetries in this way, false asymmetries due to 60 Hz noise in the electronics are eliminated. This method has the additional benefit of removing false asymmetries due to long-term drifts (much longer than 1/60 s) in the electronics. All of the pulse pairs in the experiment are averaged together to get the final A_Y.

Before striking the GaAs crystal, located at the top of the 60 keV gun, the circularly polarized laser beam passes through a region where a half wave plate can be manually installed. This half wave plate reverses the electron's helicity with respect to the electronics' helicity signal. Taking asymmetry data with this plate in and out is an effective means of searching for helicity correlated differences in the electronics. The parity violating asymmetry will reverse sign but the electronics asymmetry will not under insertion or removal of this plate.

There are three additional important optical elements in the polarized source prior to the HPC. The correction Pockels cell (CPC) is used to reduce helicity correlated beam current differences via PITA feedback, discussed in Section A.3. A piezo-electric device is used to reduce helicity correlated beam position differences in the experimental hall (Section A.2). A remotely controlled, rotatable half wave plate (PLASI) sets the overall intensity of the laser light.

The electrons that are knocked free of the crystal are accelerated to 60 keV and enter a region of crossed magnetic and electric fields known as a Wien filter. In route to the SAMPLE detector, the electron beam is bent 36.5° by a

series of dipole magnets. The dipoles cause the electron polarization to rotate an additional 16.6° due to the anomalous magnetic moment of the electron. By rotating the electrons' spin $-16.6°$ in the Wien filter before the beam enters the accelerator the electrons' spin will be longitudinal in the SAMPLE target.

The filter consists of a pair of electrostatic plates and a magnetic dipole. The electric and magnetic fields are set to cancel each other so that the electrons experience no net force; the spin of the electron is free to precess about the magnetic field without skewing the electrons' trajectory. The equation governing the spin precession is [Jac75]

$$\frac{d\mathbf{s}}{dt} = \frac{e}{mc}\mathbf{s} \times \mathbf{B}\left[\frac{g}{2}(1+\beta^2) - 2(1-\frac{1}{\gamma})\right] \tag{2.3}$$

where $\mathbf{s}$ is the electron's spin vector, $\mathbf{B}$ is the magnetic field vector, $\frac{g}{2}$ is the magnetic moment of the electron in units of Bohr magnetons $\left(\mu_B = \frac{e\hbar}{2m_e}\right)$, $\beta = \frac{v}{c}$, and $\gamma = \frac{1}{\sqrt{1-\beta^2}}$. The total spin rotation is determined by the following equation, assuming a perfect Wien filter of length L:

$$\theta = \frac{L}{c\beta}\frac{eB}{mc}\left[\frac{g}{2}(1+\beta^2) - 2\right]. \tag{2.4}$$

The details of setting the Wien filter correctly are discussed in Section 2.3.2. After exiting the Wien filter the electrons are accelerated another 300 keV before entering the accelerator.

2.2.2 Accelerator

The first stage of the accelerator is a chopper-prebuncher-buncher assembly which compresses some fraction of the electrons leaving the polarized source into a 25 μs long pulse and sweeps the rest out of the beamline. The pulse is accelerated to 200 MeV by a series of 12 radiofrequency (RF) acceleration cavities operating at a frequency of 2.856 GHz.

Quadrupole magnets are scattered throughout the linac and the North Hall. A single quadrupole magnet focuses the electron beam along an axis perpendicular to the particle trajectory and defocuses along the orthogonal one. By combining quadrupoles in pairs that focus in orthogonal planes a net focusing effect is achieved. These quadrupole pairs are essential for tuning the beam through the accelerator and into the North Hall.

There are also sets of solenoid magnets throughout the linac, mounted in back-to-back pairs. The solenoids focus the electron beam as well, but have an unfortunate side effect when working with polarized electrons. The solenoidal fields cause any tangential electron polarization to precess about the field lines, which lie along the electron's trajectory. Since the electron polarization is set to be away from longitudinal in the Wien filter to account for the $g-2$ precession in the bending dipoles, passage through the accelerator solenoids can cause the polarization vector to point out of the bend plane. If the electron polarization is not in the bend plane when the electrons reach the bending dipoles, then the

polarization will not be completely longitudinal when it reaches the target. The solenoids must be carefully calibrated at the beginning of the experiment so that there is no net ϕ rotation (rotation about the particle trajectory) through the accelerator. This calibration is discussed in Section 2.3.2.

At the end of the linac the electrons pass through the energy compression system (ECS) chicane which consists of four dipole magnets. The first dipole bends the electron beam away from, and the second one makes the electron trajectories parallel to, the beamline. The third and fourth dipoles reverse this process, bringing the electrons back onto the original beamline. The chicane is an energy dispersive region, the horizontal displacement of electrons in the chicane is proportional to the electron energy with higher energy electrons traveling closer to the original beamline. The transverse dispersion is 33 mm/% of the beam energy. A pair of slits in the chicane define the maximum energy spread of the beam by scraping off electrons outside the desired range. These slits are set so that there is a 33 mm opening about the central trajectory, corresponding to an allowed range of $\pm 0.5\%$. There is a beam position monitor (BPM) after the slits that measures the horizontal displacement of the beam and the energy due to the dispersive nature of the chicane. The signal from this BPM (ECSX) is recorded in the SAMPLE data stream (Section 2.6) and is used by the energy feedback system (Section A.1).

The primary purpose of the ECS chicane is to reduce the spread of electron

energies in a beam pulse [Fla91]. Higher energy electrons get bent less in the dipole fields than lower energy ones, therefore they travel a shorter path through the chicane and exit before the lower energy electrons. The electrons pass through another accelerating section with the phase set such that the amplitude of the RF field passes through zero at the center of the beam pulse. Energy is subtracted from the leading (high energy) edge of the pulse and added to the trailing (low energy) edge. The energy compression system reduces the average relative energy spread of the beam from $\pm 0.15\%$ to $\pm 0.014\%$ [Jac01].

Figure 2.4 contains a schematic of the beamline in the North Hall and Table 2.4 lists the distances between the important beamline elements and the center of the target. Signals from the BPMs, toroids, halo monitors, and luminosity monitors are all recorded into the SAMPLE data stream. The four steering coils (SSS1H, SSS1V, SSS2H, and SSS2V) are used to calibrate the SLAC-style BPMs (Section 2.2.3) in the North Hall by deflecting the electron beam a known amount and also to determine the quality of the beam tune. In a coil pulsing run the coils are activated in such a way that the beam maps out a known deflection in the North Hall. The detector yield is monitored to make sure there is no correlation between yield and beam deflection; a non-zero correlation would mean that the beam was scraping something along the beamline. Coil pulsing runs are performed after the beam has been off for an extended period of time.

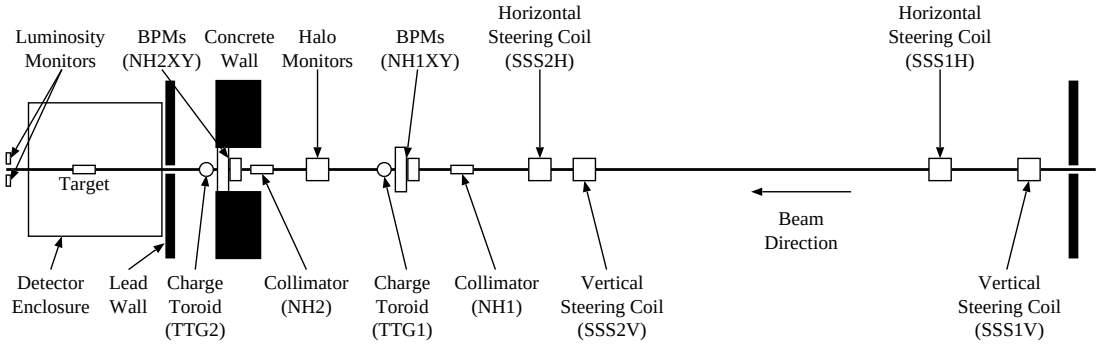

Figure 2.4: A schematic of the layout of beamline elements in the North Hall.

Name	Device	Distance (in)
North Hall Wall		684
SSS1V	Vertical Steering Coil	638
SSS1H	Horizontal Steering Coil	591
SSS2V	Vertical Steering Coil	468
SSS2H	Horizontal Steering Coil	445
NH1(X/Y)	SLAC-style BPMs	334
HA(1/2)(X/Y)	Halo Monitors	249
NH2(X/Y)	SLAC-style BPMs	172
Lead Wall		104
LUMI(L/R)	Luminosity Monitors	96

Table 2.1: Distances between North Hall beamline elements and the center of the target.

2.2.3 Beam Monitors

The accelerator operators employ a variety of devices throughout the accelerator to monitor the electron beam as it is tuned. The experiment records data from several of them as well, on a pulse-by-pulse basis, for later analysis. These devices can be grouped by the beam parameter they monitor: beam position, charge, energy, halo, and luminosity. Each of these devices is discussed in this section with the exception of the energy monitor (it was discussed in the previous section).

Beam Position Monitors

There are two types of non-destructive beam position monitor that can be used during data taking: NIKHEF and SLAC. The NIKHEF-style BPMs are used in the linac, most prominently as the BPM (ECSX) that monitors the beam energy in the magnetic chicane. SLAC-style BPMs are used in the North Hall to measure the beam position on a pulse-by-pulse basis for inclusion in the SAMPLE data stream. The signal is proportional to the product of the beam position and the beam charge, therefore the signal must be normalized to the charge in a pulse in order to extract the position information [Far76].

There are also two types of destructive monitors that are only used while the beam is being tuned; their purpose is to determine the location and size of the electron beam at a given point in the accelerator. The most common such device is a beryllium oxide (BeO) flip target paired with a television camera. The

target can be remotely inserted into the beamline by an accelerator operator and scintillates in the visible spectrum when struck by the electron beam. An image of the target is transmitted to the operator via the television camera and allows the position and size of the beam in the x-y plane to be roughly determined. A more quantitative measurement of position and size is provided by "lutes". A lute consists of a pair of crossed aluminum wires that are pushed across the beamline. When a beam electron strikes one of the wires a current is generated via secondary electron emission. The current in the wires is measured as they are stepped across the beam and an accurate profile is generated.

Charge Monitors

Charge toroids are used to measure the beam current. A toroid is a wire-wrapped iron doughnut that encircles the beamline. The passage of electrons through the doughnut induces a magnetic flux in the iron. This flux in turn induces a voltage in the wire that can be measured electronically. The toroid is calibrated by passing a known amount of charge through the doughnut using a loop of wire (Q-loop). The output of the two toroids in the North Hall are read into the SAMPLE data stream and are used to normalize the the other monitors and detectors in the experiment.

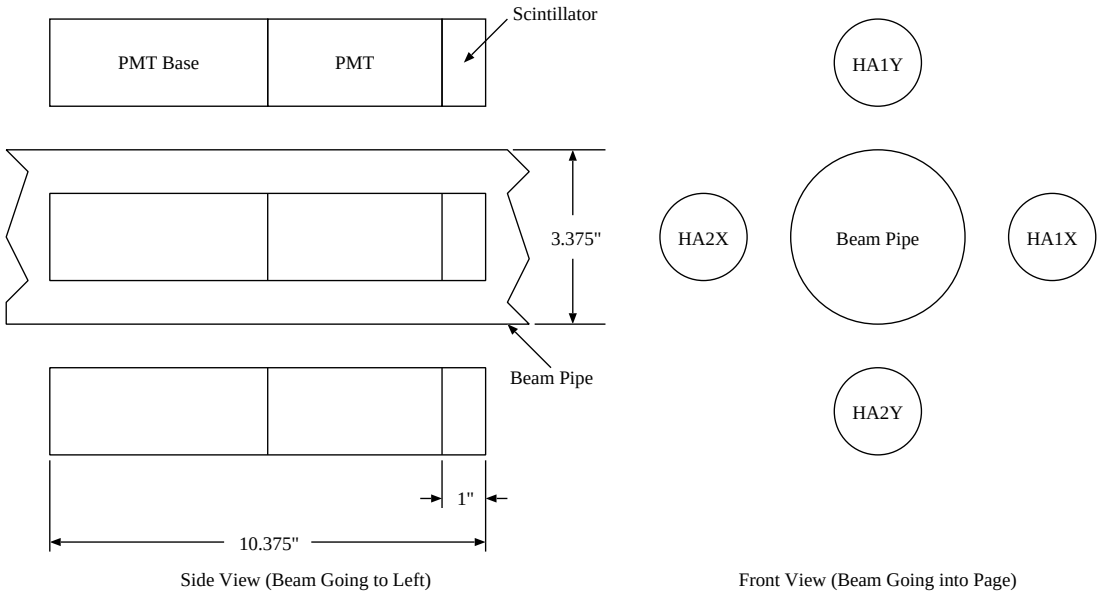

Figure 2.5: A schematic of the halo monitor array.

Halo Monitors

There is an array of halo monitors in the North Hall. A schematic can be found in Figure 2.5. The purpose of these monitors is to measure the amount of background radiation that accompanies a pulse of electrons. A halo monitor consists of a two inch diameter photomultiplier tube (PMT) coupled to a one inch thick disk of plastic scintillator. Incident radiation generates photons in the scintillator that are detected by the PMT. The PMT signal is digitized and read into the SAMPLE data stream. These monitors serve as a measure of beam quality, if the halo signal grows too large it is usually indicative of an excess amount of beam scraping off of the slits in the magnetic chicane.

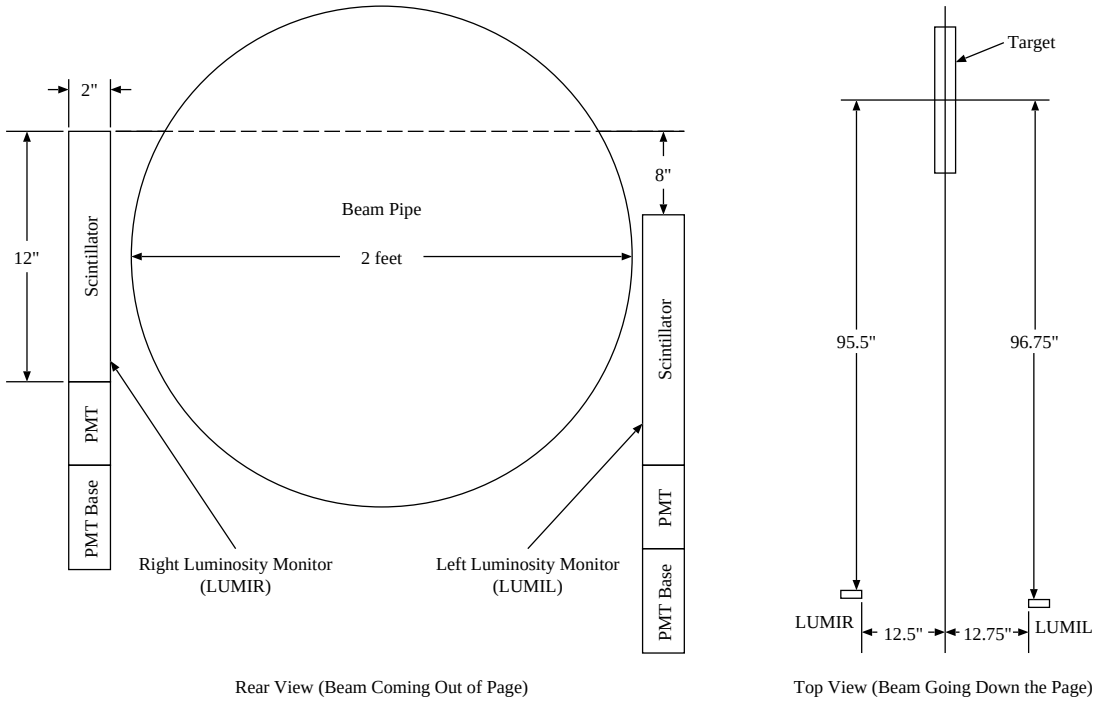

Figure 2.6: A schematic of the luminosity monitors.

Luminosity Monitors

Downstream of the SAMPLE target are a pair of detectors that measure the luminosity (the product of the beam charge and the target density) at forward scattering angles. After normalization to the beam charge, the luminosity monitor (LUMI) signals are sensitive to fluctuations in the density of the target. Since the LUMIs are at very forward angles the parity violating asymmetry (which is proportional to Q^2) should be zero (Section 1.2.3). Any asymmetry measured by these monitors has to be a false asymmetry due to helicity correlated beam parameter differences (Section 3.2) or a Mott asymmetry due to transverse beam polarization (Section 3.4.3). Figure 2.6 shows the composition and placement

of the luminosity monitors; they consist of long, thin strips of lucite coupled to PMTs. Čerenkov photons are generated in the lucite and detected by the PMTs.

2.3 Møller Polarimeter

Prior to entering the North Hall the electron beam passes through a region containing a polarimeter for determining the electron polarization. The polarimeter is used to measure the spin-dependent cross section asymmetry A_M for elastic scattering of polarized electrons from polarized electrons ($\vec{e}$-$\vec{e}$). The cross section asymmetry for elastic $\vec{e}$-$\vec{e}$, or Møller, scattering can be calculated exactly in quantum electrodynamics (QED). The expression for the asymmetry at a scattering angle of 90° in the center-of-mass (CM) frame is [Møl32, KR57]

$$A_M = -\frac{1}{9}\left[7P_Z^B P_Z^T - P_Y^B P_Y^T + P_X^B P_X^T\right] \tag{2.5}$$

where P_i^B and P_i^T are the polarization components of the beam and the target. The beam polarization is determined by having the electron beam strike a polarized target and measuring A_M at 90° CM.

A schematic of the Møller apparatus can be found in Figure 2.7. The target of polarized electrons is provided by the atomic electrons in a Supermendur* foil. The foil is exposed to magnetic fields generated by two sets of Helmholtz coils,

*Supermendur is an alloy of elements in the following proportions by mass [Arr92]: 49% Fe, 49% Co, and 2% Va.

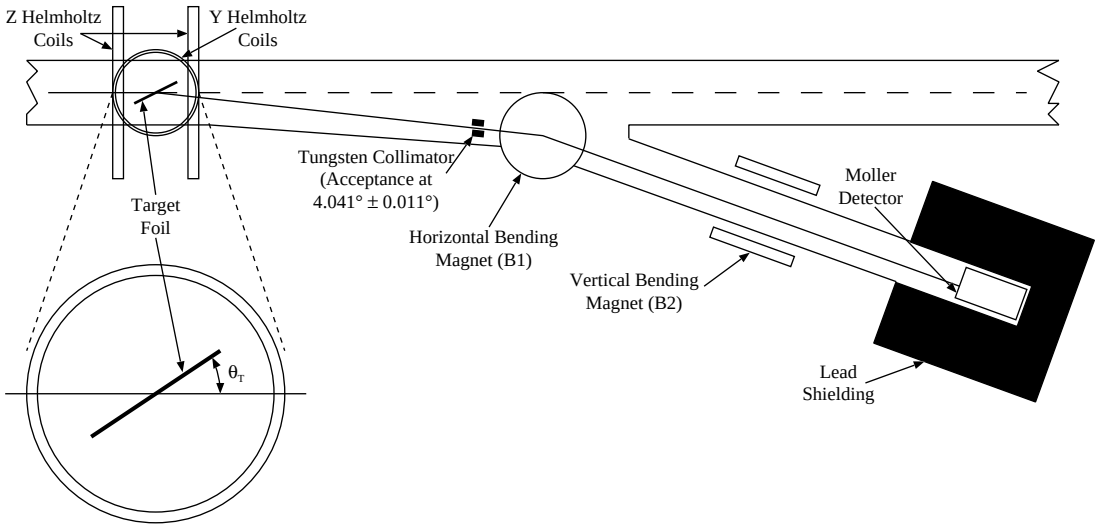

Figure 2.7: A schematic of the Møller polarimeter.

one set generates a field along the z axis* (z coils) and the other along the y axis (y coils). Outer shell electrons in the foil are polarized to $8.03\% \pm 0.12\%$ in the plane of the foil by the magnetic field [Arr92]. The target foil is mounted in a remotely controlled ladder that can be used to move the foil out of the beamline and rotate it about the vertical axis. Electrons that scatter at 90° CM (4.041° in the lab frame) pass through a tungsten collimator and enter a magnetic channel. The magnetic channel deflects the electrons away from the beamline and down to the detector. The horizontal deflection of 15.5° is accomplished by a dipole magnet, B1, and the vertical deflection of 34.8° by another dipole magnet, B2. The magnetic fields in the bending magnets can be varied in order to select

*The z axis lies along the electron beam trajectory, the x axis points in the direction that the dipoles bend the beam, and the y axis points perpendicularly out of the bend plane.

electrons with different scattering energies. Scattered electrons are detected with a lucite Čerenkov detector; the signal is integrated over the length of a beam pulse.

2.3.1 Longitudinal Beam Polarization Measurement

A measurement of the longitudinal beam polarization can be performed to high precision in a short period of time (approximately one hour) with the Møller polarimeter. The z coils are energized to their full strength of 100 gauss. The foil polarization is saturated by rotating the foil so it points along z, then it is rotated to an angle $\theta_T = 30.0^\circ$ with respect to the z-axis. The electron beam is turned on and a Møller data taking run begins. Yield and asymmetry measurements are taken for several different scattering energies. Electrons from true Møller scattering are peaked around 100 MeV in scattering energy while electrons from background processes have a continuous distribution. By taking yield measurements at several energies the background-to-signal ratio can be measured as well as the asymmetry at the Møller peak. After the Møller run is finished the target foil is resaturated and rotated to $\theta_T = -30.0^\circ$. The measurements at $\pm\theta_T$ can be combined to improve the measurement of the longitudinal polarization and to check for residual transverse polarization (Section 3.3.1).

2.3.2 Wien Filter and Accelerator Solenoid Calibration

As discussed in Section 2.2.1, the bending dipoles used to steer the electron beam into the North Hall also cause the electron spin to precess about the y-axis by $\theta_g = 16.6°$. The Wien filter and accelerator solenoids have to be set to account for the $g-2$ precession so that the beam is purely longitudinal at the SAMPLE target. The fact that the Møller polarimeter is located after the final bending magnet means that it can be used to calibrate the Wien filter and accelerator solenoids. A series of "spin transport" measurements were performed prior to SAMPLE data taking.

The components of the beam polarization at the SAMPLE or Møller target, can be written in the following way:

$$P_X^B = P^B \left[\cos\theta_g \sin\theta_W \langle\cos\phi\rangle + \sin\theta_g \cos\theta_W\right] \tag{2.6}$$

$$P_Y^B = P^B \left[\sin\theta_W \langle\sin\phi\rangle\right] \tag{2.7}$$

$$P_Z^B = P^B \left[\cos\theta_g \cos\theta_W - \sin\theta_g \sin\theta_W \langle\cos\phi\rangle\right] \tag{2.8}$$

where θ_W is the Wien rotation and ϕ is the precession in the solenoids. The target polarization components can be written

$$P_X^T = P^T \sin\theta_T \tag{2.9}$$

$$P_Y^T = 0 \tag{2.10}$$

$$P_Z^T = P^T \cos\theta_T \tag{2.11}$$

assuming that only the z coils are energized and that there is no target foil tilt about the x-axis. Using equations 2.5 and 2.6-2.11, the Møller asymmetry can be written as

$$A_M = -\frac{P^T P^B}{9}[(7\cos\theta_T \sin\theta_g - \sin\theta_T \cos\theta_g)\sin\theta_W \langle\cos\phi\rangle + (7\cos\theta_T \cos\theta_g + \sin\theta_T \sin\theta_g)\cos\theta_W]. \tag{2.12}$$

The first term in this is equation is sensitive to the rotation caused by the solenoids and the Wien filter while the second term is sensitive only to the Wien filter.

The first term in equation 2.12 goes to zero when the target angle is set to $\theta_T = \arctan(7\tan\theta_g) = 64.4°$, the "magic" angle; the Wien filter is calibrated at this setting. The rotation caused by the Wien filter is parameterized as

$$\theta_W = \kappa V \tag{2.13}$$

where V is the potential between the electrostatic plates in the filter and κ is a measured quantity. The coefficient κ is determined by varying V and measuring the resultant Møller asymmetry. Figure 2.8(a) is a plot of such data and the resulting fit to a cosine, $\kappa = 17.10 \pm 0.27$. The point $V = \frac{16.6°}{\kappa}$ is the desired Wien filter setting to exactly counteract the $g-2$ rotation.

Once the Wien filter has been calibrated the second term in equation 2.12 is set to zero by choosing V such that $\theta_W = 90.0°$, making the asymmetry sensitive to the precession caused by the accelerator solenoids ϕ. The asymmetry is maximized by choosing $\theta_T = -25.6°$, the "anti-magic" angle. As in the Wien filter

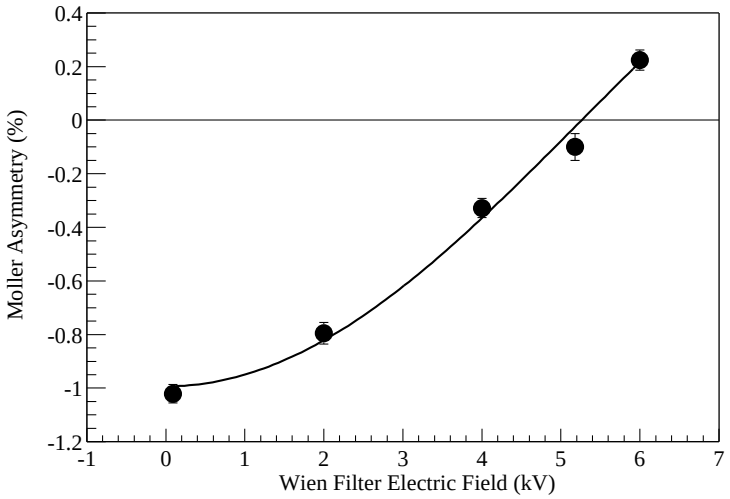

(a) Wien Filter Calibration

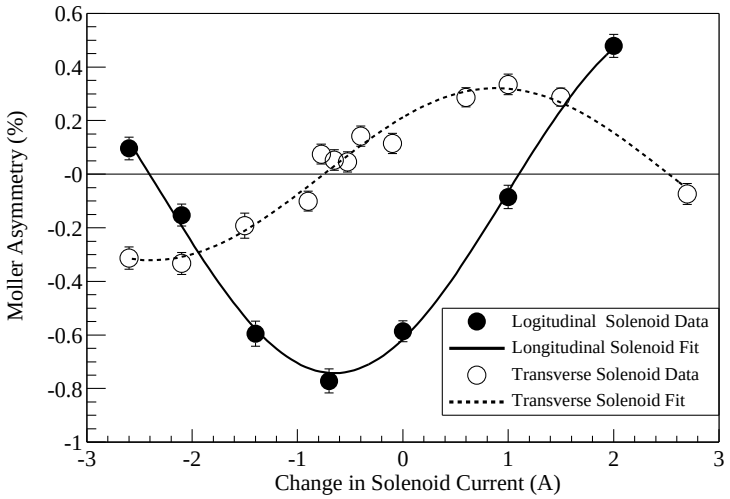

(b) Solenoid Calibration

Figure 2.8: Plots of the Wien filter and solenoid calibration data. The desired solenoid current setting corresponds to the point where the longitudinal data has a minimum and the transverse data goes through zero.

calibration, the solenoid precession is parameterized as

$$\phi = \phi_0 + \lambda \Delta I \tag{2.14}$$

where ΔI is the change in solenoid current from the nominal settings and ϕ_0 and λ are measured constants. The Møller asymmetry as a function of ΔI is shown in Figure 2.8(b) for longitudinal and transverse scans. In a transverse scan the foil is polarized along y and the polarimeter is sensitive to transverse polarization. The zero crossing in the transverse scan should correspond to the minimum in the longitudinal scan and yield the desired solenoid setting for minimal ϕ rotation. The Wien filter is set to the $\theta_W = -16.6°$ point, the solenoid currents are set to the $\phi = 0$ point, and neither are adjusted for the remainder of the experiment.

2.4 Target

A schematic of the SAMPLE target can be found in Figure 2.9(a). The target cell is a 40 cm long aluminum cylinder containing liquid hydrogen, positioned coaxially with the electron beam [Bei96]. It is joined to the bottom of a stainless steel loop that contains a 10-60 Hz circulating pump and an internal heater on one side and a heat exchanger on the other as shown in Figure 2.9(b). Under normal operating conditions the target loop is full of liquid hydrogen at a temperature of 20 Kelvin (K) and under 2 atmospheres (atm) of pressure. The total volume of liquid hydrogen in the system is approximately 25 liters (L).

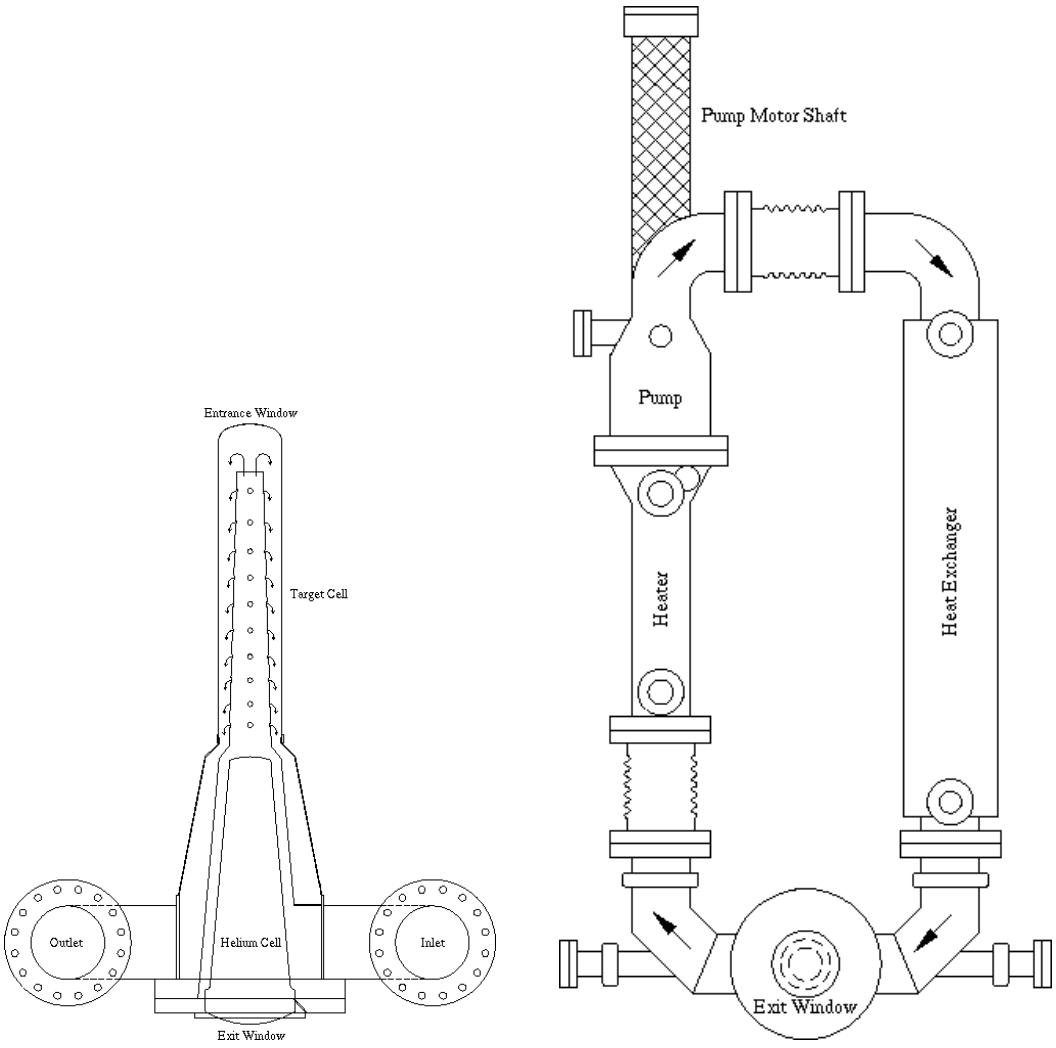

(a) Target (Top View)

(b) Target Loop (Rear View)

Figure 2.9: Schematics of the SAMPLE target and recirculating loop.

The cryogenic fluid has to be able to absorb approximately 500 Watts (W) of heat deposited by the electron beam without boiling. A helium gas refrigerator supplies 12 K helium gas at 16 pounds per square inch absolute (psia) to the counterflow heat exchanger in the target loop through vacuum-jacketed transfer lines. This coolant gas provides the necessary cooling power to keep the hydrogen in a liquid state. An open ended aluminum cone with holes punched in it runs along the interior of the target cell and efficiently removes packets of liquid hydrogen from the electron beam path. This design keeps the liquid hydrogen moving through the target cell and loop in order to prevent localized density fluctuations due to the passage of the electron beam.

A resistive heater, consisting of Chromel ribbon wound about a pair of fiberglass boards, is mounted inside the target loop beneath the circulating pump. This heater is operated in a feedback loop with the measured beam current in order to keep the power deposition in the target constant over time. When the electron beam is on the heater is set to low power deposition, but when the electron beam goes off the heater power increases by approximately 500 W to compensate for the loss of beam heating. This keeps the target density constant as the electron beam is turned on and off. The feedback loop is controlled by a PC using target control software written in National Instruments' LabView environment. This software also monitors the overall state of the target system including the refrigerator and the gas panel used to fill the target.

The 15 mil entrance window of the target cell has a certain radius of curvature. In order to keep the path length in hydrogen traversed by the electron beam a constant as a function of transverse beam displacement the 4 mil hydrogen exit window must have the same radius of curvature. The curvature of this window is maintained by a small helium gas backing cell attached to the rear of the target. The exit window forms the wall between the He gas and the liquid hydrogen, and the helium gas is maintained at a slight positive pressure with respect to the liquid hydrogen.

The entire target assembly is suspended inside of an evacuated aluminum chamber. The target cell protrudes into a cylindrical scattering chamber that is an eighth inch thick; the scattering chamber is encased in 2.5 mm of lead shielding. The loop and backing cell are contained in a large rectangular vacuum box behind the scattering chamber.

2.5 Detector

The SAMPLE detector is a large, air Čerenkov detector set at backward scattering angles with respect to the target as shown in Figures 2.10 and 2.11. The first figure shows a cut-away side view of the detector with one mirror and Čerenkov PMT combination depicted. The second figure is a rendering of the full SAMPLE geometry. Most electrons that scatter into the detector are moving faster than the speed of light in air. As a result, a shock wave of photons is generated similar

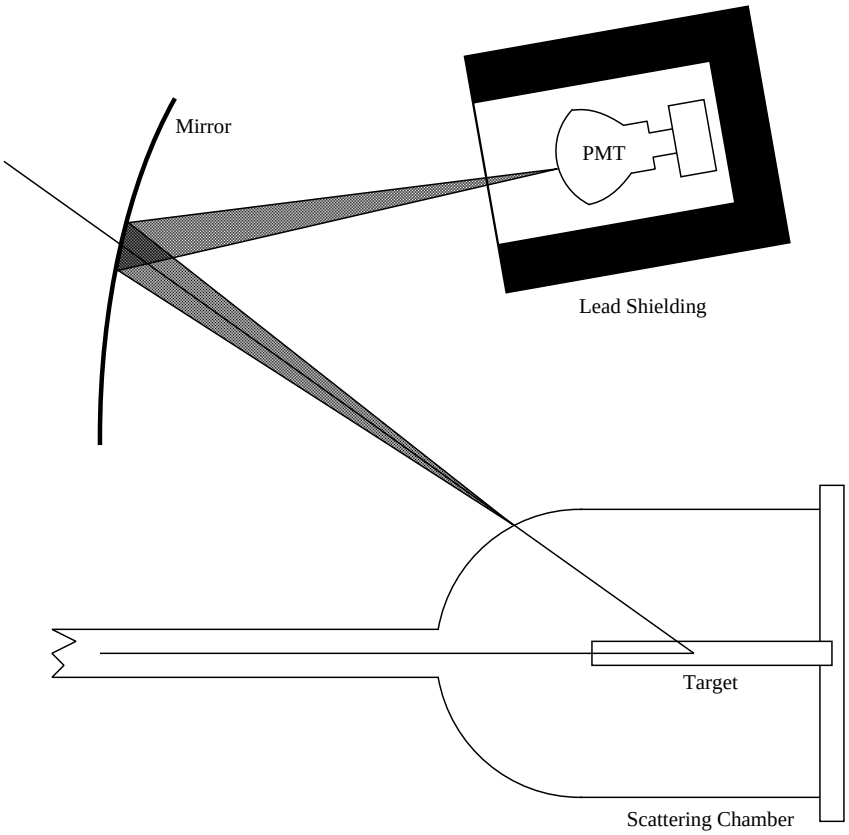

Figure 2.10: A side view of the SAMPLE detector and target systems; only one mirror and photomultiplier tube combination are depicted for clarity. A single scattered electron and Čerenkov cone are shown.

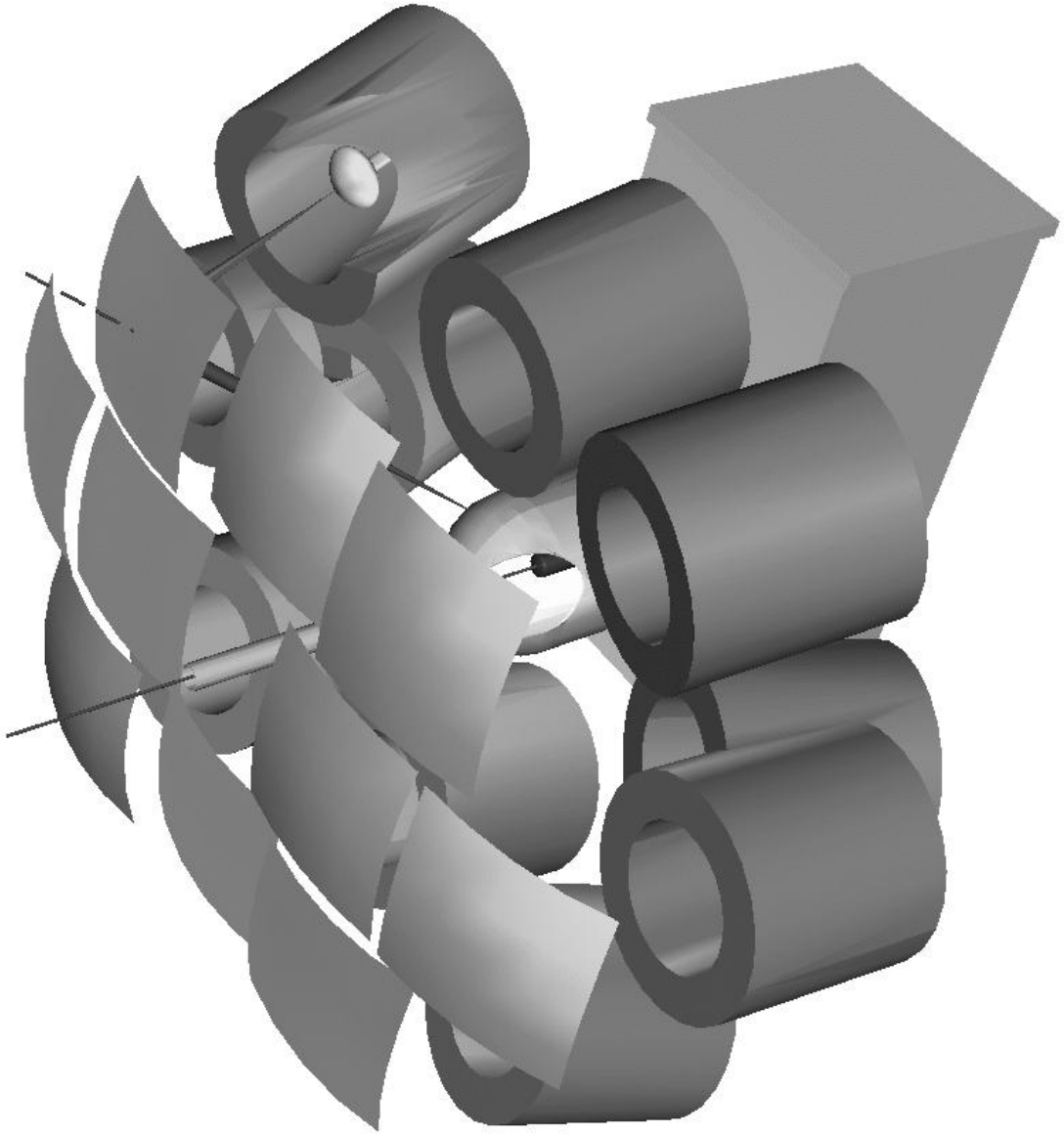

Figure 2.11: A rendering of the SAMPLE detector and target systems. Portions of the scattering chamber and lead shielding have been cut away for clarity. A single scattered electron and Čerenkov cone are shown.

to the sonic shock wave associated with an aircraft moving faster than the speed of sound [Leo94]. These photons, known as Čerenkov photons, are emitted at an angle θ_C with respect to the electron's momentum and form a cone about the electron trajectory:

$$\cos\theta_C = \frac{1}{\beta n(\omega)} \tag{2.15}$$

where $n(\omega)$ is the index of refraction of the radiating medium as a function of photon frequency. The number of photons emitted per unit length of radiator traveled is given by the following equation [Leo94, Gro00]:

$$\frac{dN}{dx} = 2\pi Z^2 \alpha \sin^2\theta_C \int_{\lambda_1}^{\lambda_2} \frac{d\lambda}{\lambda^2} \tag{2.16}$$

where Z is the charge of the particle Ze, α is the fine structure constant, and λ_1 and λ_2 are the limits of the wavelength range over which photons are detected. As Figure 2.12 indicates, electrons with an energy less than about 20 MeV do not emit Čerenkov photons and are not detected.

The detector subtends approximately 1.5 steradians (sr) of solid angle at scattering angles greater than 110° and consists of an array of 10 ellipsoidal mirrors that focus the Čerenkov photons from back-scattered electrons onto a corresponding array of ten 8" PMTs. Each mirror is formed from a sheet of glass 62.6 cm on a side and molded to fit a form that defines the ellipsoidal shape of the mirror. The PMTs are encased in large cylinders of lead that act as shields to electromagnetic background radiation. The lead cylinders have openings to

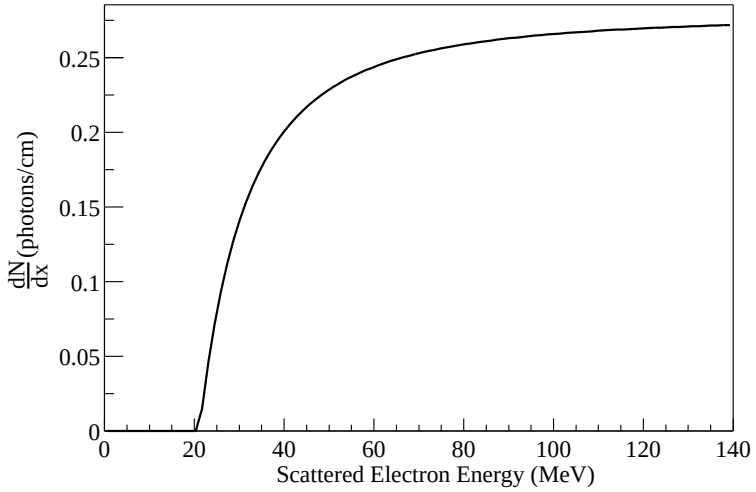

Figure 2.12: A graph of the number of Čerenkov photons emitted per unit length as a function of scattered electron energy.

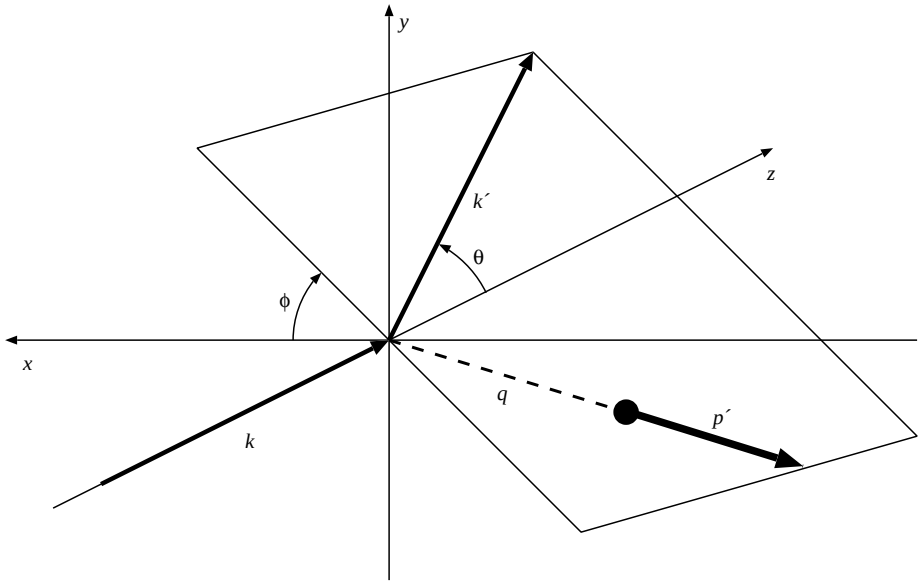

Figure 2.13: This figure defines the coordinate system in which the polar and azimuthal scattering angles are defined at the SAMPLE target. The z axis lies along the electron beam momentum vector, the x axis points in the direction the electron beam is bent to get into the North Hall (beam left), and the y axis is orthogonal to both.

Mirror	θ (°)	ϕ (°)	L (cm)	L_C (cm)	Q^2 ((GeV/c)^2)	$\Delta\Omega$ (sr)	σ (nb)
1	145.9	135.8	171.6	128.8	0.100	0.133	4.52
2	154.0	90.0	151.7	104.6	0.103	0.170	5.09
3	145.9	44.2	171.6	128.8	0.100	0.133	4.52
4	138.4	180.0	182.1	144.3	0.097	0.118	4.66
5	160.5	180.0	153.0	103.2	0.104	0.167	4.64
6	160.5	0.0	153.0	103.2	0.104	0.167	4.64
7	138.4	0.0	182.1	144.3	0.097	0.118	4.66
8	145.9	224.2	171.6	128.8	0.100	0.133	4.52
9	154.0	270.0	151.7	104.6	0.103	0.170	5.09
10	145.9	315.8	171.6	128.8	0.100	0.133	4.52

Table 2.2: A table of physical parameters of the mirrors. The θ and ϕ are central polar and azimuthal angles with respect to the target. L is the distance from the center of the target to the center of the mirror. The quantity L_C is the length of Čerenkov radiator (air) a charged particle must pass through to reach the mirror from the target. The momentum transfer squared Q^2 is calculated at the central angle. The total solid angle subtended by a mirror is given by $\Delta\Omega$. The total cross section for elastic scattering into the region subtended by a mirror is given by σ.

allow the reflected Čerenkov photons to reach the PMTs. Remotely controlled mechanical shutters of thin aluminum can seal off the entrances of each lead cylinder thereby preventing light from striking the PMTs. These shutters are used for background studies (see Section 3.3.2). The entire detector assembly, mirrors, PMTs, and target, is housed in a light-tight aluminum box. Table 2.2 lists the physical quantities of interest for the ten mirrors and Figure 2.13 shows the coordinate system in which the polar and azimuthal scattering angles θ and ϕ are defined. As Table 2.2 and Figure 2.11 indicate, the symmetry of the detector means that the ten mirrors are grouped into four types, each at a different value of Q^2.

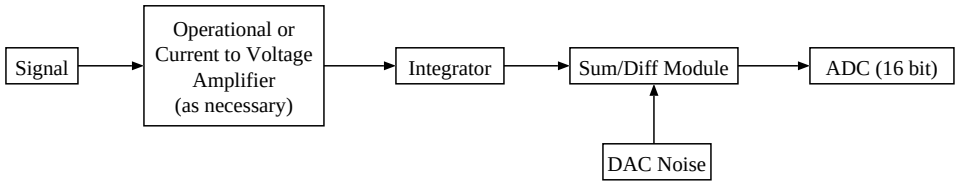

Figure 2.14: A schematic of one channel of the integrating electronics used in normal data taking mode.

2.6 Data Acquisition

Approximately 3600 electrons are scattered into the acceptance of a given mirror in one beam pulse. The scattered electron rate is too high to count them individually, therefore an integrating data acquisition system is used. The data acquisition system is very closely related to the one employed by a previous parity violation experiment at Bates [Kum90, Mic88].

One channel of the integration electrons is shown in Figure 2.14 (there are 40 channels in all). The important signals from the experiment, Čerenkov PMTs, halo and luminosity monitors, BPMs, and charge toroids, are integrated for a period of 50 μs that includes the beam pulse. The integrators only accept positive voltage levels therefore certain signals are passed through (non)inverting op amps or current to voltage amplifiers before being integrated. A random DC voltage (0 to 0.5 V), known as the "DAC noise", is added to each of the integrated signals in "sum/diff" modules before being digitized in 16 bit ADCs with an input range of 0 to 5 V. A new DAC noise value is generated for each beam pulse and a 16 bit word corresponding to the value of the DAC noise is written into the SAMPLE

data stream so that the appropriate voltage can be subtracted in software during data analysis. Special "DAC fit" runs measure the ADC value for each detector over the full range of DAC noise values so that the DAC noise subtraction can be performed. DAC fit runs are carried out every day or two, always after a beam polarization measurement and occasionally at other times.

The purpose of the DAC noise system is to spread the signal over a wider range of the ADC than it would normally occupy. The ADCs used in this experiment are known to suffer from differential nonlinearity, as can be seen in Figure 2.15(b). If the signals in a given pulse pair straddle a discontinuity, then a large false asymmetry could result. The size of this false asymmetry δA is found to be proportional to the size of the discontinuity S and the measured asymmetry A [Mic88]:

$$\delta A = \psi \frac{SA}{\sigma} \tag{2.17}$$

where σ is the width of the signal distribution and $\psi \approx 0.7$. The signal width is typically about 300 ADC channels in the absence of DAC noise and S has been measured to be as large as 50 channels leading to $\frac{\delta A}{A} = 12\%$. The DAC noise spreads the signal over approximately 6000 channels (0.5 V) of the ADC thereby reducing $\frac{\delta A}{A}$ to less than 1%.

The signal-handling and digitization are instrumented with CAMAC electronics. A microVAX III (μVAX) running VMS and the Q data acquisition system is used to read out the CAMAC electronics and record the data on a pulse-by-pulse

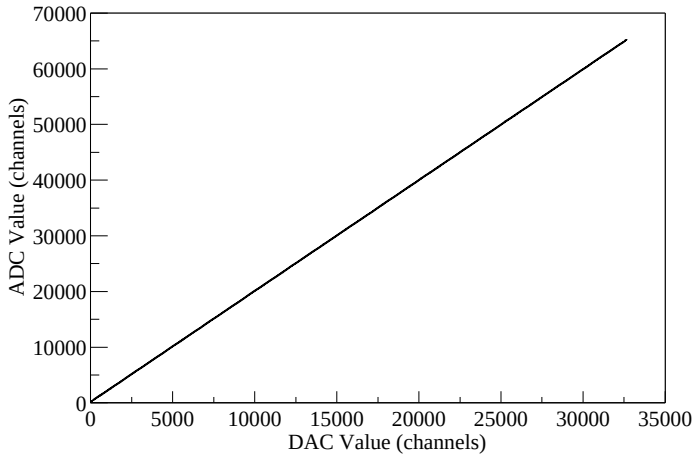

(a) ADC Linearity Data

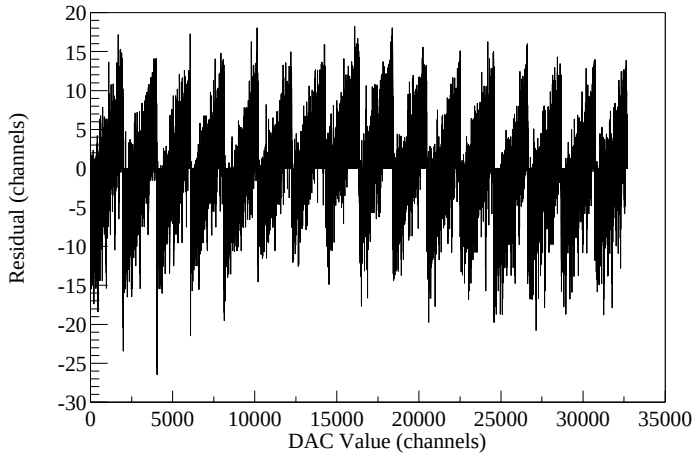

(b) Residuals from Fit

Figure 2.15: The first plot shows the linearity of a typical ADC used in this experiment. The second plot reveals the differential nonlinearity that shows up when the deviation of the data from a linear fit are plotted. The signal from a typical mirror is centered around channel 25000 and has a width of order 300 channels.

basis [Gro86]. A microprogrammable branch driver (MBD) handles the interface between the CAMAC electronics and the μVAX. The data acquisition system operates at 600 Hz without significant dead time. Every 1.6 milliseconds (1/600 s) 40 analog signals are digitized and an "event" consisting of 75 16-bit words is recorded onto a hard drive. These events contain, in addition to the 40 ADC signals, the pulse's helicity, timeslot, DAC noise value, event type (pedestal or data), NEW/COMP status, and other pertinent information. The hard drives are swappable, so when one is full it is exchanged for an empty one. The data-bearing drive is placed in a VAXStation 9000 connected to three Exabyte 8 mm tape drives in order to make four identical copies of the data for distribution to the collaboration. After the data has been written to tape it is transferred over the lab's internal Ethernet network to a dual processor PC running Linux for immediate analysis. There is also an online data analysis, but in the 1998 data taking period only about one out of every three events was analyzed this way.

A timing diagram of the electronics is shown in Figure 2.16. All the signals in the data acquisition are set relative to MOD pulse, which indicates the start of a new beam pulse. The timeslot trigger increments the scaler that tags each beam pulse with its timeslot number; every 1/60 s the 60 Hz Clear signal resets the timeslot scaler. If the pulse is a pedestal pulse (a pulse with no electrons) then the Pedestal LAM signal will form an AND with the timeslot trigger. Approximately 3 μs after the timeslot trigger signal arrives the integrate gate is opened for 50

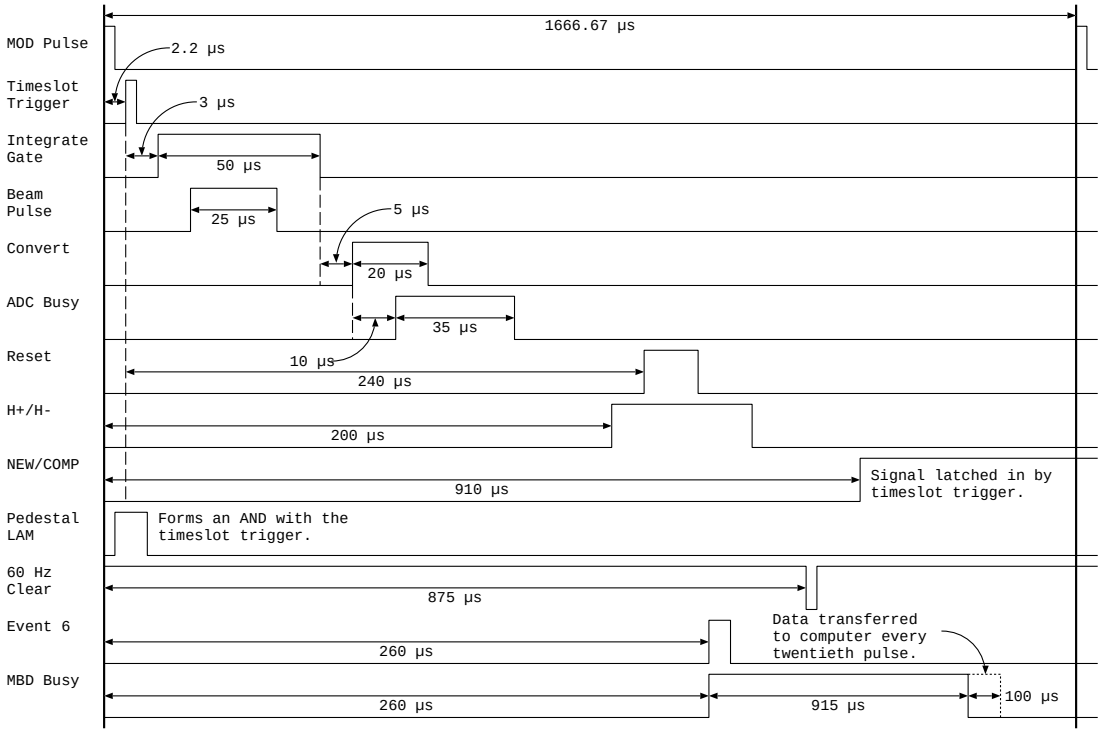

Figure 2.16: Timing diagram of the electronics signals in the experiment.

μs. The beam pulse arrives shortly after the gate opens and lasts for 25 μs. After the integrate gate closes the ADC digitizes the analog signal (Convert and ADC Busy). Well after the ADCs have finished digitizing a pair of TTL signals (H+ and H$-$) from the polarized source carry the information about the electron helicity into the data acquisition; H+($-$) is true for positive (negative) helicity electrons and false otherwise. The complementary helicity signals and late arrival times are intended to eliminate false asymmetries due to electronic crosstalk. The ADC reset signal (Reset) arrives at approximately the same time as the helicity signals. The signal (NEW/COMP) that records whether the beam pulse is in the new or complement sequence arrives before MOD pulse and is latched in

by the timeslot trigger. After all the signals have been digitized and the helicity information has arrived from the polarized source the data are stored in the MBD (MBD Busy); the data are shipped to the computer after every twentieth pulse.

2.7 Supplemental Measurements

There are a variety of additional measurements that have to be performed in order to extract the physics asymmetry A_p from A_Y. The integrating nature of the detector makes it impossible to separate the signal due to elastically scattered electrons from the signal due to background events during a normal data run; the extraction of the signal-to-background ratio is discussed in the next section, 2.7.1. The measured asymmetry can be contaminated by a parity-conserving asymmetry due to Mott scattering of transversely polarized electrons. Great care is taken to insure that the electron beam is longitudinally polarized to a high degree, but it is still important to assess the possible contribution to the asymmetry due to non-zero transverse polarization. Section 2.7.2 describes the measurements performed to address this issue.

2.7.1 Signal Analysis

The signal measured by the PMTs in the main detector contains contributions from processes other than elastically scattered electrons: low energy EM radiation from "beam scraping" in the accelerator, pion production in the target, and

scintillation in the detector volume. These background processes can affect the measurement in two ways: by diluting the elastic signal and by exhibiting a non-zero asymmetry. Several measurements are performed to assess both the dilution factor and the asymmetry of background processes.

As will be discussed in Section 3.1, the fraction of the detector yield due to elastically scattered electrons is broken down into three multiplicative factors: the light fraction f_l, the elastic fraction f_e, and the pion fraction f_π. If the measured yield consists of a part due to elastically scattered electrons (S) and a part due to background (B), then the following equation holds:

$$\frac{S}{S+B} = f_l f_e (1 - f_\pi). \tag{2.18}$$

Light Fraction

The light fraction is the portion of the total signal due to photons of some kind striking the PMT. It is measured by closing the mechanical shutters over the PMTs (Section 2.5) and performing a normal data run. The shutter closed yield Y_C was previously determined to be predominantly due to low energy EM radiation [Mue97b]. Such radiation should not exhibit a helicity dependent asymmetry and we verify that is the case by making one out of every four data runs a closed shutter run. Enough statistics are collected in the closed shutter runs to extract a relatively high precision measurement of the closed shutter asymmetry. Results and analysis of these data are discussed in Section 3.3.2.

Pulse Counting

It is not enough to measure just the light fraction when trying to determine the signal-to-background for the experiment. The light signal, $Y_O - Y_C$, can contain contributions from scintillation photons as well as the signal from Čerenkov photons. In order to extract the fraction of the light signal due to elastically scattered electrons, f_e, it is necessary to perform a conventional counting measurement. By placing a scintillating paddle behind a mirror and forming a coincidence between it and the corresponding PMT it is possible to determine the elastic fraction. This set of measurements is referred to as pulse counting.

As mentioned previously the rates in the experiment are too high to perform a counting measurement, but it is possible to reduce the beam current and the rate to a level where a counting measurement becomes feasible. The polarized source and accelerator are operated in a special mode known as "tracer bullets" mode. The shutter Pockels cell in the polarized source is set to allow beam in only one of the ten possible timeslots and the linear polarizer downstream of the SPC is rotated so that there is some leakage current in the other nine time slots. The current in the unshuttered, or tracer bullets, time slot is high enough that data can be collected from the integration electronics. A dedicated data acquisition system, shown in Figure 2.17, is used to collect pulse counting data in the nine time slots with leakage current. In this way, the integration mode electronics can verify that the beam quality is consistent with normal, integration mode running.

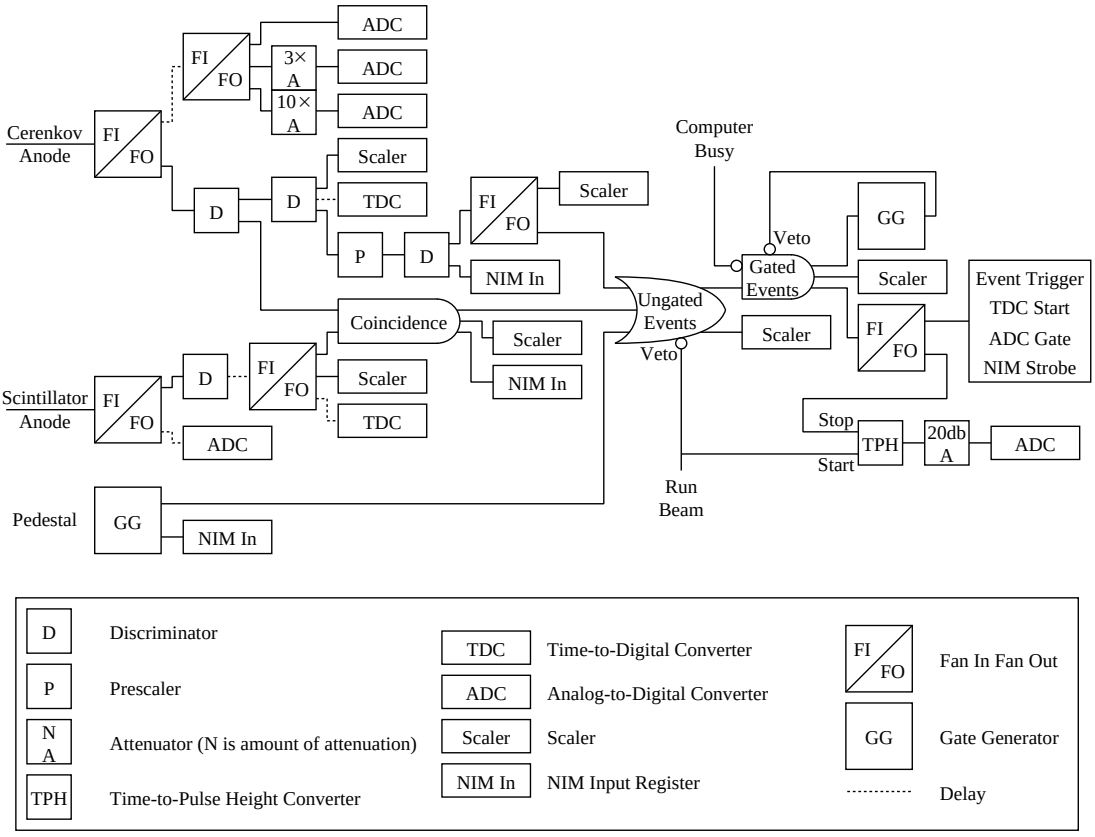

Figure 2.17: A schematic of the pulse counting electronics. There are only enough electronics to instrument one full channel so data is taken from one scintillator and mirror combination at a time.

This is important since the elastic fraction could vary between pulse counting runs and integration runs if the background changed. Detailed descriptions of the pulse counting electronics can be found in Ref. [Mue97b, For98]. The only difference in the pulse counting data acquisition between this measurement and the data taken in 1995 and 1996 was the absence of the electronics associated with the NaI detector, which was not used for this measurement.

Scintillating paddles are placed behind five of the mirrors as shown in Figure

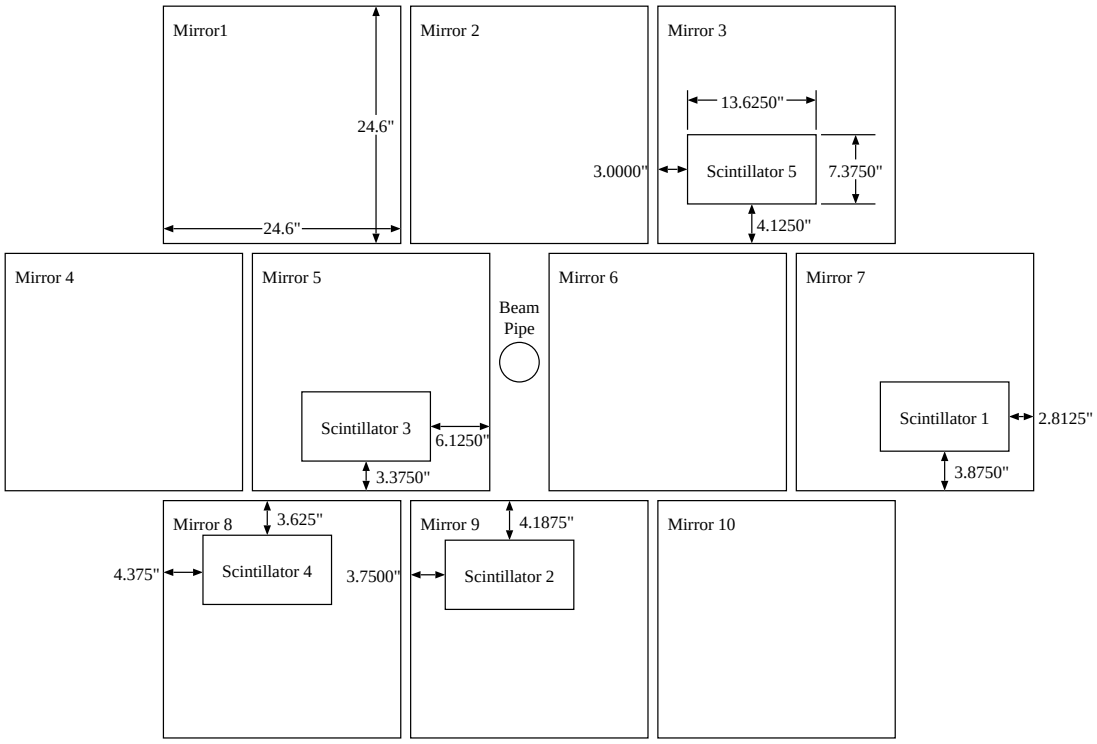

Figure 2.18: A view of the mirrors as seen from the target. The location behind the mirrors of the scintillating paddles used in pulse counting is shown. This diagram also reveals the symmetry of the detector that results in four groups of mirrors, each with a different value of Q^2 (see Section 2.5).

2.18. The paddles are $13\frac{5}{8}'' \times 7\frac{3}{8}'' \times \frac{1}{4}''$ in size and are coupled to $2''$ photomultiplier tubes. A sixth paddle, $4'' \times 6''$ in area, can be placed at various points behind the mirrors to take data on the "mirror edge effect" (Section 3.3.3). Coincidences between the paddles and the PMTs are recorded, as are singles spectra in each. The coincidences are due to elastically scattered electrons and are the true signal in the experiment. The singles in the PMTs are due to elastically scattered electrons and background processes. The data analysis to extract the elastic fraction is discussed in Section 3.3.3. The pion fraction f_π is also extracted from

the pulse counting data in Section 3.4.2.

2.7.2 Transverse Beam Polarization

A possible source of false asymmetry in the SAMPLE experiment is transverse beam polarization. Only longitudinally polarized electrons contribute to the parity violating asymmetry, but transversely polarized electrons can contribute to a parity conserving Mott asymmetry. This is a left-right asymmetry (an asymmetry in the number of electrons scattered to the left and to the right), unlike the parity violating asymmetry, but it could contribute if the detector were not symmetric about whatever axis the transverse electron polarization lay along. The correction K_T to the parity violating asymmetry would be

$$K_T = A_T \frac{P_B^T}{P_B} F_S \tag{2.19}$$

where A_T is the measured asymmetry for purely transverse beam polarization, P_B^T and P_B are the transverse and total beam polarizations, and F_S is the degree of detector asymmetry.

A series of measurements with transversely polarized beam were performed to extract A_T. The Wien filter and accelerator solenoids were used to make the beam transverse, first in the bend plane and then orthogonal to it. A day's worth of asymmetry running was taken with the polarization in each state. The results of these measurements are discussed in Section 3.3.1.

Chapter 3

Data Analysis

3.1 Overview

The design of the SAMPLE detector system simplifies the data analysis in a number of ways; there is no particle tracking or rejection and the data acquisition system has no dead time. Computer dead time is an issue, but it has been addressed by limiting the amount of data collected per beam pulse. The data consists primarily of the signals from ten photomultiplier tubes, integrated over a period of 50 μs at a rate of 600 Hz for a couple of months. The disadvantages of the detector system are that it has no energy resolution, no way of directly separating signal from background, and the small measured asymmetry requires continuous monitoring of all aspects of the experiment to avoid contamination by false asymmetries. The data analysis is designed to address these issues.

This chapter begins by addressing some of the computational aspects of the

data analysis (Section 3.1.1). This is followed by an in-depth discussion of the analysis procedure, how to get from the measured asymmetry in the ten PMTs to A_p (Section 3.1.2). The rest of the chapter discusses each portion of the analysis in detail.

3.1.1 Computational Aspects

As discussed in Section 2.6, the data in this experiment consists of the signals from 40 ADCs as well as various binary flags and scalars. One set of readings constitutes an event, of which there are 600 per second. An hour's worth of events are stored together as a run and are eventually written onto 8 mm magnetic tape for permanent storage.

The structure of the data analysis at this point is very similar to the analysis of a spectrometer-based experiment. One set of programs, generally known as the replay engine, takes the raw data from the tape and extracts useful physics quantities. In a spectrometer experiment this would generally take the form of a database, or ntuple, indexed by particle and event number. It would be possible at this point to do some processing and throw away events that were not desired because they came from the wrong reaction or had some other undesirable quantity. The good events could be saved away and, theoretically, make it unnecessary to run the replay engine again. The integrating nature of the SAMPLE detector makes it impossible to sort events by particle or reaction type, therefore it is not

possible to winnow down the data to only good events. Furthermore, as will be discussed in Section 3.2, a great deal of the final analysis occurs in the replay engine. As a result, the entire SAMPLE data set was replayed a number of times by the replay engine before a final result was extracted.

The replay engine consists of approximately 17000 lines of C/C++ code. It contains calls to the ROOT library of physics analysis functions, written by a team at CERN, which are used to generate ntuples and histograms [BR96]. The replay engine is known to run on DEC Alpha workstations running Digital UNIX (this analysis) and on Pentium-based systems running Linux. The primary output of the replay engine is a large set of text files consisting of a couple thousand lines of text each, one line for each run. The data contained in a single line is outlined in Table 3.1. The yield is the average over all analyzed events of whatever quantity is stored in the file. The asymmetry is the difference in yields over the sum for the two helicity states in a pulse pair averaged over all pairs in the run; the difference is stored instead of the asymmetry if the sum of yields could be zero, as in the measurement of the beam position for instance. A straight average was performed on the yields and asymmetries/differences:

$$\langle Q \rangle = \frac{1}{N} \sum_{i=1}^{N} Q_i \tag{3.1}$$

where Q is the quantity being averaged over and N is the total number of mea-

Column Number	Contents
1	Run Number
2	Helicity Plate State (1=OUT, -1=IN)
3	Total Number of Analyzed Events
4	Yield
5	Error on the Yield
6	Total Number of Analyzed Pulse Pairs
7	Asymmetry or Difference
8	Error on the Asymmetry or Difference

Table 3.1: A table listing the contents of each column in the text files generated by the replay engine. For a discussion of slow helicity reversal (Helicity Plate State) see Section 2.2.1.

surements in the run. The error on Q is given by [BR92]

$$\sigma_Q = \sqrt{\frac{1}{N}(\langle Q^2 \rangle - \langle Q \rangle^2)}. \tag{3.2}$$

The data from every physics quantity or beam monitor in the experiment is stored in one of these files. They are generally referred to as ADC files or "dot out" files in reference to their file extension (.out). After the data have been replayed the bulk of the analysis focuses on processing the dot out files generated by the engine. A variety of ROOT-based and Perl scripts are used to generate graphs, histograms, and summary tables of the data in the files.

3.1.2 Procedure

The basic analysis procedure was to extract the asymmetry for each mirror in each run, then perform a weighted average over all runs and all mirrors to get the

final physics asymmetry A_p. This philosophy is codified in the following equation:

$$A_p = \frac{\sum_{m=1}^{10} \sum_{n}^{\text{all runs}} \frac{A_p(m,n)}{\sigma_p^2(m,n)}}{\sum_{m=1}^{10} \sum_{n}^{\text{all runs}} \frac{1}{\sigma_p^2(m,n)}} \tag{3.3}$$

where $A_p(m,n)$ is the physics asymmetry for run n and mirror m and $\sigma_p(m,n)$ is the error on the determination of A_p*. Once A_p has been calculated for the entire experiment equation 1.65 is used to extract G_M^s.

Before equation 3.3 could be employed it was necessary to determine A_p for each mirror and run. In the replay engine a raw asymmetry $A^U(m,n)$ for each mirror is calculated; histograms of the raw asymmetry A_O^U from all open shutter runs in the experiment, divided by the beam polarization P_B, are shown for each mirror in Figure 3.1. The data are well described by a Gaussian probability distribution [BR92]

$$P_G(x;\mu,\Sigma) = \frac{I_h}{\Sigma\sqrt{2\pi}} \exp\left[-\frac{1}{2}\left(\frac{x-\mu}{\Sigma}\right)^2\right] \tag{3.4}$$

where I_h is the integral of the histogram and μ and Σ are the mean and width† of the distribution. The mean and width are given by the weighted mean and

*For the sake of clarity, the dependence on mirror m and run n will be dropped from $A_p(m,n)$ and related quantities except where it would cause confusion with quantities averaged over all m and n.

†This unconventional notation for the distribution width Σ is chosen so as to avoid confusion with the error σ.

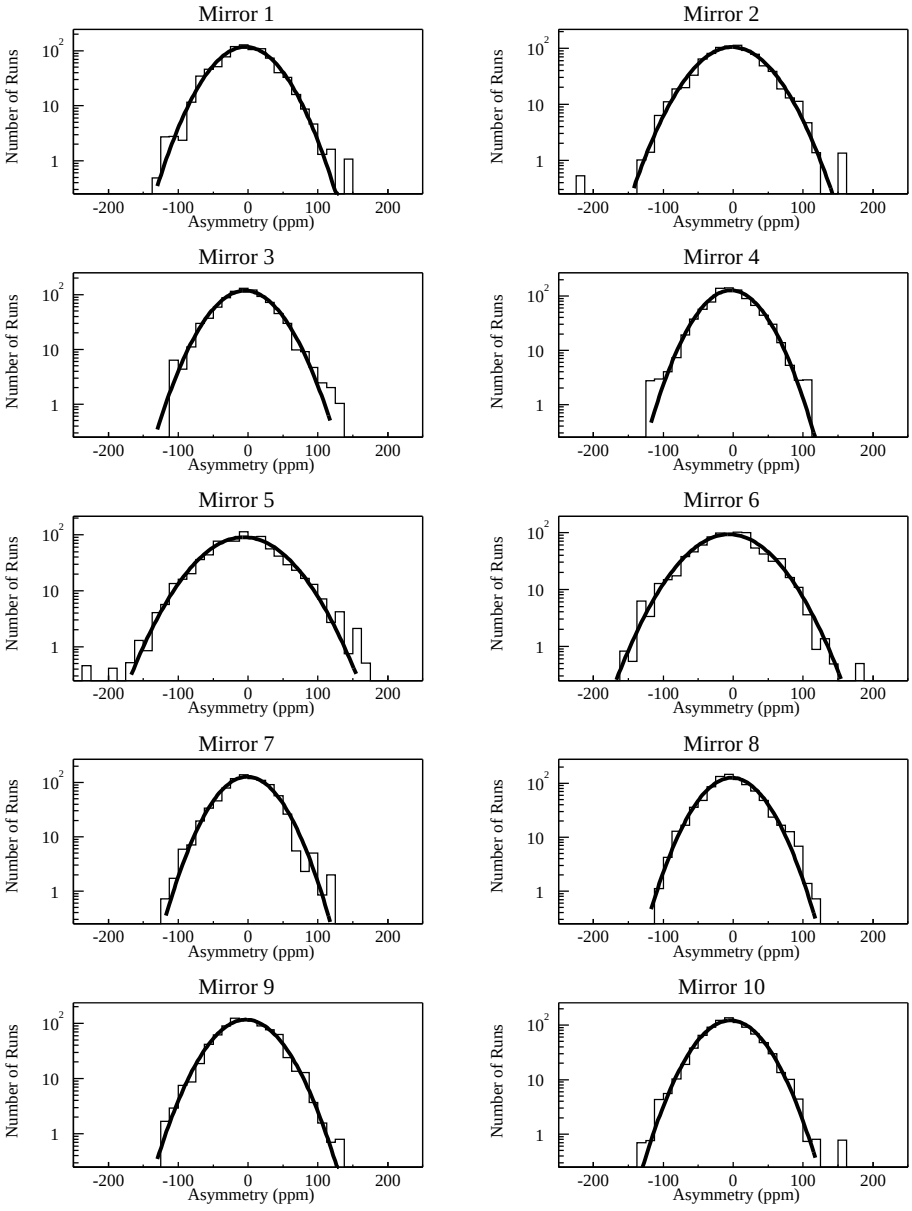

Figure 3.1: Raw asymmetries for each mirror for all open shutter runs (a minus sign has been applied to the helicity out data to account for helicity reversal). The beam polarization has been divided out of each asymmetry and the value weighted by the statistical error on each average measurement. The histograms have been renormalized so that the integral I_h is equal to the number of runs $N = 871$. The curves are the Gaussian probability distributions for the mean asymmetries and errors tabulated in Table 3.2 over a range of $\pm 3.5\Sigma$ (see equations 3.4 - 3.6).

error on the asymmetry:

$$\mu(m) = \frac{\sum_n \frac{A(m,n)}{\sigma_a^2(m,n)}}{\sum_n \frac{1}{\sigma_A^2(m,n)}} \tag{3.5}$$

$$\Sigma(m) = \sqrt{N}\sigma_\mu(m) = \sqrt{\frac{N}{\sum_n \frac{1}{\sigma_A^2(m,n)}}} \tag{3.6}$$

where $A(m,n)$ is the asymmetry for mirror m and run n, σ_A is the error on $A(m,n)$, and N is the total number of runs. The black line on the histogram is the Gaussian probability distribution with μ and Σ determined by equations 3.5 and 3.6. The $\mu(m)$ and $\sigma_\mu(m)$ are tabulated in Table 3.2 (the column labelled A_O^U/P_B), along with the χ^2 and number of degrees of freedom ν for a Gaussian distribution of mean μ and width Σ. The value of χ^2 is determined as follows [BR92]:

$$\chi^2 = \sum_{j=1}^{n_b} \frac{[h(x_j) - P_G(x_j)]^2}{P_G(x_j)} \tag{3.7}$$

where $h(x_j)$ is the contents of bin x_j and n_b is the number of bins. The number of degrees of freedom ν is equal to $n_b - 3$. The probability P that a random set of data points drawn from this parent distribution will result in a χ^2 greater than that in the table is also shown.

The raw asymmetry A_O^U is not the asymmetry due to elastic $\vec{e}$-p scattering because it is contaminated by false asymmetries and background processes. The transformation of A_O^U into A_p was a three step process. First, false asymmetries due to helicity correlated beam parameter differences (Section 3.2) were removed. Then, dilution factors were applied to correct for background, imperfect electron

Mirror	$\frac{A_O^U}{P_B}$ (ppm)	χ^2	ν	P
1	-3.71 ± 1.25	24.2	19	0.1887
2	-1.52 ± 1.40	15.6	21	0.7912
3	-4.19 ± 1.25	23.3	18	0.1786
4	-3.34 ± 1.16	35.0	17	0.0063
5	-6.08 ± 1.62	41.6	24	0.0145
6	-6.06 ± 1.59	30.1	24	0.1799
7	-1.29 ± 1.15	35.3	17	0.0057
8	-1.97 ± 1.17	28.1	17	0.0440
9	-3.09 ± 1.26	17.4	19	0.5644
10	-3.97 ± 1.21	12.2	18	0.8371

Table 3.2: This table lists the raw asymmetry, divided by the beam polarization, for each mirror averaged over all open shutter runs (see Figure 3.1). A minus sign has been applied to the helicity plate out data to account for the reversal of helicities. The value of χ^2 was calculated for a Gaussian probability distribution over a range of $\pm 3.5\Sigma$ from the mean value of the asymmetry (see equation 3.6). There are 871 data points (open shutter runs) in each average.

polarization, and radiative effects (Section 3.3). Finally, the measured asymmetries were corrected for background, closed shutter asymmetries (Section 3.4)*. The first step resulted in a corrected open (closed) shutter asymmetry A_O^C (A_C^C) that was an input to the other two steps.

The physics asymmetry $A_p(m,n)$ is related in a straightforward manner to $A_O^C(m,n)$. The corrected open shutter yield $Y_O^{C\pm}$ receives contributions from four sources:

$$Y_O^{C\pm} = Y_e^{\pm} + Y_\pi^{\pm} + Y_B + Y_C^{C\pm} \tag{3.8}$$

where $Y_e^{\pm}$ is the yield due to Čerenkov light from electrons, $Y_\pi^{\pm}$ is Čerenkov light

*Corrections due to pion production asymmetries and transverse beam polarization were too small to be necessary.

from pion decay, Y_B is other light sources, and $Y_C^{C\pm}$ is the corrected shutters closed background yield. The superscript $\pm$ refers to the electron helicity; it is assumed that all contributions can have helicity dependence except for the background due to other light sources. The average yield is denoted by the same symbol but without the superscript $\pm$. The light, elastic, and pion fractions are defined in terms of the yield contributions as follows:

$$f_l \equiv \frac{Y_O^C - Y_C^C}{Y_O^C} \tag{3.9}$$

$$f_e \equiv \frac{Y_e + Y_\pi}{Y_O^C - Y_C^C} \tag{3.10}$$

$$f_\pi \equiv \frac{Y_\pi}{Y_e + Y_\pi}. \tag{3.11}$$

The combination $f_l f_e (1 - f_\pi)$ constitutes the signal(S)-to-background(B) ratio in this experiment* (Sections 3.3.2, 3.3.3, and 3.4.2).

The open shutter asymmetry is the difference in corrected open shutter yields over the sum:

$$\begin{aligned} A_O^C &\equiv \frac{Y_O^{C+} - Y_O^{C-}}{Y_O^{C+} + Y_O^{C-}} \\ &= \frac{\left(Y_e^+ + Y_\pi^+ + Y_B + Y_C^{C+}\right) - \left(Y_e^+ + Y_\pi^+ + Y_B + Y_C^{C+}\right)}{2Y_O^C} \\ &= A_p^M \frac{Y_e}{Y_O^C} + A_C^C \frac{Y_C^C}{Y_O^C} + A_\pi \frac{Y_\pi}{Y_O^C} \\ &= A_p^M f_l f_e (1 - f_\pi) + A_C^C (1 - f_l) + A_\pi f_l f_e f_\pi \end{aligned} \tag{3.12}$$

where A_p^M is the measured $\vec{e}$-p scattering asymmetry and A_π is the asymmetry in threshold pion production. One assumption that goes into the derivation

*The exact expression is $f_l f_e (1 - f_\pi) \equiv \frac{S}{S+B}$.

of A_p in equation 1.65 is that the electron polarization is 100%, however the beam polarization P_B is approximately $\frac{1}{3}$, therefore A_p^M must be inflated by P_B. This correction was done on a run by run basis (Section 3.3.1). A_p^M must also be corrected for the emission of bremsstrahlung radiation, another effect not considered in the derivation of A_p. The factor R_c is an electromagnetic radiative correction that accounts for the emission of real bremsstrahlung photons (Section 3.3.4). In order to extract A_p the measured asymmetry must be inflated by the beam polarization P_B and multiplied by the electromagnetic radiative correction R_c:

$$\begin{aligned} A_p(m,n) &\equiv \frac{R_c(m)}{P_B(n)} A_p^M(m,n) \\ &= \frac{R_c(m)}{P_B(n) f_l(m) f_e(m)(1-f_\pi)} A_O^C(m,n) - K_C(m,n) - K_\pi(m,n) \end{aligned} \tag{3.13}$$

where

$$K_C(m,n) = \frac{R_c(m)(1-f_l(m))}{P_B(n) f_l(m) f_e(m)(1-f_\pi)} A_C^C(m,n) \tag{3.14}$$

$$K_\pi(m,n) = \frac{R_c(m)}{P_B(n)} \frac{f_\pi}{1-f_\pi} A_\pi. \tag{3.15}$$

The factors K_C and K_π are corrections for closed shutter and pion asymmetries and are the subject of Sections 3.4.1 and 3.4.2. There is an additional additive factor K_T arising from residual transverse beam polarization at the SAMPLE target (Section 2.7.2). It will be shown in Section 3.4.3 that this contribution is negligibly small. The remainder of this chapter is structured to follow the logical progression from $A_O^U \rightarrow A_O^C \rightarrow A_p$.

3.2 Corrections to the Asymmetry

The corrections procedure is designed to remove specific kinds of false asymmetries, those due to helicity correlated beam parameter differences. The elements required for a beam parameter to generate a false asymmetry are a non-zero, helicity dependent beam parameter difference and a correlation between detector yield and that beam parameter. Figure 3.2 indicates that such correlations do exist and that they are essentially linear in nature. This figure shows the correlation between right luminosity monitor yield and each of six different beam parameters with non-zero, helicity correlated beam parameter differences: X and Y position of the beam at the target, angular deviation in X and Y at the target (θ_X and θ_Y), beam energy E^*, and beam current $I^\dagger$. The yields measured for a given value of the beam parameter are averaged together to form one point in the graphs with an error bar given by the error on the mean. Luminosity monitor yield is shown rather than a mirror yield because the correlations are more pronounced. It is obvious from these plots how a false asymmetry can arise. If a beam parameter P_k has an average value P_k^+ for positive helicity electrons and an average value $P_k^- \neq P_k^+$ for negative helicity electrons, then on average the measured yield will be different in the two states independent of any parity

*The beam energy is expressed in % deviation from the mean central value of 200 MeV.

†Oftentimes in this work the beam current is expressed as the total charge in nC in one beam pulse. To get the peak or average beam current simply divide by 25 or 580×25 μs respectively.

violation effects.

This set of six parameters (X, Y, θ_X, θ_Y, E, and I) was chosen because all members exhibited a non-zero, helicity correlated beam parameter difference (Δ) or asymmetry (A). Figure 3.3 shows the measured beam parameter differences averaged over all runs in the experiment. Each point in the graphs represents an average of all of the data from one setting of the helicity plate, in or out, therefore the abscissa is time elapsed in the experiment in units of helicity plate setting (approximately 24-48 hours per unit). The filled (empty) circles correspond to data with the helicity plate in (out). If the signal being plotted is truly dependent on the helicity of the incident electrons, then the sign of the difference should reverse as the helicity plate is inserted or removed; the figure shows that this is only true of the beam charge asymmetry A_I. Table 3.3 lists the average difference or asymmetry for each of the six parameters sorted by helicity plate state. The data are broken down into two distinct sets, "Piezo On" and "Piezo Off", corresponding to the state of the piezo-electric beam position feedback mechanism discussed in Section A.2. The piezo feedback system was not employed at the beginning of the experiment (runs 2164-2669), but was for the remainder (runs 2670-3819). It is clear from the table and the first six points of the ΔX and ΔY graphs of Figure 3.3 that the position differences were much larger when the feedback system was not used. With the exception of ΔX and A_I this table shows that the measured difference has the same sign and approximate magnitude in both

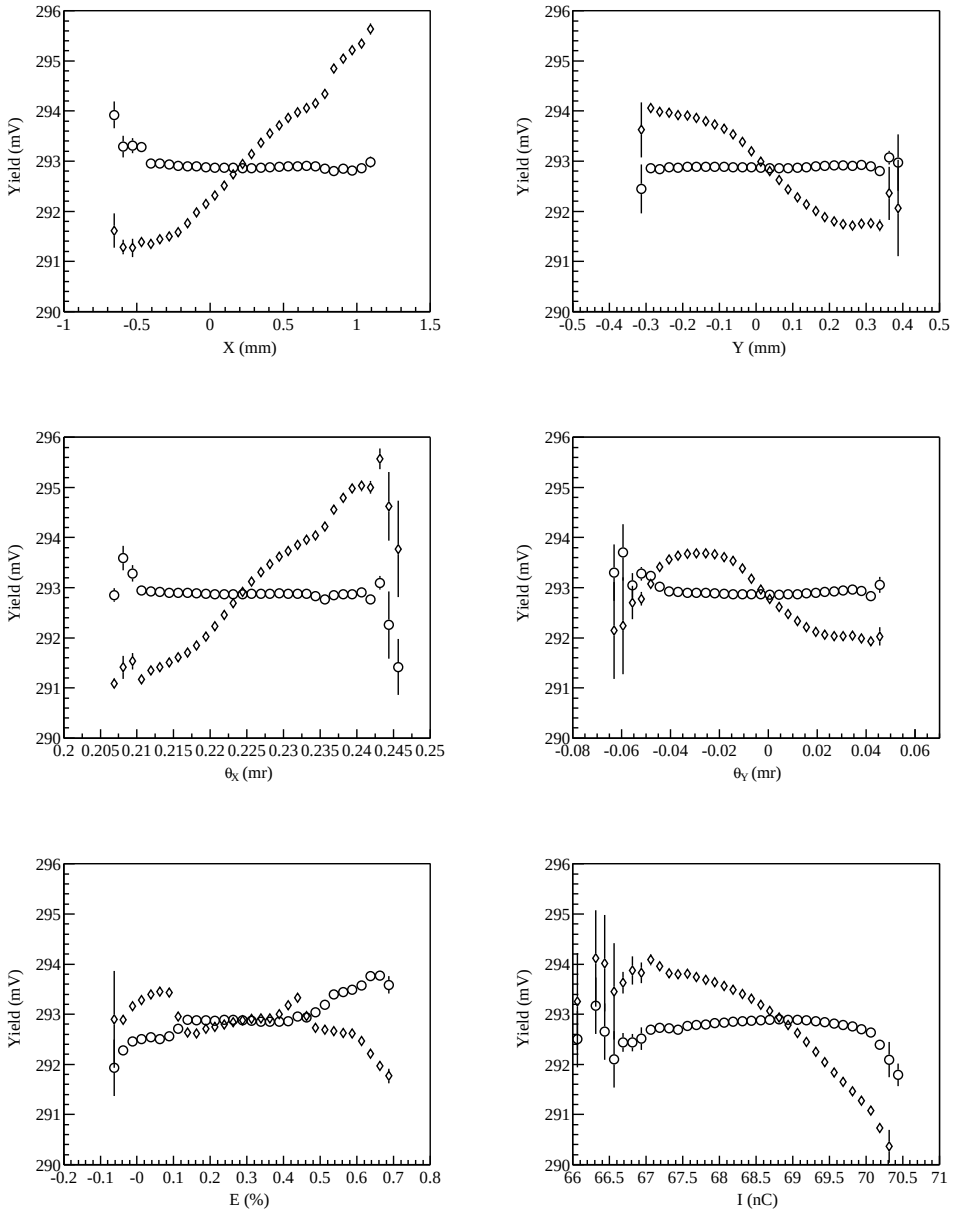

Figure 3.2: Representative right luminosity monitor yield slopes from one run (3362); one of the six beam parameters (X, Y, θ_X, θ_Y, E, and I) is plotted on the horizontal axis of each plot. All the data in a given bin along the horizontal axis are averaged together and plotted as one point with an error bar representing the statistical error on the mean. The diamonds (circles) are uncorrected (corrected) yield data. The results of linear fits to these data are presented in Table 3.4.

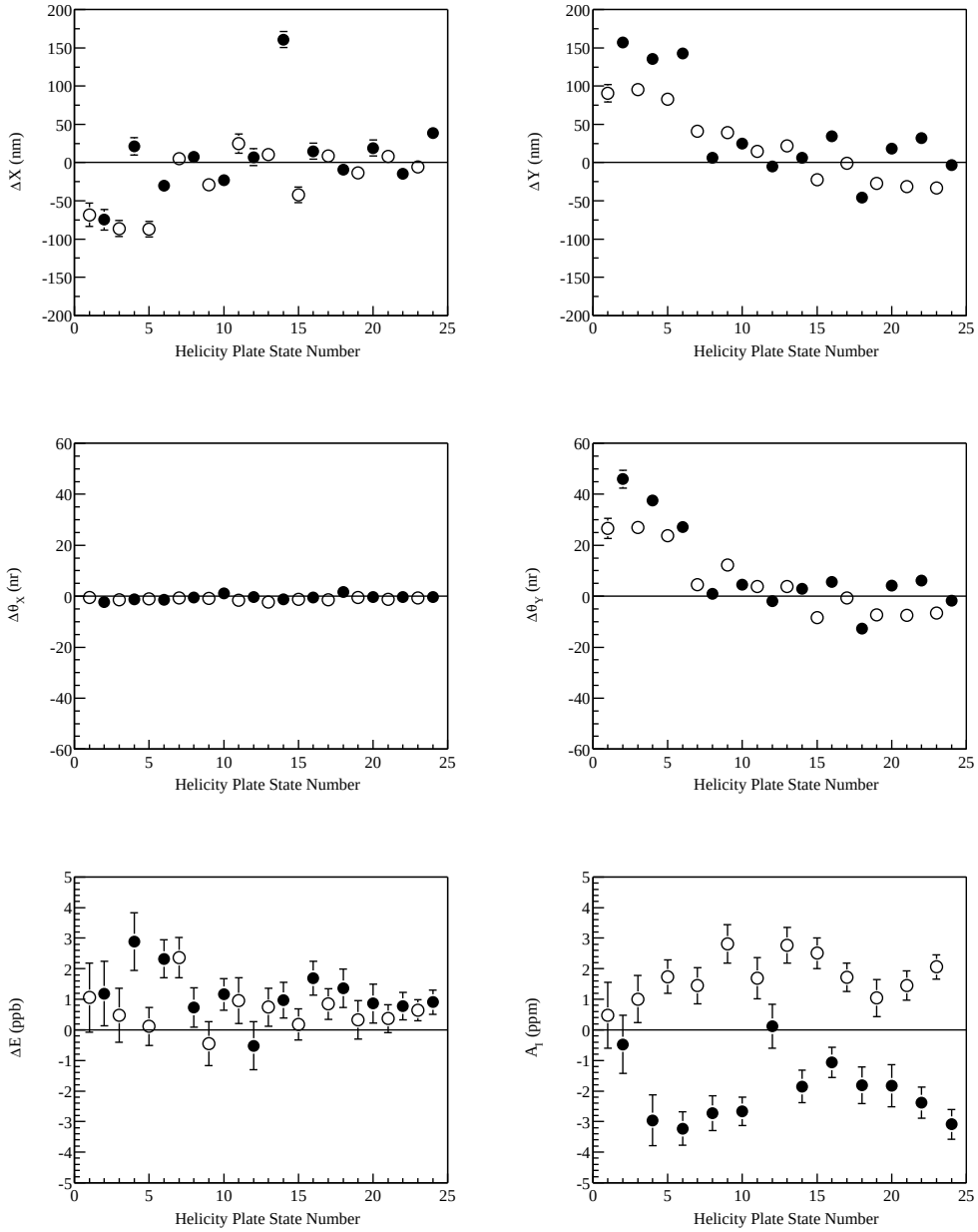

Figure 3.3: Asymmetry A or difference Δ in each beam parameter averaged over all runs in the experiment. Filled (empty) circles correspond to the helicity reversal plate being in (out). Each point along the x axis represents approximately 24-48 hours worth of data, all taken at one setting (in or out) of the helicity reversal plate.

Data Set	Helicity Plate Setting In	Out
	ΔX (nm)	
Piezo Off	-24.39 ± 6.33	-59.30 ± 5.54
Piezo On	18.72 ± 3.18	-3.50 ± 3.24
All Data	10.04 ± 2.84	-17.72 ± 2.80
	ΔY (nm)	
Piezo Off	145.37 ± 5.60	79.48 ± 4.09
Piezo On	8.60 ± 1.98	-12.44 ± 2.02
All Data	23.81 ± 1.87	5.57 ± 1.81
	$\Delta\theta_X$ (nr)	
Piezo Off	-1.51 ± 0.26	-1.11 ± 0.25
Piezo On	-0.09 ± 0.15	-1.14 ± 0.15
All Data	-0.45 ± 0.13	-1.13 ± 0.13
	$\Delta\theta_Y$ (nr)	
Piezo Off	33.76 ± 1.53	13.49 ± 1.03
Piezo On	1.62 ± 0.49	-3.50 ± 0.49
All Data	4.56 ± 0.46	-0.34 ± 0.44
	ΔE (ppb)	
Piezo Off	2.23 ± 0.46	1.04 ± 0.40
Piezo On	0.96 ± 0.18	0.51 ± 0.18
All Data	1.13 ± 0.17	0.60 ± 0.17
	A_I (ppm)	
Piezo Off	-2.66 ± 0.41	1.26 ± 0.36
Piezo On	-2.07 ± 0.18	2.00 ± 0.18
All Data	-2.17 ± 0.17	1.85 ± 0.16

Table 3.3: Table of beam parameter differences or asymmetries, sorted by helicity plate state, averaged over the entire experiment.

helicity plate states and that the differences are non-zero. The change in sign of the X difference can be traced to one point (number 14) with an abnormally large value. The beam charge asymmetry reverses systematically with helicity plate indicating a true dependence on electron helicity.

Assuming a linear relationship between measured yield Y and beam parameter P_k, $Y = \alpha P_k$, and a non-zero beam parameter difference, $\Delta P_k = P_k^+ - P_k^- \neq 0$ where superscript $+(-)$ indicates the positive (negative) helicity state, it is straightforward to show how a false asymmetry can arise. The measured yield in a given helicity state $Y^\pm$ consists of a portion due to parity violation $Y_{PV}^\pm$ and a portion due to the correlation with beam parameter:

$$Y^\pm = Y_{PV}^\pm + \alpha P_k^\pm. \tag{3.16}$$

An asymmetry is formed between two yield measurements in opposite helicity states

$$A_m = \frac{Y^+ - Y^-}{Y^+ - Y^-} \tag{3.17}$$

$$= \frac{Y_{PV}^+ + \alpha P_k^+ - (Y_{PV}^- + \alpha P_k^-)}{Y_{PV}^+ + \alpha P_k^+ + (Y_{PV}^- + \alpha P_k^-)} \tag{3.18}$$

$$\approx \frac{Y_{PV}^+ - Y_{PV}^-}{Y_{PV}^+ + Y_{PV}^-} + \frac{\alpha(P_k^+ - P_k^-)}{Y_{PV}^+ + Y_{PV}^-} \tag{3.19}$$

$$A_m \approx A_{PV} + \alpha \frac{\Delta P_k}{2\langle Y \rangle}. \tag{3.20}$$

where $\langle Y \rangle \equiv \frac{1}{2}(Y^+ + Y^-)$. The only assumptions in equation 3.20 are that $\alpha \frac{\Delta P_k}{2\langle Y \rangle} \ll 1$ and $A_k \equiv \frac{\Delta P_k}{2\langle P_k \rangle} \gg A_{PV}$, which are true in practice. The essence of the corrections procedure is to measure A, ΔP_k, and α, then solve for A_{PV}. It

should be noted that this procedure is the last step of a three-fold approach to ensuring that false asymmetries do not contaminate the measured asymmetry. The first two are to make the helicity correlated beam parameter differences and the detector yield-beam parameter correlations as small as possible.

3.2.1 Procedure

The corrections procedure was used to correct the measured yield on an event-by-event basis. This is equivalent to correcting the measured asymmetry, as was discussed in association with equation 3.20. The derivation of the procedure follows from equation 3.16, but must be expanded to deal with corrections from more than one beam parameter P_k:

$$Y = \langle Y \rangle + \sum_k C_k (P_k - \langle P_k \rangle) \tag{3.21}$$

$$\delta Y = \sum_k C_k \delta P_k \tag{3.22}$$

where P_k is a particular beam parameter, C_k is the correlation between Y and P_k, $\langle Q \rangle$ is the average of the quantity Q (where Q is Y or P_k) over the entire run, and $\delta Q \equiv Q - \langle Q \rangle$. The first step in performing the correction is to determine what the C_k are; multiple linear regression techniques are used to fit data to equation 3.22 and extract the C_k [BR92].

It is useful to recast the problem in dimensionless form before seeking solutions. This is done with the aid of covariances of Y and P_k which are defined as

[BR92]:

$$s_{jk}^2 = \frac{1}{N-1}\sum_{i=1}^{N}(\delta P_j(i)\delta P_k(i)) \tag{3.23}$$

$$s_{Yk}^2 = \frac{1}{N-1}\sum_{i=1}^{N}(\delta Y(i)\delta P_k(i)) \tag{3.24}$$

$$s_k^2 = \frac{1}{N-1}\sum_{i=1}^{N}(\delta P_k(i))^2 \tag{3.25}$$

$$s_Y^2 = \frac{1}{N-1}\sum_{i=1}^{N}(\delta Y(i))^2 \tag{3.26}$$

where the sum is over all events N in the run. The correlation coefficient r_{jk} is defined as a ratio of covariances:

$$r_{jk} \equiv \frac{s_{jk}^2}{s_j s_k}. \tag{3.27}$$

With these definitions it is possible to rewrite equation 3.22 in dimensionless form:

$$\begin{aligned}\frac{\delta Y}{s_Y} &= \sum_k \left(C_k \frac{s_k}{s_Y}\right)\left(\frac{\delta P_k}{s_k}\right) \\ &= \sum_k D_k \left(\frac{\delta P_k}{s_k}\right).\end{aligned} \tag{3.28}$$

Equation 3.28 must now be solved for D_k. The yield slopes C_k that are of ultimate interest are related to D_k by a ratio of covariances:

$$C_k = D_k \frac{s_Y}{s_k}. \tag{3.29}$$

The method of least squares is applied to equation 3.28 in order to find the best fit for D_k. This method generates a system of K equations, where K is

the total number of beam parameters, that must be solved for D_k [BR92]. This system of equations can be reduced to a single matrix equation:

$$\vec{\beta} = \overleftrightarrow{\alpha}\vec{D} \tag{3.30}$$

where

$$\begin{aligned}
\beta_k &\equiv \sum_{i=1}^{N} \frac{1}{\sigma_Y^2(i)} \frac{\delta Y(i)}{s_Y} \frac{\delta P_k(i)}{s_k} \\
&\approx \frac{N-1}{\sigma_Y^2} \frac{1}{s_Y s_k} \left(\frac{1}{N-1} \sum_{i=1}^{N} \delta Y(i) \delta P_k(i) \right) \\
&= \frac{N-1}{\sigma_Y^2} \frac{s_{Yk}^2}{s_Y s_k} \\
&= \frac{N-1}{\sigma_Y^2} r_{Yk}
\end{aligned} \tag{3.31}$$

and

$$\begin{aligned}
\alpha_{kl} &\equiv \sum_{i=1}^{N} \frac{1}{\sigma_Y^2(i)} \frac{\delta P_k(i)}{s_k} \frac{\delta P_l(i)}{s_l} \\
&\approx \frac{N-1}{\sigma_Y^2} r_{kl}.
\end{aligned} \tag{3.32}$$

The only assumption made in equations 3.31 and 3.32 is that the error on the individual measurements of Y, $\sigma_Y(i)$, are all the same and equal to σ_Y. Substitution of equations 3.31 and 3.32 into 3.30 results in*

$$r_{Yk} = r_{kl} D_l. \tag{3.33}$$

The r_{Yk} and r_{kl} are easy to calculate from the data during replay (see equations 3.23 – 3.27), then it is straightforward to invert the matrix equation 3.33 and

*Unless otherwise noted, a sum over repeated indices is assumed.

solve for D_k. After C_k has been extracted from D_k the run is replayed again and the individual yield measurements are corrected for beam parameter differences according to the following equation:

$$Y^C(i) = Y(i) - C_k \delta P_k(i) \tag{3.34}$$

where $Y^C(i)$ is the corrected yield. The corrected asymmetry A^C is formed from the corrected yield measurements $Y^C(i)$. This procedure can be easily altered so that different sets of beam parameters form the basis of the correction. The corrections procedure is applied to the data from each mirror therefore a corrected asymmetry $A^C(m)$ is extracted for each mirror. The luminosity monitor asymmetries are corrected as well based on their own yield slopes and serve as an important check on the success of the procedure.

3.2.2 Results

Figure 3.2 shows the corrected yield from one run (3362) for the right luminosity monitor as a function of each of the six beam parameters. A comparison with the uncorrected data in the same figure graphically illustrates the ability of this procedure to remove the beam parameter dependence of the measured yield. The results from linear fits to these data $\frac{\partial Y^{(U)C}}{\partial P}$ are presented in Table 3.4. For all six parameters the yield slopes are significantly reduced from decidedly non-zero to zero within a few standard deviations in most cases. This indicates that the corrections procedure is doing a good job of removing beam parameter

P_k	$\frac{\partial Y^U}{\partial P_k}$	$\frac{\partial Y^C}{\partial P_k}$
X (mV/mm)	3.0196(21)	$-0.0005(18)$
Y (mV/mm)	$-6.1152(51)$	0.0013(41)
θ_X (mV/mr)	155.82(15)	0.13(11)
θ_Y (mV/mr)	$-36.269(38)$	0.040(29)
E (mV/%)	0.544(15)	0.150(10)
I (mV/nC)	$-1.1196(15)$	0.0070(10)

Table 3.4: A table of uncorrected $\left(\frac{\partial Y^U}{\partial P_k}\right)$ and corrected $\left(\frac{\partial Y^C}{\partial P_k}\right)$ yield slopes for the right luminosity monitor. These results come from linear fits to the data in Figure 3.2 (run 3362). The uncorrected slopes presented here are different from the C_k used to correct the yield.

dependence from the measured yield. Though not shown here, the reduction in the mirror yield slopes is even more striking. These slopes are not the same as the C_k extracted from the replay engine, the C_k account for correlations between parameters as well. The average C_k for each of the ten mirrors and all six beam parameters are tabulated in Table B.1. Luminosity monitor slopes are listed in Table B.2.

The effect of the corrections procedure on the measured asymmetry is most clearly seen in the luminosity monitors. These monitors are mounted at forward scattering angles where the parity violating asymmetry goes to zero, $A_p \propto Q^2$ from equation 1.65. In the absence of false asymmetries these monitors should measure an asymmetry consistent with zero and the corrections procedure should remove any non-zero asymmetry.

In Figure 3.4(a) the measured luminosity asymmetry, averaged over both monitors and divided by P_B, is plotted for the two data sets discussed previously:

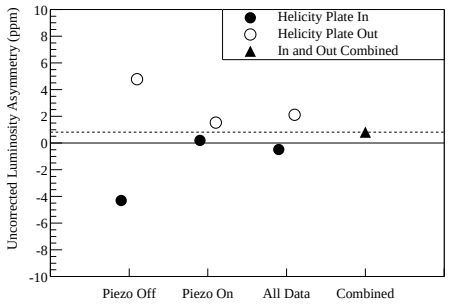

(a) Uncorrected Luminosity Monitor

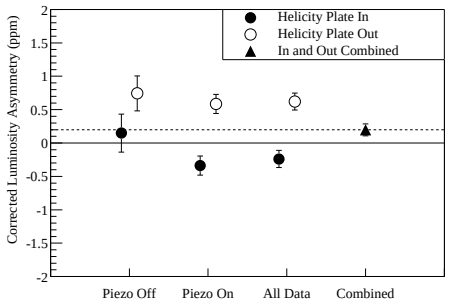

(b) Corrected Luminosity Monitor

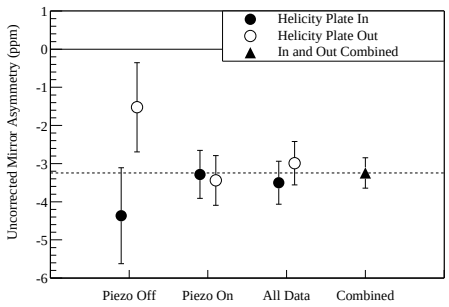

(c) Uncorrected Mirror

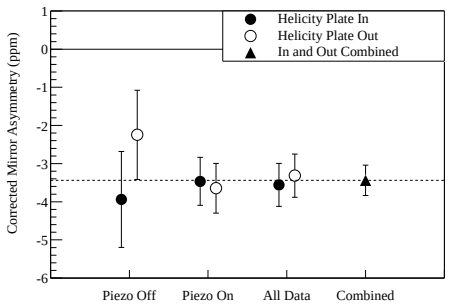

(d) Corrected Mirror

Figure 3.4: Asymmetries for the luminosity monitors and the mirrors sorted by data set and helicity plate state: piezo on/off/all and in/out. The dashed line corresponds to the asymmetry of the final, combined data point. The helicity plate out data have been multiplied by -1 to account for the reversal of helicities. Note the factor of five reduction in the vertical scale between Figures (a) and (b).

piezo on and off. During the time period before the piezo feedback system was used large position differences were measured in the North Hall (Table 3.3) and the measured luminosity asymmetry was very large and distinctly non-zero. The solid circles represent the asymmetry when the helicity plate was in and the empty circles represent the helicity plate out data*. Even after the piezo feedback system was in use, and the position differences were greatly reduced, the measured asymmetry in the luminosity monitors deviated from zero as indicated by the second pair of points in Figure 3.4(a). The third pair of points is the average over the entire experiment for each helicity plate state and the final point is the average of the two helicity plate data sets.

Figure 3.4(b) shows the same data points, but for the corrected asymmetry (note the factor of five reduction in vertical scale). The asymmetries in the piezo off data set have been reduced by an order of magnitude; the asymmetries in the piezo on data set have been reduced as well. The final corrected asymmetry is within two standard deviations of zero, down from eight standard deviations in the uncorrected case, thus the luminosity monitor asymmetry presents strong evidence that the corrections procedure works. Numerical values for the data shown in Figure 3.4 are found in Table 3.5.

Figures 3.4(c) and 3.4(d) show the average (un)corrected mirror asymmetry

*A minus sign has been applied to the helicity plate out data to account for the reversal of helicities.

Data Set	Uncorrected Asymmetry (ppm) In	Uncorrected Asymmetry (ppm) Out	Corrected Asymmetry (ppm) In	Corrected Asymmetry (ppm) Out
		Luminosity Monitors		
Piezo Off	-4.31 ± 0.36	-4.78 ± 0.33	0.15 ± 0.28	-0.74 ± 0.26
Piezo On	0.19 ± 0.15	-1.53 ± 0.16	-0.34 ± 0.14	-0.59 ± 0.14
All Data	-0.48 ± 0.14	-2.11 ± 0.14	-0.24 ± 0.13	-0.62 ± 0.13
Combined	0.81 ± 0.10		0.19 ± 0.09	
		Mirrors		
Piezo Off	-4.37 ± 1.26	1.52 ± 1.17	-3.94 ± 1.26	2.25 ± 1.17
Piezo On	-3.28 ± 0.63	3.44 ± 0.65	-3.46 ± 0.63	3.65 ± 0.65
All Data	-3.50 ± 0.56	2.99 ± 0.57	-3.56 ± 0.56	3.32 ± 0.57
Combined	-3.25 ± 0.40		-3.44 ± 0.40	

Table 3.5: A table of uncorrected and corrected luminosity monitor and mirror asymmetries. The luminosity monitor data has been averaged over open and closed shutter runs, but the mirror data has only been averaged over the open shutter runs. The beam polarization has been divided out in both cases. Unlike Figure 3.4, the helicity plate out data have not been multiplied by -1 to account for the reversal of helicities.

broken down in the same way as the luminosity monitors. In these plots the beam polarization has been divided out and a weighted average of all ten mirrors has been used*. The most striking feature of these figures is the minor impact the corrections have on the asymmetry, the change is well within the plotted statistical error bar. Close inspection of the piezo off data in both figures reveals that the helicity plate in and out points moved closer together to a non-zero value. This is again strong evidence that the corrections procedure properly removes false asymmetries due to helicity correlated beam parameter differences, but these figures also indicate that the mirrors are relatively insensitive to fluctuations

*This weighted average is not the one used to extract A_p in Chapter 4 because the dilution factors have not been applied to each mirror yet.

Mirror	$\frac{A_Q^C}{P_B}$ (ppm)	χ^2	ν	P
1	-3.88 ± 1.25	25.6	19	0.1425
2	-1.65 ± 1.40	19.9	21	0.5267
3	-4.34 ± 1.25	25.1	18	0.1234
4	-3.50 ± 1.16	27.6	17	0.0496
5	-6.30 ± 1.62	35.6	24	0.0601
6	-6.24 ± 1.59	29.9	24	0.1894
7	-1.38 ± 1.15	32.7	17	0.0124
8	-2.22 ± 1.17	27.5	17	0.0515
9	-3.34 ± 1.26	13.5	19	0.8139
10	-4.17 ± 1.21	16.6	18	0.5534

Table 3.6: This table lists the corrected asymmetry, divided by the beam polarization, for each mirror averaged over all open shutter runs (see Figure 3.5). A minus sign has been applied to the helicity plate out data to account for the reversal of helicities. The value of χ^2 was calculated for a Gaussian probability distribution over a range of $\pm 3.5\Sigma$ from the mean value of the asymmetry (see equation 3.6). There are 871 data points (open shutter runs) in each average.

in these parameters. The final mirror asymmetry is shifted by only 0.19 ppm, approximately half of the statistical error on the measurement (Table 3.5).

Once the corrections procedure has been applied, the individual mirror asymmetries can be extracted. Figure 3.5 shows the histogram of open shutter corrected asymmetries for each mirror individually, after the beam polarization has been divided out. As in the case of the uncorrected asymmetries (Figure 3.1) the distribution of asymmetries measured in each run obeys a Gaussian distribution with a mean given by the weighted mean of the asymmetries μ and the width Σ. The final corrected mirror asymmetries, divided by the beam polarization, are presented in Table 3.6.

The residual, non-zero luminosity monitor asymmetry of 0.19 ppm in Table

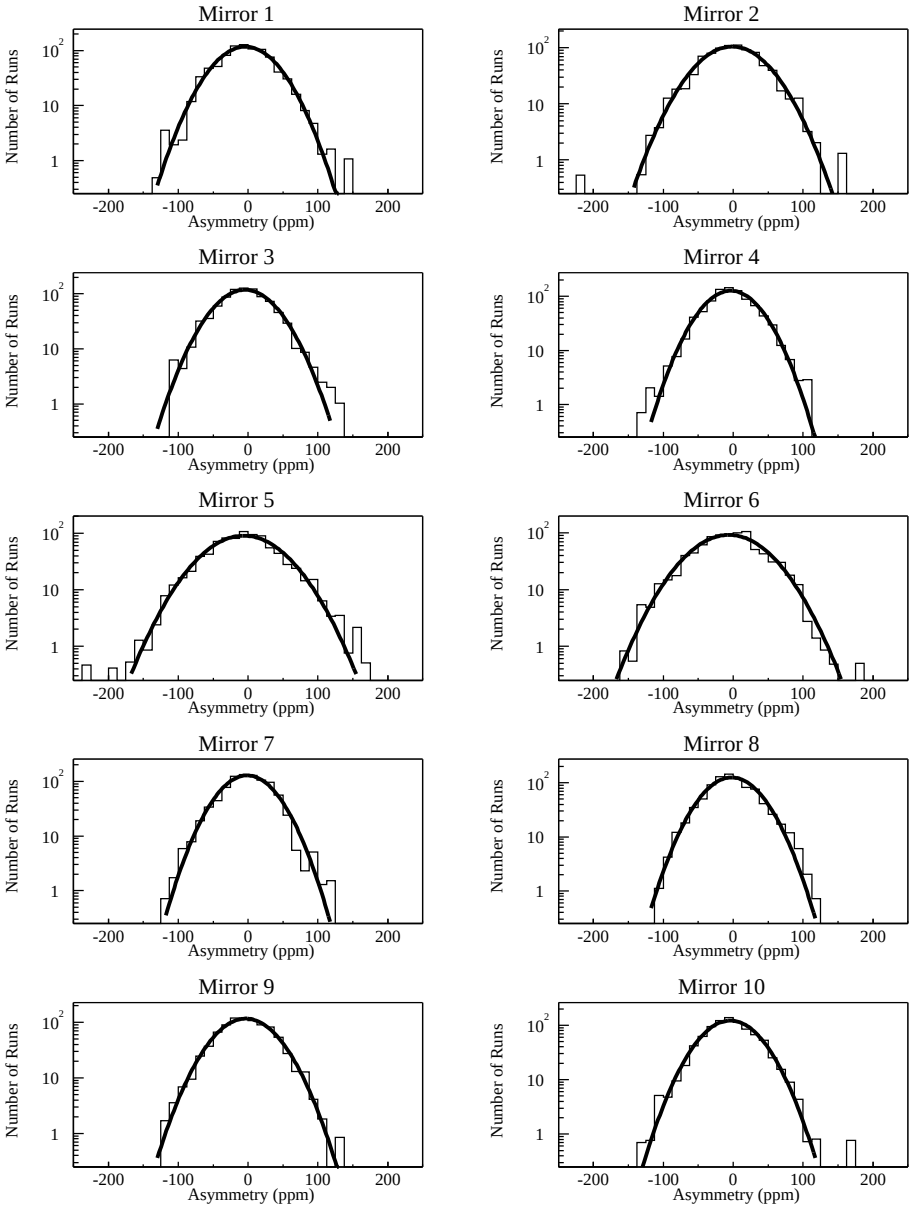

Figure 3.5: Corrected asymmetries for each mirror for all open shutter runs (a minus sign has been applied to the helicity out data to account for helicity reversal). The beam polarization has been divided out of each asymmetry and the value weighted by the statistical error on each average measurement. The histograms have been renormalized so that the integral I_h is equal to the number of runs $N = 871$. The curves are the Gaussian probability distributions for the mean asymmetries and errors tabulated in Table 3.6 over a range of $\pm 3.5\Sigma$ (see equations 3.4 - 3.6).

3.5 is used to put a systematic error on the corrections procedure. The relative systematic error on A_O^C is $\frac{0.19}{3.44} = 6\%$. This is the same as applying a 100% error bar to the actual mirror correction.

3.3 Dilution Factors

As discussed in Section 3.1.2, the dilution factors play an important role in extracting the physics asymmetry A_p from the measured asymmetry A_O^U. The data from which these factors are extracted come, for the most part, from measurements outside of the normal integration running on the primary detector. Each of these measurements requires its own data analysis procedure; these procedures are presented in the following sections.

3.3.1 Beam Polarization

The Møller polarimeter described in Section 2.3 was used to perform beam polarization measurements. These measurements were performed every other day and were sensitive to the longitudinal and transverse components of the beam polarization.

The measured asymmetry A_E differs from the Møller asymmetry A_M due to the presence of background processes. The yield measured in the Møller Čerenkov detector can be written as the sum of a helicity dependent signal $S^{\pm}$ due to Møller scattering and a helicity independent signal B due to background processes: $Y^{\pm} =$

$S^{\pm} + B$. The measured asymmetry is found by taking the difference in yield in the two helicity states over the sum:

$$\begin{aligned} A_E &= \frac{Y^+ - Y^-}{Y^+ + Y^-} \\ &= \frac{S^+ + B - (S^- + B)}{S^+ + B + (S^- + B)} \\ &= \left(\frac{S^+ - S^-}{S^+ + S^-}\right)\left(1 + \frac{2B}{S^+ + S^-}\right)^{-1} \\ A_E &= \frac{A_M}{1 + B/S} \end{aligned} \tag{3.35}$$

where $S = \frac{1}{2}(S^+ + S^-)$ and $A_M \equiv \frac{S^+ - S^-}{S^+ + S^-}$. Equation 3.35 can be used to extract A_M from A_E once the background-to-signal ratio B/S has been determined. As discussed in Section 2.3 data are collected well above and below the Møller peak so that this ratio can be extracted precisely.

The Čerenkov yield Y was measured as a function of magnetic field setting V_S, or "Shunt Voltage". Since the magnetic field determines the energy of the detected electrons this was the same as measuring the yield as a function of energy. The measured signal consists of a peak due to Møller scattering plus a linear background. The yield data were fit to the following function:

$$Y(V_S) = Me^{-\frac{1}{E}\left|\frac{V_S - P}{W}\right|^E} + B_0 + B_1(V_S - P) \tag{3.36}$$

where the parameters M, E, P, W, B_0, and B_1 were allowed to vary. The first term of this equation constitutes the signal S and the last two terms constitute the background B. Therefore the background-to-signal ratio as a function of V_S

is given by

$$\frac{B}{S}(V_S) = \frac{B_0 + B_1(V_S - P)}{Me^{-\frac{1}{E}\left|\frac{V_S - P}{W}\right|^E}}. \tag{3.37}$$

It was found to have a value of approximately $\frac{1}{5}$ at the Møller peak. Once B/S was determined the Møller asymmetry was extracted by fitting the asymmetry data to equation 3.35 and allowing A_M to vary. Representative Møller yield and asymmetry data, along with the appropriate fits, are shown in Figure 3.6. A relative systematic error of 4.2% is assigned to the determination of P_B^z due to the measurement of B/S (3.2%), the target polarization P_T (2.0%), and the target angle θ_T (1.0%), depolarization of the target due to beam heating (1.5%), and the possibility of an asymmetry in the background (0.5%). [Pit01].

Data are taken at positive and negative values of the target foil angle θ_T (Section 2.3). The Møller asymmetries from each setting are determined according to the above procedure and combined to extract the longitudinal and transverse beam polarizations.

Longitudinal

As the target foil angle reverses sign, $\theta_T \to -\theta_T$, the longitudinal target polarization P_T^z is unaffected, but the transverse polarization changes sign $P_T^x(-\theta_T) = -P_T^x(\theta_T)$ (equations 2.11 and 2.9). The beam polarization P_B is unaffected by changes in θ_T therefore, according to equation 2.5, taking the sum of the Møller asymmetries at $\pm\theta_T$ causes the sensitivity to transverse beam polarization to

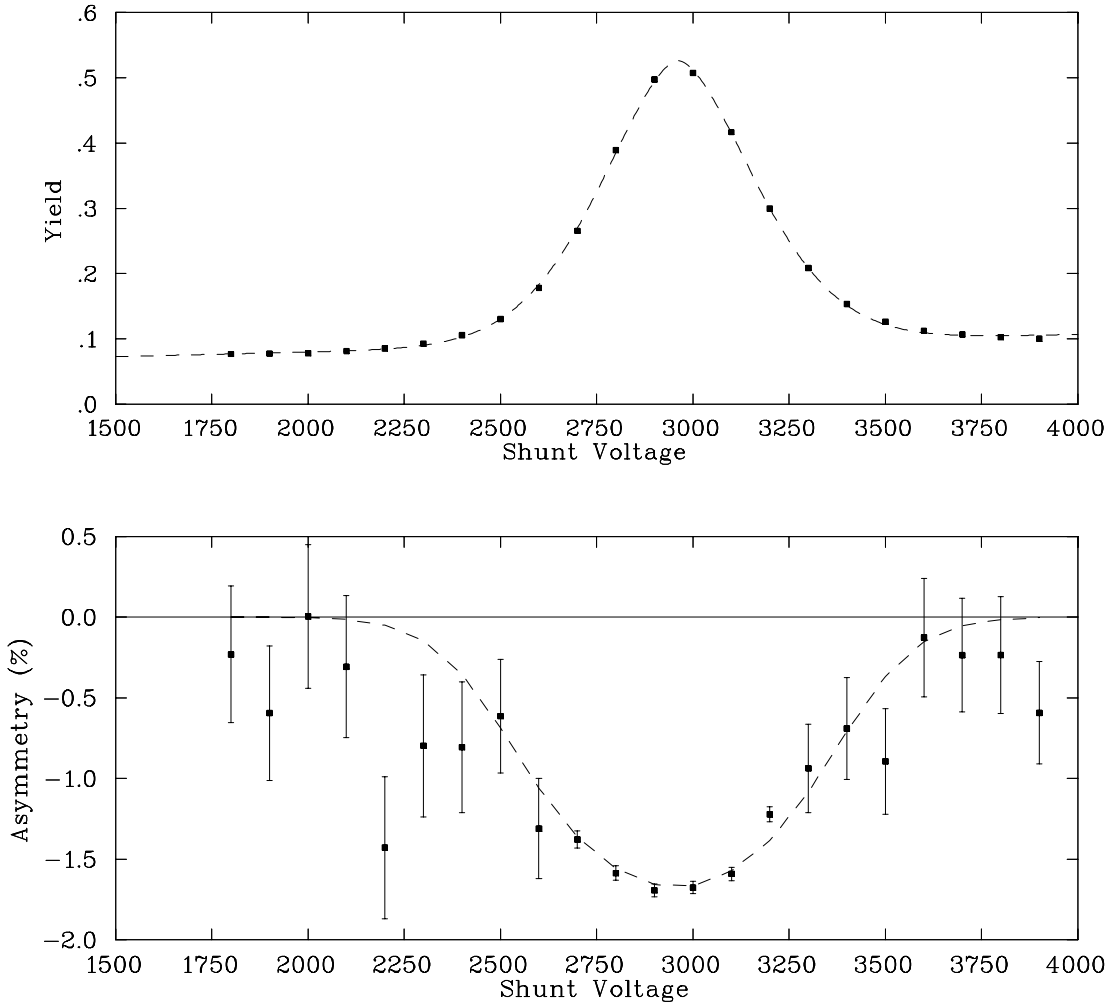

Figure 3.6: Møller yield and asymmetry data as a function of shunt voltage V_S from run number 2507. The fits to equations 3.36 and 3.35 are shown by the dashed lines in each graph.

drop out*. The longitudinal beam polarization is determined by the relationship

$$P_B^z = -\frac{9}{14}\frac{A_M(\theta_T) + A_M(-\theta_T)}{P_T \cos\theta_T} \tag{3.38}$$

where $P_T = (8.03 \pm 0.12)\%$ as discussed in Section 2.3.

Figure 3.7 shows the longitudinal beam polarization as a function of time. The average polarization varied from day to day as a result of the changing quantum efficiency (QE) of the GaAs crystal used to generate polarized electrons. The crystal's QE drops over time, resulting in an increase in beam polarization. Eventually the QE drops so low that 40μA of beam current cannot be maintained and the crystal must be reconditioned. This procedure takes several hours so it was performed only as needed. The QE increases dramatically (from approximately 0.3% to 2%) after reconditioning, causing a corresponding decrease in the beam polarization. The dips in Figure 3.7 correspond to periods immediately after a crystal reconditioning.

In this analysis the polarization correction was applied on a run-by-run basis, using the measurement closest in time to a given run, according to equation 3.13. Runs immediately after a crystal reconditioning were corrected by the first beam polarization measured after the reconditioning occurred. The beam polarization applied to each set of runs is listed in Table 3.7.

*This assumes that there is no out-of-plane component to the target polarization. In other words, the target foil is assumed to be perfectly vertical with no tilt about the x axis.

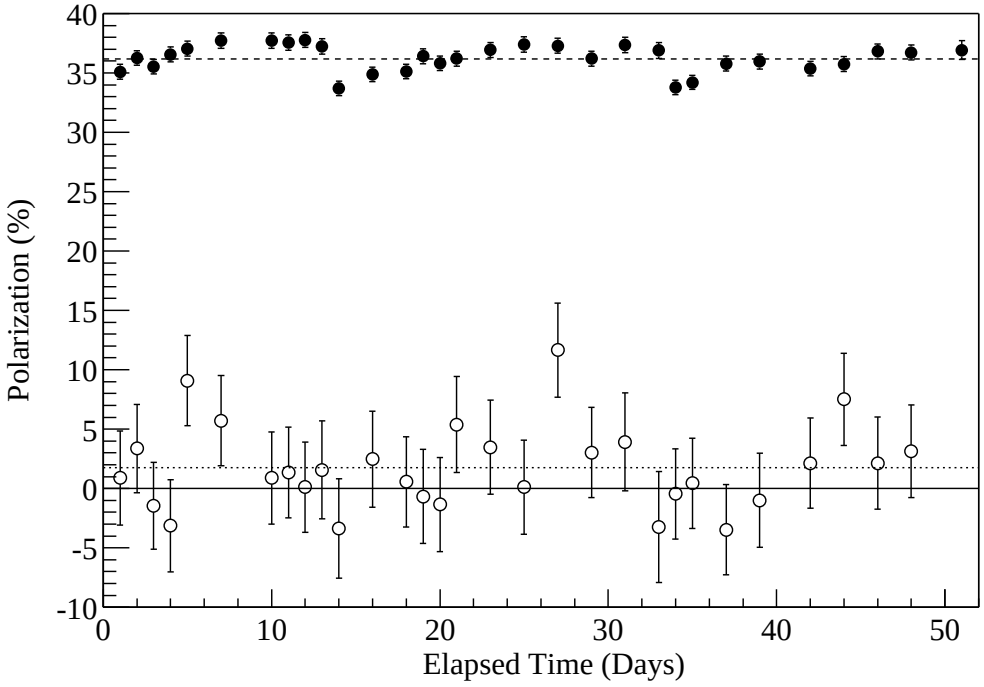

Figure 3.7: Longitudinal (filled circles) and transverse (open circles) beam polarization as a function of time. The dashed (dotted) line is the average longitudinal (transverse) polarization for the experiment, $P_B^z = (36.19 \pm 0.11)\%$ and $P_B^x = (1.75 \pm 0.71)\%$ where the errors are due solely to the statistics of the asymmetry measurement. The drops in beam polarization correspond to periods after the GaAs crystal was reconditioned.

Run Numbers	$A_M(\theta_T)(\%)$	$A_M(-\theta_T)(\%)$	$P_B^z(\%)$	$P_B^x(\%)$
2163–2216	1.902(26)	1.894(24)	35.1(6)	0.9(4.0)
2217–2258	1.976(24)	1.946(23)	36.3(6)	3.4(3.7)
2259–2302	1.915(23)	1.928(23)	35.5(6)	-1.5(3.6)
2303–2346	1.963(25)	1.991(24)	36.6(6)	-3.1(3.9)
2347–2398	2.044(24)	1.963(24)	37.0(6)	9.1(3.8)
2399–2467	2.065(24)	2.014(24)	37.7(6)	5.7(3.8)
2468–2530	2.045(24)	2.037(25)	37.7(6)	0.9(3.9)
2531–2570	2.037(24)	2.025(24)	37.5(6)	1.3(3.8)
2571–2602	2.044(24)	2.043(24)	37.8(6)	0.1(3.8)
2603–2620	2.020(26)	2.006(26)	37.2(6)	1.6(4.1)
2621–2678	1.807(27)	1.837(26)	33.7(6)	-3.4(4.2)
2679–2741	1.897(25)	1.875(26)	34.9(6)	2.5(4.0)
2742–2801	1.903(24)	1.898(24)	35.1(6)	0.6(3.8)
2802–2848	1.966(25)	1.972(25)	36.4(6)	-0.7(4.0)
2849–2890	1.931(25)	1.943(25)	35.8(6)	-1.3(4.0)
2891–2952	1.982(26)	1.934(25)	36.2(6)	5.4(4.0)
2953–3033	2.013(25)	1.982(25)	36.9(6)	3.5(4.0)
3034–3119	2.024(25)	2.023(25)	37.4(6)	0.1(4.0)
3120–3188	2.069(25)	1.965(25)	37.3(6)	11.7(4.0)
3189–3240	1.972(24)	1.945(24)	36.2(6)	3.0(3.8)
3241–3288	2.038(27)	2.003(25)	37.4(6)	3.9(4.1)
3289–3310	1.981(30)	2.010(29)	36.9(6)	-3.3(4.7)
3311–3346	1.825(24)	1.829(24)	33.8(5)	-0.4(3.8)
3347–3384	1.852(24)	1.848(24)	34.2(5)	0.4(3.8)
3385–3434	1.920(24)	1.951(24)	35.8(6)	-3.5(3.8)
3435–3489	1.941(25)	1.950(25)	36.0(6)	-1.0(4.0)
3490–3544	1.922(24)	1.903(24)	35.4(6)	2.1(3.8)
3545–3590	1.967(24)	1.900(25)	35.7(6)	7.5(3.9)
3591–3640	2.001(24)	1.982(25)	36.8(6)	2.1(3.9)
3641–3702	2.000(24)	1.972(25)	36.7(6)	3.1(3.9)
3703–3819	1.997(31)	N/A	37.1(6)	N/A

Table 3.7: Longitudinal beam polarization for each integration mode run and the associated in-bend-plane transverse polarization. The final beam polarization measurement did not include a measurement at $-\theta_T$, therefore P_B^x could not be calculated. P_B^z for this measurement was calculated by assuming that $P_B^x = 0$.

Transverse

The transverse, in-bend-plane component of the beam polarization P_B^x can also be determined from a pair of Møller asymmetry measurements performed at $\pm\theta_T$. Taking the difference in these asymmetries causes the longitudinal polarization to drop out, leaving sensitivity only to the transverse components. The x component of beam polarization is determined by the following equation:

$$P_B^x = -\frac{9}{2}\frac{A_M(\theta_T) - A_M(-\theta_T)}{P_T \sin\theta_T}. \tag{3.39}$$

As Figure 3.7 illustrates, the behavior of the transverse polarization appears to be governed by the statistics of the measurement. The average transverse polarization is found to be quite small, $\langle P_B^x \rangle = (1.75 \pm 0.71)\%$. Under the assumption that there is no component of P_B along y this determination of P_B^x constitutes a limit on the amount of transverse beam polarization P_B^T in the experiment. The individual measurements are listed in Table 3.7.

3.3.2 Light Fraction

The light fraction f_l was extracted for each mirror during the course of the normal measurement using runs with the PMT shutters closed. It is simply the fraction of the measured yield in the PMTs due to light, be it Čerenkov or scintillation:

$$f_l \equiv \frac{Y_O - Y_C}{Y_O} \tag{3.40}$$

PMT	Y_O(PE/nC)	Y_C(PE/nC)	f_l	f_e
1	345.8	52.4	0.848	0.886 ± 0.017
2	281.9	51.5	0.817	0.868 ± 0.029
3	251.8	36.5	0.855	0.860 ± 0.019
4	483.8	63.2	0.869	0.867 ± 0.009
5	241.3	81.7	0.661	0.863 ± 0.042
6	215.7	74.4	0.655	0.874 ± 0.017
7	318.1	42.8	0.865	0.764 ± 0.025
8	264.7	36.5	0.862	0.794 ± 0.033
9	291.8	49.1	0.832	0.864 ± 0.023
10	370.4	55.0	0.851	0.961 ± 0.026

Table 3.8: The measured PMT yield for each mirror-PMT combination averaged over the entire experiment for open and closed shutter runs. The units are number of photoelectrons per nanoCoulomb (PE/nC). Equation 3.40 is used to extract the light fraction f_l. The relative error is 100 times smaller than the error on the yield measurement, negligible compared to the errors on the other dilution factors. The elastic fraction f_e for each mirror is listed as well.

where Y_O is the PMT yield during an open shutter run and Y_C is the yield when the shutters are closed. One out of every four runs was a closed shutter run so there was ample data with which to form f_l. Table 3.8 summarizes the results for f_l for each mirror. The relative errors on f_l are 100 times smaller than those on a yield measurement and are a negligible contribution to the systematic error on A_p.

3.3.3 Elastic Fraction

The elastic fraction f_e was extracted from the pulse counting data discussed in Section 2.7.1. It is the fraction of the total light yield due to Čerenkov light from charged particles; the combination $f_l f_e(1 - f_\pi)$ determines the fraction of

the total open shutter signal due to elastically scattered electrons. The small contribution to the charged particle signal from the products of pion decay f_π will be discussed in Section 3.4.2.

In order to extract f_e, normal data taking was stopped and a coincidence experiment was performed between the Čerenkov PMTs and the scintillator paddles placed behind certain mirrors (Figure 2.18). The paddles were only triggered by the passage of charged particles, i.e. electrons and positrons; the Čerenkov PMTs responded to all incident light. A coincidence between a scintillator paddle and the corresponding Čerenkov PMT indicated that the light signal was associated with an elastically scattered electron or a charged particle from pion decay (Section 3.4.2) or pair production from high energy photons (Section 3.3.4). Data were taken with shutters open and closed in order to extract the portion of the signal due to light. This is necessary because a correction for the light fraction is already applied as discussed in Section 3.3.2.

Pulse height and timing data were collected for coincidences between a scintillator paddle and the corresponding Čerenkov PMT as well as singles data for the Čerenkov PMT alone. The elastic fraction is defined as the ratio of integrated light yields in the coincidence Y_L^c and singles Y_L^s spectra. These spectra are extracted from the appropriate pulse height spectra by normalizing to the total beam charge:

$$f_e \equiv \frac{Y_L^c}{Y_L^s}. \tag{3.41}$$

In the case of singles, the light yield was found by subtracting the shutter closed pulse height spectrum from the shutter open spectrum, both normalized to the incident beam charge.

Dark noise was also subtracted from all three pulse height spectra: coincidence, singles open shutter, and singles closed shutter. The dark noise was due to the random emission of an electron somewhere along the PMT dynode chain that generated enough current at the anode to trigger the data acquisition; this noise was completely uncorrelated with the photons incident on the PMT cathode. Dark noise shows up in the pulse height spectra as one photoelectron (number of electrons knocked off the PMT cathode) events or less, but it is not possible to simply cut the single photoelectrons events away because inelastic processes in the experiment can also result in a one photoelectron (PE) signal. The data acquisition was set up to collect data during a 50 μs period that included the 25 μs period of time when the beam was on. Events outside the beam window due to dark noise were used to subtract away the dark noise portion of the one PE peak during the beam window.

A timing spectrum is shown in Figure 3.8, the period of time during which there was beam is clearly delineated. The distribution of events in the period before and after the beam is assumed to be flat as a function of time, but not necessarily the same [Ito99]. During the beam window, the number of events detected as a function of time decreases exponentially. This is due to the fact

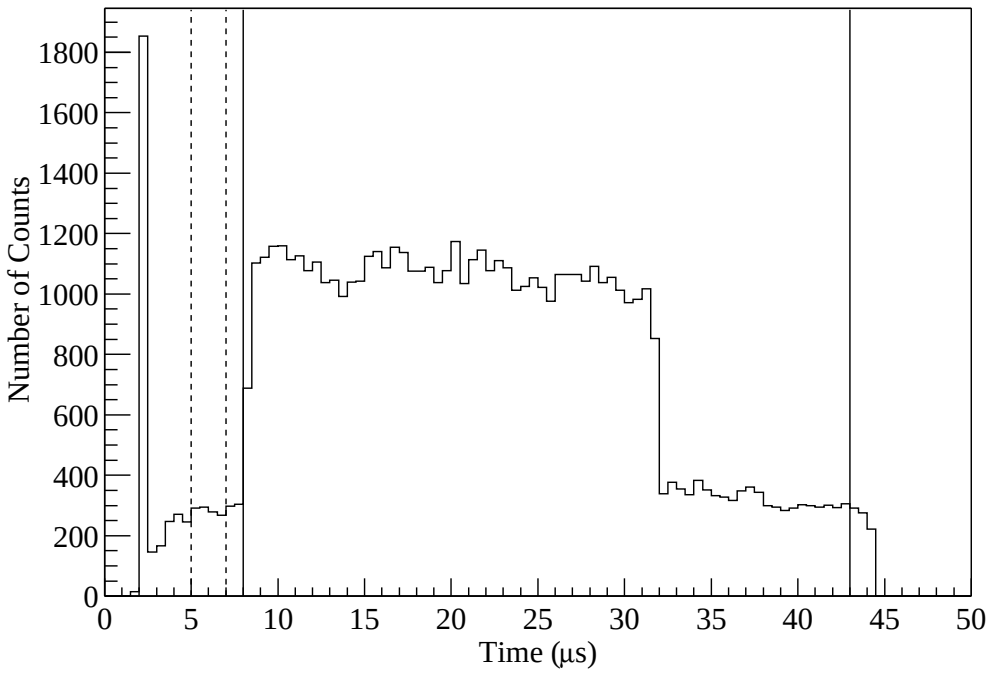

Figure 3.8: The Čerenkov PMT singles time spectrum. The solid (dashed) lines represent the time window $\Delta t_B + \Delta t_A$ (Δt_P).

that the data acquisition accepts only one event per 50 μs long acquisition period; events that come early in this time span prevent later events from being counted. This drop off is given by an exponential that decays in time with a constant λ equal to the rate at which events are collected. In the "dark noise only" region this rate is low enough that the exponential can be approximated by a constant. A pulse height spectrum consisting of events in a time window of length Δt_P before the arrival of the beam constitutes the dark noise spectrum for the singles events. Events that arrive during the beam pulse, time window Δt_B, plus those that arrive for Δt_A after the pulse ends are included in the singles pulse height

spectrum. The period of time after the arrival of the beam pulse is included in the spectrum because the integration data acquisition samples this region as well.

For open shutter runs the dark noise spectrum is normalized by the factor [Ito99]

$$N_s^O = \frac{1}{\Delta t_P}\left(\int_0^{\Delta t_B} e^{-\lambda t}\mathrm{d}t + \Delta t_A e^{\lambda \Delta t_B}\right). \tag{3.42}$$

This factor corrects for the data acquisition (DAQ) dead time during the time the electrons arrive. DAQ dead time is low during this same time span for shutter closed runs, so the following normalization factor is used:

$$N_s^C = \frac{\Delta t_B + \Delta t_A}{\Delta t_P}. \tag{3.43}$$

The DAQ rate λ is the sum of all singles and coincidence events divided by the total number of beam pulses and the length of the pulse. Once the open and closed shutter singles pulse height spectra have been dark noise subtracted the light spectrum is formed by subtracting the closed spectrum from the open spectrum. Before this subtraction occurs each spectrum is normalized to the total beam charge for the run, the total number of singles for the run divided by the number of singles in the histogram and the total incident beam charge. The total number of singles events can be different from the number in the histogram because the singles that enter the DAQ are prescaled by a known amount, usually 256.

There is much more dark noise in the singles spectra than in the coincidence

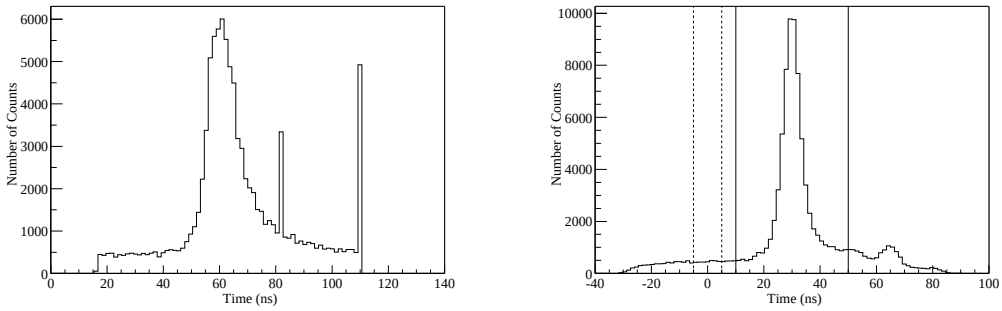

(a) Uncorrected Timing Spectrum (b) Corrected Timing Spectrum

Figure 3.9: The coincidence time spectrum without and with the correction for time walk. The solid (dashed) lines represent the time window Δt_C (Δt_D). The spike at approximately 80 ns is due to time walk occasionally causing the Čerenkov PMT to generate both the TDC start and stop signals (generally the scintillator PMT sets the coincidence timing). The spike at 110 ns consists of coincidence events that did not receive a TDC stop signal before the digitization time window was exceeded.

spectra because the accidental coincidence rate is significantly lower than the singles rate, but there can still be accidental coincidences with dark noise. Figure 3.9(a) shows the raw coincidence timing spectrum, the peak corresponding to real coincidences is clearly visible. Since the timing is determined by leading edge discriminators it is necessary to correct the coincidence time for "time walk" caused by forming coincidences between pulses with different amplitudes and/or rise times. Figure 3.9(b) shows the coincidence timing spectrum corrected for time walk. The coincidence pulse height spectrum consists of events that occur during the coincidence peak in the corrected timing spectrum (during time window Δt_C). The dark noise spectrum is collected during a time window Δt_D before

the coincidence peak and is then normalized by $\frac{\Delta t_C}{\Delta t_D}$ before being subtracted from the coincidence spectrum. Both the dark noise and the coincidence spectra are normalized to the beam charge before the subtraction occurs, the same as for the singles spectra.

It is necessary to scale up the dark subtracted coincidence pulse height spectrum due to the difference in geometric acceptance of the scintillator paddles and the Čerenkov PMTs. The Čerenkov PMTs sample the entire mirror, but the paddle only samples a small portion near the center of the mirror. The coincidence spectrum is scaled up until it agrees with the singles spectrum in the region with yield greater than 3 PE, where the signal is entirely due to Čerenkov photons. Figure 3.10 shows the singles pulse height spectrum and the scaled up coincidence spectrum; the integrals of these two spectra are the light yields $Y_L^{s/c}$ necessary to calculate f_e according to equation 3.41.

There is another geometric effect to consider, the "mirror edge effect" that arises from electrons that intersect the edges of the mirror [Ave98]. Electrons that strike near a mirror edge can lose some fraction of their cone of Čerenkov photons. Similarly, electrons that miss the mirror can still be detected because some of their Čerenkov photons intersect the mirror. The net result of this is that some electron events that would appear in the high PE region of the singles ADC spectrum are shifted down, causing a deformation of the high PE region of the spectrum. This deformation will not be present in the coincidence spectrum

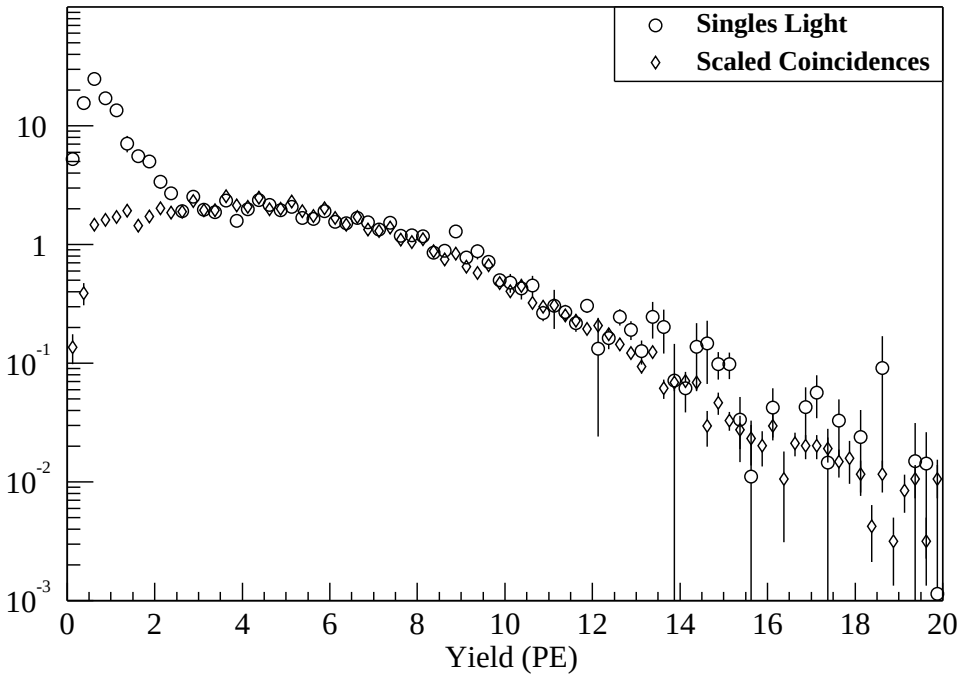

Figure 3.10: The singles and coincidence ADC spectra.

since the paddles are not near the edges of the mirrors. Therefore, scaling the coincidence yield to agree with the singles yield in the greater than 3 PE region underestimates the coincidence yield. The correction factor was calculated to be 1.05 and a Monte Carlo simulation was able to verify this to within a few percent (1.084) [Ave98, Tie98]. The final values for f_e were extracted by multiplying equation 3.41 by 1.05; the results for all ten mirrors are shown in Table 3.8. A relative systematic error of 4% has been assigned to the determination of f_e; there is a 3% contribution from the statistics of determining f_e and the remainder is due to a consideration of the various systematic effects.

3.3.4 Electromagnetic Radiative Corrections

Electroweak radiative corrections to the various form factors were discussed in Section 1.2.4. Those corrections arise from diagrams involving the exchange of extra Z bosons. The radiative corrections addressed in this section are purely electromagnetic, emission and absorption of real and virtual photons. This topic was treated by Mo and Tsai [MT69] and their results have been utilized extensively here. Their treatment was for unpolarized e-p scattering, so some extensions have been made to account for the polarization of the electrons.

Electromagnetic radiative corrections can be grouped into two types: external and internal. External corrections are due to the emission of a real photon by the electron in the field of a target nucleus other than the one that scatters the electron into the detector acceptance. This bremsstrahlung radiation can occur before or after the parity violating scattering interaction. Internal corrections involve the emission of a real photon by an electron at the parity violating interaction point. The two contributing Feynman diagrams for internal bremsstrahlung are shown in Figure 3.11.

There are two effects due to the emission of photons prior to the parity violating interaction:

1. the energy of the electron is reduced, leading to a lower value of Q^2 and of the asymmetry for a given scattering angle θ, and

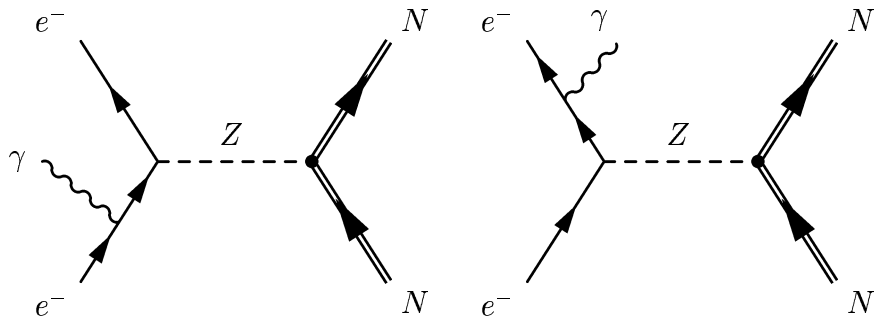

(a) Internal Before (b) Internal After

Figure 3.11: Diagrams for internal before and after bremsstrahlung radiation.

2. the spin of the electron can be flipped, giving a net depolarization.

Both of these effects reduce the measured asymmetry with respect to the tree level asymmetry. The emission of photons after the parity violating interaction reduces the energy of the scattered electron leading to a reduction in the detector signal due to the fewer number of emitted Čerenkov photons (Figure 2.12). The emission of post-interaction bremsstrahlung photons can cause low energy electrons to fall below the Čerenkov threshold and not be detected; since these electrons tend to be correlated with small asymmetries the measured asymmetry would increase. However, high energy electrons that emit bremsstrahlung photons will emit fewer Čerenkov photons thereby reducing their weight relative to the other elastically scattering electrons. The combined effect of these processes can be evaluated with the Monte Carlo computer simulation discussed below.

In the absence of external and internal bremsstrahlung the cross section for

elastic scattering of an electron from a nucleon is given by [HM84]:

$$\begin{aligned}\frac{\mathrm{d}\sigma_E}{\mathrm{d}\Omega}(E_s,\theta) =& \frac{\alpha^2}{4E_s^2\sin^4\frac{\theta}{2}}\frac{E_p^M}{E_s} \\ &\times\left[\frac{(G_{E,\gamma}^N)^2+\tau(G_{M,\gamma}^N)^2}{1+\tau}\cos^2\frac{\theta}{2}+2\tau(G_{M,\gamma}^N)^2\sin^2\frac{\theta}{2}\right]\end{aligned} \tag{3.44}$$

where E_s is the energy of the incident electron, E_p^M is the energy of the elastically scattered electron, and $\tau \propto Q^2$ is defined in equation 1.29*. The scattered energy is constrained by relativistic kinematics to be

$$E_p^M \equiv \frac{E_s}{1+\frac{2E_s}{M_N}\sin^2\frac{\theta}{2}} \tag{3.45}$$

where M_N is the mass of the target nucleon. The effect of internal and external bremsstrahlung is to remove electrons from the elastic peak and put them into a long tail. Ionization also affects this distribution, but more by smearing out the elastic peak to lower energies than adding to the radiative tail [MT69].

In order to calculate the radiative correction R_c it is necessary to calculate two different parity violating asymmetries: the tree level asymmetry A_p^T of single boson exchange (Figure 1.1) and the asymmetry A_p^R including the electromagnetic radiative effects. The radiative correction is simply the ratio of these two asymmetries,

$$R_c = \frac{A_p^T}{A_p^R}. \tag{3.46}$$

An accurate calculation of A_p^T and A_p^R requires knowledge of the detector geometry.

*The notation in this section follows that of Ref. [MT69]

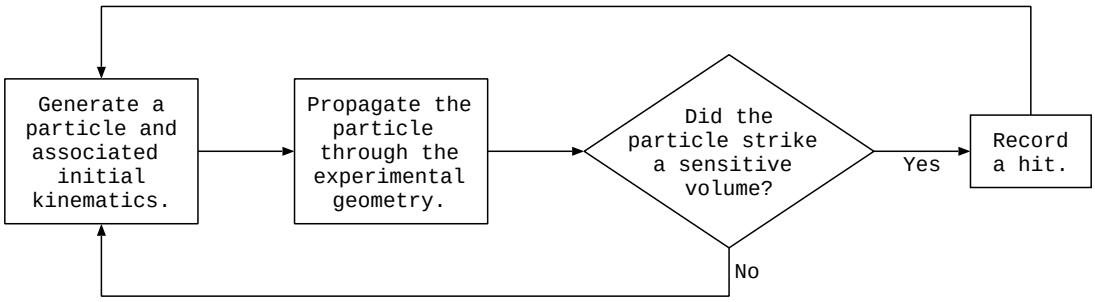

Figure 3.12: A flowchart of the logic behind the GEANT calculation. The circuit is interrupted when a predetermined number of particles has been generated.

Details of the Calculation

The GEANT detector simulation package developed at CERN was used to model the SAMPLE apparatus in the calculation of A_p^T and A_p^R [Gro94]. With this package the user defines a detector geometry through which particles are propagated and undergo realistic physics processes. The detector setup defined for this calculation included the target, vacuum chamber, mirrors, photomultiplier tubes, and lead shielding. Figure 3.12 shows the flow of logic in the program. Each aspect of the calculation presented in the flowchart will be dealt with separately in the discussion that follows.

Particle Generation The generation of particles in the GEANT simulation is a four step process:

1. Generate an electron at a random point in z along the central axis of the target cylinder, within the target volume (see Figure 2.13 for a schematic of the coordinate system).

2. Assign a random scattering direction to the electron.

3. Assign a random scattering energy to the electron.

4. Calculate the cross section and parity violating asymmetry for that scattering process.

The scattering angle is chosen randomly in a range of $0.001 \leq \theta < \pi$ radians and $0 \leq \phi < 2\pi$ radians. The scattered electron energy is randomly chosen from 5 MeV up to E_p^M.

The position of the incident electron in the target determines its energy E_s at the interaction point. In the absence of ionization E_s would be the energy of the incident beam $E_0 = 200$ MeV. However, the passage of the electron through the target volume to get to the interaction point reduces its energy resulting in the elastic peak smearing mentioned previously. The incident electron energy is determined by the following formula [Tsa71]:

$$E_s = E_0 - \Delta_{Al}(E_s, t_{Al}) - \Delta_{H_2}(E_s, t_{H_2}) \tag{3.47}$$

where Δ_{Al} is the energy loss due to ionization in a thickness t_{Al} of aluminum entrance window and Δ_{H_2} is the energy lost in passing through a thickness t_{H_2} of target material*. The energy loss is given by [Tsa71]:

$$\Delta_Z(E_s, t) = \xi(t) \left[\ln \left(\frac{3 \times 10^9 \xi(t) E_s^2}{m_e^2 Z^2} \right) - 0.5772 \right] \tag{3.48}$$

*The energy lost in the aluminum window is a negligibly small constant.

where t^* is the number of radiation lengths traveled by the electron, and

$$\xi(t) = a(Z)x_0 t \tag{3.49}$$

$$a(Z) = \frac{2\pi N_A \alpha^2}{m_e}\frac{Z}{A}. \tag{3.50}$$

N_A is Avogadro's number and x_0 is the unit radiation length of the material in g/cm^2.

After E_s and θ have been determined, the elastic scattering energy E_p^M is calculated according to equation 3.45 and the actual scattered energy E_p, which includes losses due to bremsstrahlung, is selected randomly. The calculation of the cross section and asymmetry depends on how close E_p is to E_p^M. If E_p is within $\Delta E = 1$ MeV of E_p^M, then the electron is assumed to have elastically scattered without any bremsstrahlung processes having occurred. The cross section for this is related to the elastic scattering cross section via the following equation [Tsa71]:

$$\frac{\mathrm{d}\sigma_R}{\mathrm{d}\Omega}(E_p,\theta) = e^{\delta}\left(\frac{R\Delta E}{E_s}\right)^{bt}\left(1-\frac{\xi}{\Delta E}\right)\left[G(\theta,t_{H_2})\frac{\mathrm{d}\sigma_E}{\mathrm{d}\Omega}(E_p,\theta)\right]. \tag{3.51}$$

These factors all reduce the elastic cross section at the peak to account for electrons that have radiated into the tail. The factor G is coupled with the Mott cross section to form an effective cross section both at the elastic peak and, as will be shown in the next section, in the radiative tail. It is very close in value

*In Ref. [Tsa71] $t \to \frac{T}{2}$ where T is the total length of the target.

to 1 [Tsa71]:

$$G(\theta, t_{H_2}) = 1 + 0.5772 b_{H_2} t_{H_2} + \frac{\alpha}{\pi}\left[\frac{\pi^2}{6} - \Phi\left(\cos^2\frac{\theta}{2}\right)\right] \tag{3.52}$$

$$b = \frac{4}{3}\left[1 + \frac{1}{9}\frac{Z+1}{Z+\eta}(\ln 183 Z^{-1/3})^{-1}\right] \approx \frac{4}{3} \tag{3.53}$$

$$\eta = \frac{\ln 1440 Z^{-2/3}}{\ln 183 Z^{-1/3}} \tag{3.54}$$

where the Spence function $\Phi(x) \equiv \int_0^x \frac{-\ln|1-y|}{y} dy$. The factor $\left(\frac{R\Delta E}{E_s}\right)^{bt}$ is due to the emission of external bremsstrahlung; the exponent $bt = b_{Al} t_{Al} + b_{H_2} t_{H_2}$ indicates the passage of the electron through the entrance window and the target volume. The maximum allowed energy of a real photon that can be emitted along the incident direction is given by $R\Delta E$ [Tsa71]:

$$R \equiv \frac{\omega_s}{\omega_p} \tag{3.55}$$

$$\omega_s = \frac{1}{2}\frac{u^2 - M_p^2}{M - E_p(1-\cos\theta)} \tag{3.56}$$

$$\omega_p = \frac{1}{2}\frac{u^2 - M_p^2}{M + E_s(1-\cos\theta)} \tag{3.57}$$

where $u^2 = 2m_e^2 + M_p^2 + Q^2 + 2M_p(E_s - E_p)$ is the missing mass squared. There is a similar term for external bremsstrahlung after the interaction, but it is neglected for this calculation (external after bremsstrahlung is handled by GEANT). The term e^δ is a correction that can be found in Ref. [MT69] (equation II.5) and the factor $\left(1 - \frac{\xi}{\Delta E}\right)$ is a very small reduction due to high energy loss ionization events. The parity violating asymmetry at the elastic peak $A_p^{EP}(E_s)$ is calculated according to equation 1.65 assuming that $G_M^s = 0$.

If E_p is less than $E_p^M - \Delta E$, then a high energy bremsstrahlung or ionization event must have occurred either before or after the interaction. It is then necessary to calculate the cross section for the radiative tail to the elastic peak which is given by Ref. [Tsa71]:

$$\frac{\mathrm{d}\sigma_T}{\mathrm{d}\Omega \mathrm{d}E_p}(E_s,\theta) = C_B(E_s,\theta)\frac{\mathrm{d}\sigma_E}{\mathrm{d}\Omega}(E_s-\omega_s,\theta) + C_A(E_s,\theta)\frac{\mathrm{d}\sigma_E}{\mathrm{d}\Omega}(E_s,\theta) \tag{3.58}$$

where $C_{B(A)}$ is a coefficient containing the contributions from bremsstrahlung and ionization before (after) the interaction point; these coefficients are much less than one. The energy of the photon emitted before (after) the interaction point is $\hbar\omega_{s(p)}$.

The coefficients $C_{B(A)}$ contain contributions from external bremsstrahlung, internal bremsstrahlung, and ionization [Tsa71]:

$$C_{B(A)} = G_{B(A)}(v_s)^{bt+b_{H_2}t_r}\left[C^{EB}_{B(A)} + C^{IB}_{B(A)} + C^{IO}_{B(A)}\right] \tag{3.59}$$

$$G_B = G(v_s)^{bt+b_{H_2}t_r}\frac{M_p + (E_s-\omega_s)(1-\cos\theta)}{M_p - E_p(1-\cos\theta)} \tag{3.60}$$

$$G_A = G(v_s)^{bt+b_{H_2}t_r} \tag{3.61}$$

$$t_r = \frac{1}{b_{H_2}}\frac{\alpha}{\pi}\left[\ln\left(\frac{Q^2}{m_e^2}\right) - 1\right] \tag{3.62}$$

where $v_s = \frac{\omega_s}{E_s}$ and t_r is the "equivalent radiator" to the internal bremsstrahlung. The contribution from internal bremsstrahlung can be thought of as coming from a pair of external radiators, before and after the interaction point, of length t_r in radiation lengths. As before, bt is a sum of Al and H_2 terms. The after interaction contributions from external bremsstrahlung C_A^{EB} and ionization C_A^{IO}

are set to zero for the purposes of this calculation; they are handled by the GEANT routines that propagate the scattered electron out of the target. These coefficients are given below [Tsa71]:

$$C_B^{EB} = \frac{bt}{\omega_s}\phi(v_s) \qquad C_A^{EB} = 0 \tag{3.63}$$

$$C_B^{IB} = \frac{bt_r}{\omega_s}\phi(v_s) \qquad C_A^{IB} = \frac{bt_r}{\omega_p}\phi(v_p) \tag{3.64}$$

$$C_B^{IO} = \frac{\xi}{2\omega_s^2} \qquad C_A^{IO} = 0 \tag{3.65}$$

where $v_p = \frac{\omega_p}{E_p+\omega_p}$. The external bremsstrahlung and ionization contributions due to photon emission before the interaction C_B^{EB} and C_B^{IO} contain a term due to emission in the H_2 target and a term due to the Al entrance window through the coefficient bt (see also equation 3.59). The function $\phi(v)$ gives the shape of the bremsstrahlung spectrum and is normalized such that $\phi(0) = 1$. Under the assumption of complete screening, $\phi(v) = 1 - v + \frac{3}{4}v^2$ [Tsa71].

As equation 3.58 indicates the incident electron can have two different energies at the interaction point: $E_s - \omega_s$ if an amount of energy ω_s is lost before the interaction and E_s if ω_p is lost after the interaction. This means that two parity violating asymmetries, $A_p(E_s-\omega_s)$ and $A_p(E_s)$ have to be calculated and averaged together for electrons in the tail. The proper weighting of the asymmetries to form the overall asymmetry in the tail A_p^{RT} is to use the appropriate portions of

the cross section in the tail:

$$A_p^{RT}\left[\frac{\mathrm{d}\sigma_T}{\mathrm{d}\Omega \mathrm{d}E_p}(E_s,\theta)\right] = A_p(E_s-\omega_s)\frac{\mathrm{d}\sigma_E}{\mathrm{d}\Omega}(E_s-\omega_s)G_B \times \left[C_B^{EB}(1-D^{EB})+C_B^{IB}(1-D^{IB})+C_B^{IO}\right] + A_p(E_s)\frac{\mathrm{d}\sigma_E}{\mathrm{d}\Omega}(E_s)G_A C_A^{IB} \tag{3.66}$$

where $D^{EB(IB)}$ is the depolarization of the incident electron due to a spin flip caused by the emitted photon. As before, the contribution from external bremsstrahlung and ionization before the interaction contain terms due to H_2 and Al; there is external bremsstrahlung depolarization due to the two materials individually as well. The term $C_B^{EB}(1-D^{EB})$ should be written as the sum of two terms of the same form, one for H_2 and one for Al. For simplicity, this dependence is not written explicitly.

Depolarization due to external bremsstrahlung radiation was calculated by Olsen and Maximon in Ref. [OM59]:

$$D^{EB}\left(E_s,E_p,\varsigma_s\right) = \frac{(E_s-E_p)^2\left[\psi_1-\varsigma_{sz}^2\left(\psi_1-\frac{2}{3}\psi_2\right)\right]}{\left(E_s^2-E_p^2\right)\psi_1-\frac{2}{3}E_sE_p\psi_2} \tag{3.67}$$

where ς_s is the unit spin vector of the initial electron (therefore $\varsigma_{sz}^2=1$). Under the assumption of complete screening the functions ψ_1 and ψ_2 can be written as follows:

$$\psi_1 = 4\left[\ln\left(\frac{183}{Z^{\frac{1}{3}}}\right)-f(Z)\right] \tag{3.68}$$

$$\psi_2 = \psi_1-\frac{2}{3} \tag{3.69}$$

$$f(Z) = (Z\alpha)^2\sum_{i=1}^{\infty}\frac{1}{i\left[i^2+(Z\alpha)^2\right]} \tag{3.70}$$

where Z is the number of protons in the medium through which the electron travels. It is straightforward to calculate $D_{H_2}^{EB}$ and D_{Al}^{EB} for inclusion in equation 3.66.

The depolarization due to internal bremsstrahlung, arising solely from hydrogen, is derived from the work of Kuchto and Shumeiko [KS83]. They calculated the cross section for the scattering of longitudinally polarized electrons from longitudinally polarized nucleons including the effects of internal bremsstrahlung. The result applicable to this calculation is

$$\left(1 - D^{IB}\right) \equiv \frac{t'_1}{t_1} = \frac{\left[E_s^2 + \left(E'_s\right)^2\right] \ln\left(\frac{Q^2}{m_e^2}\right) - 2\left(E_s^2 + E_s E'_s - \left(E'_s\right)^2\right)}{\left[E_s^2 + E_s E'_s\right] \ln\left(\frac{Q^2}{m_e^2}\right) - 2E_s E'_s} \tag{3.71}$$

where $E'_s = E_s - \omega_s$. It should be noted that this is not strictly a simple polarization factor, because $\left(1 - D^{IB}\right) \geq 1$ for small ω_s.

Particle Propagation After the cross section and asymmetry have been calculated for an electron with scattered energy E_p, GEANT propagates the particle away from the interaction point and through the experimental geometry. GEANT uses library routines to simulate various physics processes the electron can undergo: bremsstrahlung, ionization, multiple scattering, delta ray production, synchrotron radiation, pair production, and positron annihilation. As massive particles propagate through the air in the detector, the total number of Čerenkov photons generated N_c is calculated, $N_c = L\frac{\mathrm{d}N}{\mathrm{d}x}$ where L is the distance traveled in air and $\frac{\mathrm{d}N}{\mathrm{d}x}$ is given by equation 2.16. This number is used in determining the

relative weighting of electrons that eventually generate a signal in a PMT.

Particle Hit Some fraction of the electrons that are propagated by GEANT will intersect one of the detector mirrors, which are designated as sensitive volumes for the purpose of the simulation. The properties of these electrons at the time of the hit, including the cross section and parity violating asymmetry, are recorded into an ntuple for later use in calculating the radiative corrections. Before being recorded into the ntuple the electron's trajectory is reflected specularly from the mirror surface. This reflected trajectory is used to determine where the Čerenkov photons emitted by the electron would wind up. When extracting the radiative corrections a cut is placed so that only those trajectories that intersect a PMT are included.

Analysis

The simulation was run twice to extract final results. In the first run the external and internal bremsstrahlung were turned off, as were the interaction processes handled by GEANT, thereby simulating the tree level asymmetry*. Ten million electrons were generated for this run. In the second run all interaction processes were reactivated and five million electrons were generated. Fewer electrons can be generated in the Monte Carlo simulation than the actual experiment because a

*The ionization processes were left on so that the leading order and beyond leading order asymmetries were calculated at the same mean incident electron energy E_s.

	Unradiated			Radiated		
Mirror	No Cut	Cut	% Cut	No Cut	Cut	% Cut
1	112115	100709	10.2	35237	23775	32.5
2	197448	197291	0.1	64061	44226	31.0
3	112320	100731	10.3	35211	23554	33.1
4	84332	78561	6.8	26120	19510	25.3
5	257654	256561	0.4	83344	42930	48.5
6	257195	256124	0.4	83570	43290	48.2
7	84505	78807	6.7	26123	19460	25.5
8	112069	100592	10.2	35278	23825	32.5
9	196749	196607	0.1	63635	43683	31.4
10	112599	100993	10.3	35076	23623	32.7

Table 3.9: This table shows the number of events removed by requiring that the reflected electron trajectory intersect a PMT in the radiated and unradiated runs.

parity violating asymmetry is calculated for each electron and stored in an ntuple for analysis rather than having to count the number of electrons in each of two helicity states to form the asymmetry.

Since scattered electrons are generated isotropically in θ, ϕ, and E_p it is necessary to weight individual events by the probability for that result in order to extract the physics. The proper weighting function, ignoring effects due to the detector response, is

$$W_P = \frac{\mathrm{d}\sigma_R}{\mathrm{d}\Omega} \sin\theta \tag{3.72}$$

for elastic peak events and

$$W_P = \frac{\mathrm{d}\sigma_T}{\mathrm{d}\Omega \mathrm{d}E_p} \sin\theta \tag{3.73}$$

for radiative tail events. To model the effect of detector response the weighting factor was multiplied by the number of Čerenkov photons generated $W_D = N_C W_P$

and it was required that the reflected photons intersect a PMT. Table 3.9 shows the average number of particles that intersect each mirror type with and without the reflected photon cut and the percentage of events cut for both radiated (full experimental simulation) and unradiated (leading order elastic scattering only) runs.

Results

Figure 3.13 shows the tree level asymmetry A_p^T and radiated asymmetry A_p^R for each mirror as calculated in GEANT. The histogram is weighted by the factor W_D, each entry in the histogram increments the appropriate bin by W_D which is why the y axis label is not indicative of the number of events in the histogram. The wide peak around an asymmetry of 7-8 ppm corresponds to the elastically scattered electrons; the width of the peak reflects the wide range of scattering angles, and asymmetries, accepted by each mirror. The long tail up to 0 ppm for A_p^T is due to high energy ionization processes. This tail gets much larger once the bremsstrahlung processes are included for A_p^R.

As per equation 3.46, the radiative correction R_c is found by taking the ratio of the average values of A_p^T and A_p^R extracted from the histograms in Figure 3.13. The average asymmetries $\langle A_p^T \rangle$ and $\langle A_p^R \rangle$ and the radiative correction $R_c = \frac{\langle A_p^T \rangle}{\langle A_p^R \rangle}$ for each mirror are shown in Table 3.10 in the case where the PMT cut has been applied. The last column contains R_c in the case where the PMT cut has not

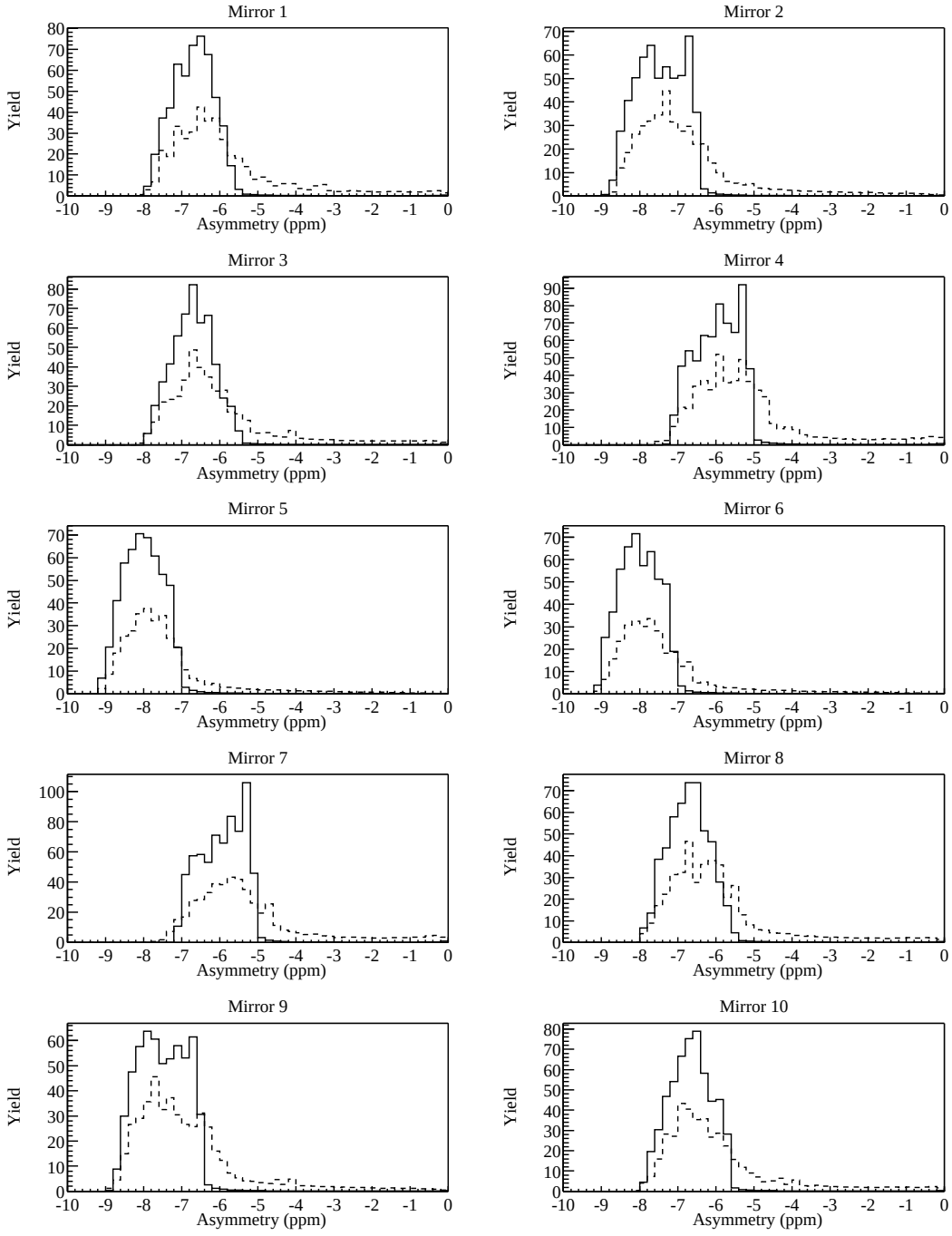

Figure 3.13: The tree level A_p^T (solid line) and radiated A_p^R (dashed line) asymmetry for each mirror. The radiated histogram has been scaled up by a factor of two to account for the difference in the number of initial electrons generated in each simulation. The average values of A_p^T and A_p^R can be found in Table 3.10.

Mirror	PMT Cut $\langle A_p^T \rangle$	PMT Cut $\langle A_p^R \rangle$	PMT Cut R_c	No PMT Cut R_c
1	-6.664 ± 0.020	-5.823 ± 0.034	1.144 ± 0.008	1.143 ± 0.006
2	-7.426 ± 0.016	-6.741 ± 0.030	1.102 ± 0.005	1.120 ± 0.004
3	-6.662 ± 0.020	-5.944 ± 0.035	1.121 ± 0.007	1.127 ± 0.006
4	-5.927 ± 0.020	-5.156 ± 0.033	1.150 ± 0.008	1.149 ± 0.007
5	-7.972 ± 0.015	-7.427 ± 0.034	1.073 ± 0.005	1.103 ± 0.004
6	-7.966 ± 0.015	-7.367 ± 0.033	1.081 ± 0.005	1.113 ± 0.004
7	-5.897 ± 0.020	-5.216 ± 0.034	1.130 ± 0.008	1.133 ± 0.007
8	-6.671 ± 0.020	-5.891 ± 0.035	1.132 ± 0.007	1.132 ± 0.006
9	-7.470 ± 0.016	-6.801 ± 0.030	1.098 ± 0.005	1.117 ± 0.004
10	-6.624 ± 0.020	-5.904 ± 0.035	1.122 ± 0.007	1.123 ± 0.006

Table 3.10: Results for $\langle A_p^T \rangle$, $\langle A_p^R \rangle$, and R_c for each mirror, with and without PMT cut. The errors are due to the statistics of determining the means of A_p^T and A_p^R from the histograms in Figure 3.13.

been applied. The results are very symmetric about the detector; that is mirrors 1, 3, 8, and 10 have the same values, as do 2 and 9, 4 and 7, and 5 and 6. This indicates that there are no gross geometry errors in the simulation.

The comparison between R_c for the PMT and no PMT cut cases is important because the mirror shapes in the simulation geometry are just an approximation to the real shapes. The actual mirrors are sections of ellipsoids whereas the simulated mirrors are sections of spheres. The agreement should be good near the center of the mirror, but there could be a discrepancy near the edges resulting in reflected trajectories not being focussed correctly. With the exception of mirrors 2 and 9 and 5 and 6 R_c for the two cases agrees to better than a percent. Mirrors 5 and 6 without the PMT cut are 3% higher than the cut case; and mirrors 2 and 9 are 1.5% higher. Table 3.9 shows that mirrors 2, 5, 6, and 9 have the fewest

Mirrors	R_c(full acceptance)	R_c(central angle)	R_c(PRL)
1, 3, 8, 10	1.130 ± 0.004	1.058 ± 0.007	1.082
2, 9	1.100 ± 0.004	1.061 ± 0.006	1.068
4, 7	1.140 ± 0.006	1.070 ± 0.007	1.103
5, 6	1.077 ± 0.004	1.056 ± 0.007	1.059

Table 3.11: Final results for R_c averaged over mirror type. The error is due to the statistics of determining the mean of A_p^T and A_p^R. The third column shows R_c in the case in which scattered electrons are constrained to a few degrees about the central angle of mirrors 1, 2, 4, and 5. The final column shows the values of R_c that were used to extract A_p in Ref. [Spa00].

number of events cut in the unradiated case, less than 1%. However, they lose a similar percentage of events to the cut as the other six mirrors in the radiated case. A relative systematic error of 2% is applied to R_c due to the effects of the PMT cut.

The final R_c used to calculate A_p are found by averaging over the results in Table 3.10 for each of the four mirror types (mirrors with the same average Q^2, see Table 2.2) with the PMT cut applied. This removes any effects due to strange geometry in the simulation and improves the statistical error on R_c. These results are tabulated in Table 3.11. The second column of this table shows R_c from constraining the scattered electrons to a few degrees about the central angle of each mirror (Table 2.2). Comparing these results with R_c over the full mirror acceptance indicates the degree to which geometry is important in this calculation. The final column lists the values used to extract A_p in Ref. [Spa00]. These numbers are in good agreement with the R_c calculated at the center of the mirrors, but are significantly smaller than the values over the full mirror.

Source	Relative Error (%)
PMT Cut	2.0
Elastic Window ΔE	2.0
Theoretical Approximations	1.0
Statistics	0.5
Total	3.0

Table 3.12: Table of systematic errors applied to R_c. The total value is found by adding the individual contributions in quadrature.

Mo and Tsai state that the approximations used to calculate the radiative tail due to bremsstrahlung are only good to 30% when $E_p \lesssim 0.5 E_p^M$ [MT69]. The systematic error due to this approximation was gauged by placing a cut such that all events with scattered energy less than 70 MeV were excluded from the calculation. This resulted in an average increase of 3% in A_p^R for each mirror; an additional relative systematic error of $30\% \times 3\% = 1\%$ was applied to R_c. Another possible source of systematic error on this calculation is due to the size of the window ΔE used to determine the elastic peak. The elastic window was chosen to be 1 MeV for this analysis, but an increase to 5 MeV resulted in a 2% increase in R_c. A 2% contribution to the systematic error was included for ΔE. The statistical errors on the determination of R_c in Table 3.10 contribute a relative systematic error of 0.5% to R_c. The total relative systematic error on R_c was found to be 3% by adding the individual contributions together in quadrature. Table 3.12 lists the relative contributions to the systematic error.

3.4 Additive Factors

In addition to the dilution factors of the previous section there are a number of additive factors that could affect the final physics asymmetry. These factors, if non-negligible, must be subtracted from the measured, undiluted asymmetry according to equation 3.13. Each of the possible additive factors will be discussed in the following sections.

3.4.1 Closed Shutter Asymmetry

A non-zero asymmetry in runs where the shutters are closed can result if there is some helicity dependent background in the experiment. Since the closed shutter signal is a portion of the total signal measured in the experiment this false asymmetry has to be removed. However, it is not simply a matter of subtracting the measured closed shutter asymmetry because of the dilution factors. The appropriate correction factor $K_C(m,n)$ is found in equation 3.14.

The contribution of the closed shutter asymmetry to A_p is a factor $(1-f_l) \approx 0.2$ of the open shutter contribution. For example, in order to constitute a 10% correction to A_p, A_C^C must be of order half a ppm. Table 3.13 displays the average uncorrected and corrected shutter closed asymmetry for each mirror, divided by the beam polarization. As the table indicates the asymmetries are certainly large enough to impact the determination of A_p, but the error bars are quite large as well. This correction is addressed in Section 4.1.1.

Mirror	$\frac{A_C^U}{P_B}$ (ppm)	$\frac{A_C^C}{P_B}$ (ppm)
1	13.48 ± 8.28	12.67 ± 8.28
2	15.53 ± 8.61	14.75 ± 8.61
3	-8.44 ± 8.71	-9.15 ± 8.71
4	-32.10 ± 9.21	-32.54 ± 9.21
5	1.64 ± 7.32	0.85 ± 7.32
6	-15.56 ± 7.16	-16.11 ± 7.16
7	-22.71 ± 8.75	-23.12 ± 8.75
8	8.13 ± 8.20	7.36 ± 8.20
9	13.05 ± 7.90	11.98 ± 7.90
10	2.77 ± 7.76	2.14 ± 7.76

Table 3.13: This table lists the uncorrected and corrected asymmetries, divided by beam polarization, for each mirror with the shutters closed. The correction for each mirror is of order one ppm.

3.4.2 Pion Fraction

The SAMPLE kinematics are such that it is possible to produce positive (π^+) and neutral (π^0) pions via photoproduction or electroproduction:

$$\gamma + p \rightarrow \begin{cases} \pi^0 + p \\ \pi^+ + n \end{cases} \qquad e + p \rightarrow \begin{cases} e + \pi^0 + p \\ e + \pi^+ + n. \end{cases}$$

The pions are not detected directly, but their decay products are. Many of the π^+ that are produced are stopped in the target and decay into positive muons (μ^+) and muon neutrinos (ν_μ). The muons decay into positrons (e^+) and more neutrinos. Sometimes the positron has enough energy to generate Čerenkov photons in the detector and thus be detected in the PMTs. The neutral pions decay into a pair of photons which can generate electrons in the target and the cryostat. These electrons also have enough energy to generate Čerenkov photons.

This contribution is potentially important because it has a cross section asym-

metry A_π that depends on the spin of the electron. If A_π is sufficiently large and pions form a large enough portion of the total signal, then a false asymmetry can be induced in A_p. While no data exist for the parity violating asymmetry due to threshold pion production, Li, Henley, and Hwang calculated A_π for photo- and electroproduced positive and neutral pions in 1982 [LHH82]. They found that the photoproduction asymmetry was of order 10^{-7}, as was the electroproduction asymmetry at the Q^2 appropriate for the SAMPLE kinematics* of 0.001 $(\mathrm{GeV/c})^2$. A decade later Hammer and Drechsel recalculated the electroproduction asymmetry and found a similar result, $A_\pi \approx -10^{-4}\frac{Q^2}{(\mathrm{GeV/c})^2} = -10^{-7}$ [HD95]. Most recently, Chen and Ji calculated A_π specifically for π^+ photoproduction near threshold using heavy baryon chiral perturbation theory and found that $|A_\pi| \leq 2.5 \times 10^{-7}$† [CJ01b]. A similar calculation of π^+ electroproduction at threshold resulted in $|A_\pi| < 2 \times 10^{-7}$ [CJ01a]. Assuming that A_π is the same for π^+ and π^0 and given that A_π is approximately the same for the two production processes in the most recent calculations, then an upper limit of 2.5×10^{-7} can be placed on $|A_\pi|$.

The fraction of the elastic signal due to π^+ can be extracted from the pulse

*The momentum transfer for electroproduction is significantly different than the elastic $\vec{e}$-p Q^2 of 0.1 $(\mathrm{GeV/c})^2$. The maximum energy of the scattered electrons in pion electroproduction is approximately 50 MeV for an incident energy of 200 MeV and the electrons are forward peaked [CJ01a]. This leads to $Q^2 = 4EE' \sin^2\frac{\theta}{2} \sim 0.001$ $(\mathrm{GeV/c})^2$.

†This is assuming a value of $h^{(1)}_{\pi NN} = 5 \times 10^{-7}$.

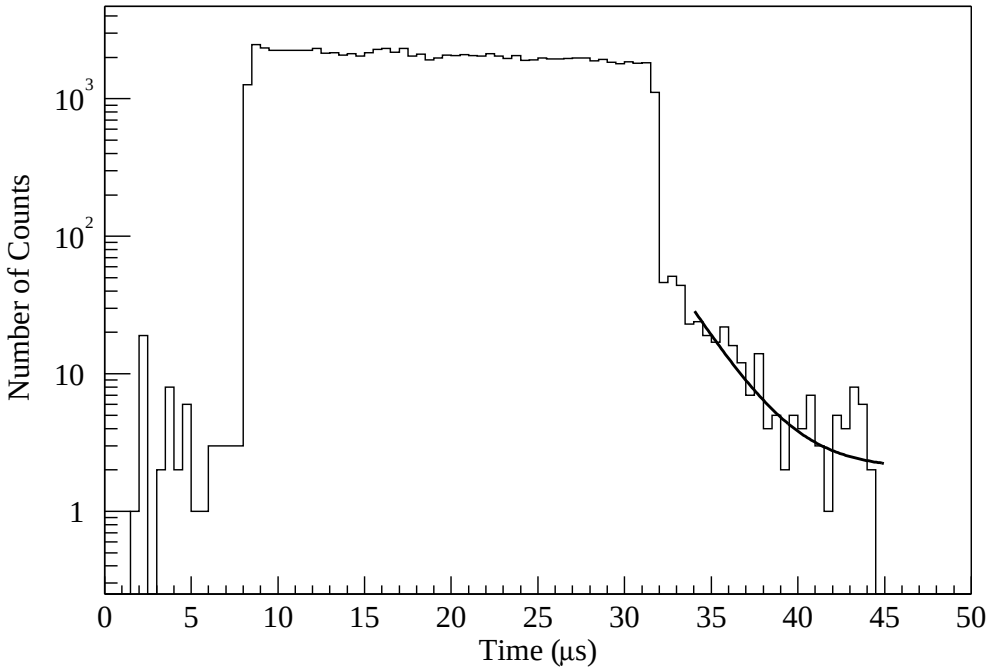

Figure 3.14: Arrival time, starting with the beginning of the pulse counting time window, of coincidence events. The flat part of the spectra reflects the period of time when the electron beam is on. The exponentially decaying event rate beyond 32 μs is attributed to pion decay products. The black line is a fit to data of equation 3.74.

counting data. Figure 3.14 shows the arrival time spectrum of coincidence events. The period of time when electrons are striking the target is obvious, as is a small exponential decay after the electrons have stopped arriving. This tail is due to the arrival of positrons from the decay of pions that have been generated by the electron beam. The π^+ contribution can be determined by fitting the tail to a function of the form

$$P(t) = A + Be^{-\frac{(t-t_0)}{\tau_{\pi^+}}} \tag{3.74}$$

where t is the arrival time of the coincidence event, t_0 is the time when the beam pulse ends, $\tau_{\pi^+} = 2.2$ μs is the lifetime of the π^+, and A and B are allowed to vary. Taking the ratio of B to the average number of counts per bin in the last few bins of the electron arrival time period yields the pion fraction due to positive pions f_{π^+} [Bei00]. Only the average of the last few bins is used because of the DAQ dead time effect discussed in Section 3.3.3.

The result for f_{π^+} was found to be 3.2% [Bei00]. According to a GEANT simulation performed by Mueller the π^0 contribution to the elastic yield is $\frac{1}{3}$ of the π^+ contribution, therefore $f_\pi = \frac{4}{3} f_{\pi^+} = 4.3\%$ [Mue97b]. This result is in good agreement with the value for f_π Mueller extracted from the 1995-96 data set of $(4.2 \pm 2.5)\%$. The error on Mueller's result comes from the GEANT simulation, therefore that error is applied to the present result, as well, leading to $f_\pi = (4.3 \pm 2.5)\%$.

The contribution of A_π to A_p was extracted in equation 3.13. The quantity $K_\pi \approx 0.03$ ppm, therefore it can be safely ignored. The pion asymmetry contributes a completely negligible amount to the measured asymmetry, but the pion fraction does constitute an important dilution factor. Its inclusion in equation 3.13 increases A_p by almost 5%.

3.4.3 Mott Asymmetry

As discussed in Section 2.7.2 there is a parity conserving, helicity dependent asymmetry that can constitute a false asymmetry in the measurement. Equation 2.19 showed that the false asymmetry is proportional to the Mott asymmetry, the amount of residual transverse polarization in the experiment, and the degree to which the detector is asymmetric. The residual transverse polarization for SAMPLE was determined in Section 3.3.1 and found to be $\left|\frac{P_B^T}{P_B}\right| = (1.74 \pm 0.72)\%$. The degree of detector asymmetry has not been measured, but it has been calculated that if one half of one mirror were completely non-reflective then the resultant detector asymmetry would be approximately 5% [Mue97b]. This is a very conservative estimate, there is no reason to believe that the detector asymmetry is this large.

Approximately 40 hours of integration mode data were taken with the beam polarization set transverse to the beam momentum. Half of these data were taken with the polarization in the bend plane and half perpendicular to the bend plane. In both states data were taken with the helicity reversal plate in and out. This resulted in a relatively low statistics data sample, but it was enough to determine the Mott asymmetry A_T to approximately $\pm 33\%$.

The raw asymmetry for each mirror was corrected for the beam polarization, elastic fraction, light fraction, and radiative correction as appropriate and then the average asymmetry for each mirror for a given setting of the transverse po-

Φ	Helicity Plate	A_T (ppm)	δ (degrees)	χ^2_ν
0	In	12.9 ± 9.8	173.8 ± 39.5	1.30
0	Out	13.8 ± 9.9	16.9 ± 39.5	1.50
90	In	18.4 ± 11.8	-84.1 ± 39.8	0.30
90	Out	18.1 ± 11.7	127.2 ± 38.0	2.07

Table 3.14: A table of Mott asymmetry magnitudes and phases for each of the four settings of transverse beam polarization Φ and helicity reversal plate determined from fitting to equation 3.75 [Wel01]. The reduced chi-squared χ^2_ν for the fit is shown as well. When $\Phi = 0$ and the reversal plate is IN positively polarized electrons point along the direction the beam bends to get into the North Hall.

larization and helicity reversal plate was calculated. The ten mirror asymmetries for each setting were fit to a function of the following form [Wel01]:

$$A(\phi) = A_T \sin(\phi + \delta) \tag{3.75}$$

where $A(\phi)$ is the average measured asymmetry for the mirror at azimuthal angle ϕ (Table 2.2). The phase δ and magnitude A_T were allowed to vary, the results are shown in Table 3.14. The direction of beam polarization is denoted by Φ. When $\Phi = 0$ and the helicity plate is in, positively polarized electrons point along the direction the beam bends to get into the North Hall. When $\Phi = 90°$ and the helicity plate is in, positively polarized electrons point down. The total Mott asymmetry is found by averaging the individual A_T in Table 3.14, while accounting for the phases appropriately. The final result is $A_T = -15.4 \pm 5.4$ ppm [Wel01].

The results for A_T can be used to put an upper limit on the false asymmetry A_F due to transverse beam polarization during longitudinal running according

to equation 2.19. Assuming a detector asymmetry F_S of 5% $|K_T| \leq 0.01$ ppm which is a negligible contribution compared to the statistical error on A_p.

3.5 Summary

This chapter has dealt with the details of extracting A_p from $A^U_{O(C)}$. The first step was to correct the raw asymmetry for helicity correlated beam parameter differences. It was determined from corrections to luminosity monitor asymmetries that the corrections procedure was effective, but the actual corrections to mirror asymmetries were very small. The combination of the various dilution factors R_c, P_B, f_e, f_l, and f_π increases the corrected asymmetry by a factor of approximately 4-5. The effects of the pion asymmetry and the transverse beam polarization asymmetry were found to be negligible, but the same may not be true of the closed shutter asymmetry. In the final chapter all of these results will be combined in order to determine G^s_M.

Chapter 4

Results and Conclusions

4.1 Results

The experimental results of the previous chapter can now be combined with the theoretical results of Chapter 1 in order to extract G_M^s and $G_A^e(T=1)$. In the first section the final value of A_p is determined and the result for A_d is quoted in order to fix G_M^s and $G_A^e(T=1)$. In Section 4.2 the results are compared to the theoretical predictions of Section 1.3. The status of other experiments with the same experimental goals is the subject of Section 4.3.

4.1.1 Asymmetry from Hydrogen

In Chapter 3 the open and closed corrected asymmetries for each mirror $A_{O(C)}^C(m)$ were extracted, as were the various dilution factors P_B, f_e, f_l, f_π, and R_c. These quantities must be combined according to equation 3.13 in order to extract the

Mirror	K_O (ppm)	K_C (ppm)	A_p (ppm)
1	-6.09 ± 1.97	3.02 ± 1.97	$-9.11 \pm 1.97 \pm 1.97$
2	-2.70 ± 2.29	4.41 ± 2.57	$-7.11 \pm 2.29 \pm 2.57$
3	-6.98 ± 2.00	-2.13 ± 2.03	$-4.85 \pm 2.00 \pm 2.03$
4	-5.54 ± 1.83	-6.72 ± 1.90	$1.18 \pm 1.83 \pm 1.90$
5	-12.42 ± 3.20	0.57 ± 4.89	$-12.99 \pm 3.20 \pm 4.89$
6	-12.27 ± 3.13	-10.93 ± 4.86	$-1.33 \pm 3.13 \pm 4.86$
7	-2.49 ± 2.07	-5.61 ± 2.12	$3.12 \pm 2.07 \pm 2.12$
8	-3.82 ± 2.02	1.75 ± 1.95	$-5.57 \pm 2.02 \pm 1.95$
9	-5.39 ± 2.03	3.25 ± 2.14	$-8.64 \pm 2.03 \pm 2.14$
10	-6.02 ± 1.75	0.46 ± 1.66	$-6.47 \pm 1.75 \pm 1.66$
Average	-5.67 ± 0.67	-0.62 ± 0.69	$-4.81 \pm 0.67 \pm 0.69$

Table 4.1: A table of results for each mirror extracted from the data in Chapter 3 and equation 3.13. The first column is the open shutter contribution to A_p, the second column is the closed shutter contribution K_C, and the third column is A_p. The error in the first (second) columns is due to the statistics of determining $A^C_{O(C)}$. The error on K_C is considered a systematic error on A_p and is the second error in the third column. The final row is the weighted average of each column over all mirrors.

proton asymmetry for each mirror $A_p(m)$. The first column of Table 4.1 shows the results for the first term of equation 3.13, the contribution K_O from the open shutter asymmetry:

$$K_O = \frac{R_c}{f_l f_e (1 - f_\pi)} \frac{A^C_O}{P_B}. \tag{4.1}$$

The error on these results is due to the statistics of determining A^C_O. The second column lists the closed shutter contribution K_C with the statistical error due to the measurement of A^C_C. As discussed in Sections 3.4.2 and 3.4.3 the pion and transverse polarization asymmetry contributions K_π and K_T are negligibly small and taken to be zero. A_p, the difference between K_O and K_C, is tabulated in the final column. The error due to K_C is considered a systematic error on the

Mirror	θ (degrees)	A_p (ppm)
4, 7	138.4	-4.96
1, 3, 8, 10	145.9	-5.56
2, 9	154.0	-6.14
5, 6	160.5	-6.53

Table 4.2: Theoretical values of A_p calculated at the central angle of each mirror using equation 1.65. The values of G_M^s and $G_A^e(T=1)$ extracted in Section 4.1.3 of this work were used in this calculation: $G_M^s = 0.06$ and $G_A^e(T=1) = -0.03$.

determination of A_p and is listed separately from the statistical error due to K_O. The final row of Table 4.1 is the average of the values for each mirror weighted by the error on each quantity.

When averaged over all mirrors the closed shutter contribution is consistent with zero, $K_C = -0.62 \pm 0.69$ ppm. This is the expected result since the closed shutter signal is due to background processes which should not possess a parity violating asymmetry. However, the reduced chi-squared χ^2_ν for this average is rather poor, 3.700, corresponding to a probability of 0.01% for nine degrees of freedom. The average K_O has a χ^2_ν of 1.206, possible at the 28% level for 10 degrees of freedom, but for A_p the $\chi^2_\nu = 1.752$ which is only 6% probable. Presumably the poor value of χ^2_ν for A_p is due to the behavior of K_C. The values of χ^2_ν for K_O and A_p were calculated using the theoretical values for A_p at the central angle of each mirror; the theoretical values of A_p are tabulated in Table 4.2. The experimentally extracted values of $G_M^s = 0.06$ and $G_A^e(T=1) = -0.03$ from Section 4.1.3 were used in the calculation of A_p.

In Figure 4.1 the data for K_C have been plotted as a function of azimuthal

scattering angle ϕ. The closed shutter data appear to have a significant ϕ dependence; the data were fit to a function of the following form:

$$f(\phi) = A_0 + F\cos(2\phi + \phi_0) \tag{4.2}$$

where A_0, F, and ϕ_0 were allowed to vary. The data were also fit to a flat line:

$$f(\phi) = A_0. \tag{4.3}$$

The results of these fits are shown in Figure 4.1 and tabulated in Table 4.3. As expected, the fit to equation 4.3 is in perfect agreement with the average value in Table 4.1. The closed shutter data are described much better by equation 4.2 ($\chi^2_\nu = 1.15$ with 33% probability) than by a flat line. The constant term A_0 of the three parameter fit is in better agreement with zero, as well.

In Figure 4.2 the data on K_O from Table 4.1 is plotted as a function of ϕ. These data do not show any strong ϕ dependence aside from that due to the variation in scattering angle θ as a function of ϕ. A better value of χ^2_ν is obtained for the weighted average (equation 4.3) than for the three parameter fit (equation 4.2). The constant term A_0 is similar for the two different K_O fits.

Given the ϕ dependence of the closed shutter data and the constraints of equation 3.13 the best value for A_p is given by subtracting the constant term of the three parameter fit to K_C from the weighted average of K_O, $A_p = (-5.67 \pm 0.67) - (-0.06 \pm 0.71)$ ppm. The statistical error on K_C is treated as a systematic error on A_p. Contributions to the systematic error on A_p due to the corrections

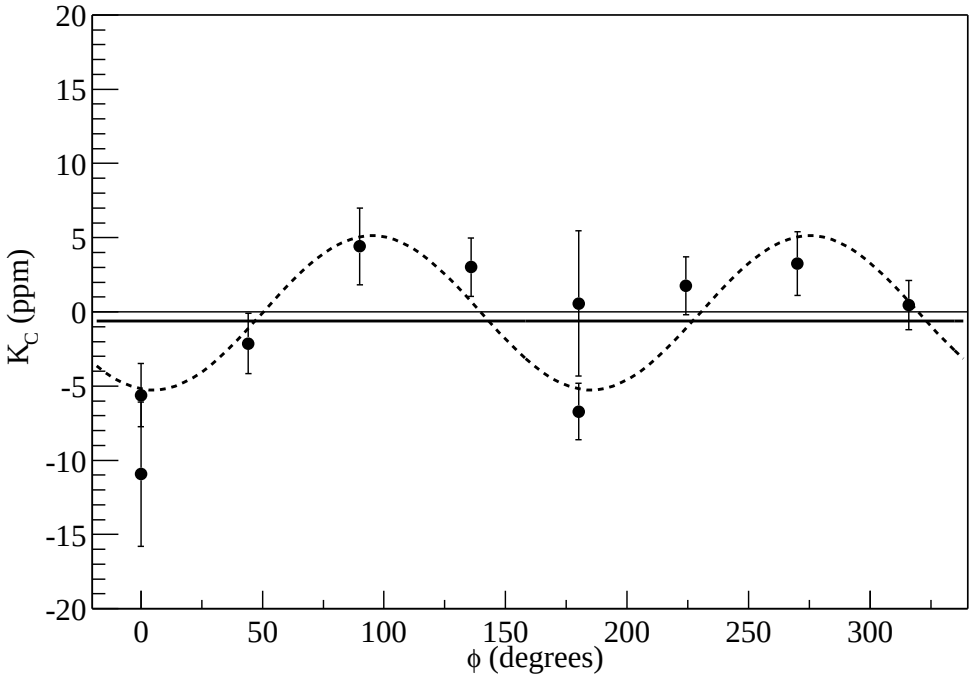

Figure 4.1: The closed shutter contribution (K_C) to A_p as a function of azimuthal scattering angle ϕ. There are two mirrors at different polar scattering angles θ for $\phi = 0°$ and $\phi = 180°$. The solid (dashed) line is the fit of equation 4.3 (4.2) to K_C. Fit results are listed in Table 4.3.

Fit	A_0 (ppm)	F (ppm)	ϕ_0 (°)	χ^2	ν	P
K_O (4.3)	-5.67 ± 0.67			12.06	10	0.2811
K_O (4.2)	-5.50 ± 0.68	1.11 ± 0.95	-162.4 ± 48.8	12.95	7	0.0733
K_C (4.3)	-0.62 ± 0.69			33.30	9	0.0001
K_C (4.2)	-0.06 ± 0.71	5.20 ± 1.04	-190.1 ± 10.5	8.06	7	0.3273

Table 4.3: This table contains the results of fits of equations 4.3 and 4.2 to the data in Table 4.1. The values of χ^2, number of degrees of freedom ν, and probability P are listed for each fit as well. The value of χ^2 listed for the fit of K_O to equation 4.3 is calculated using the values of A_p listed in Table 4.2.

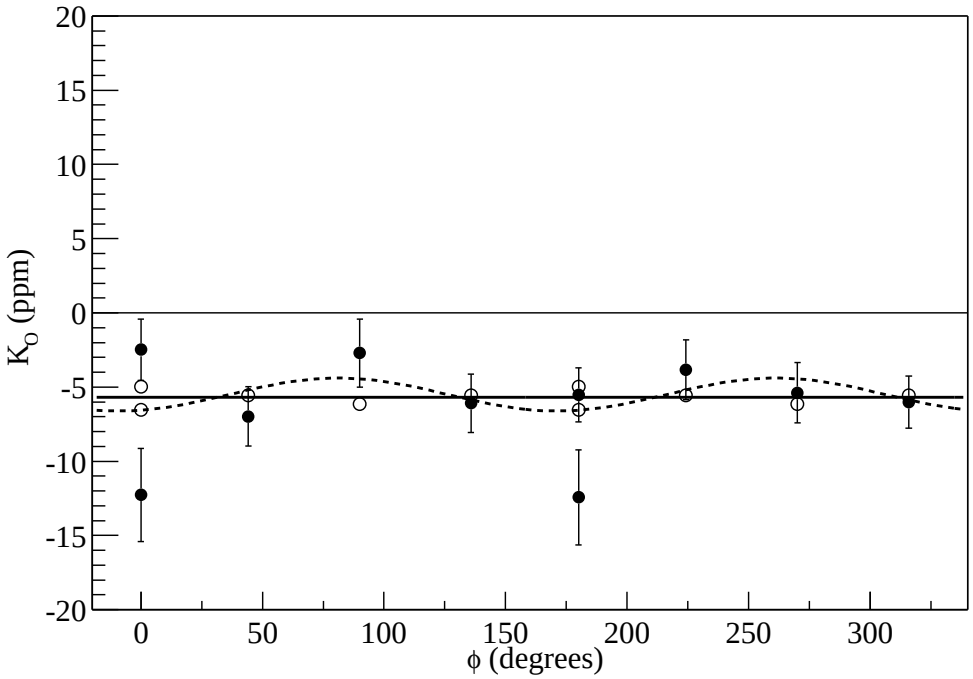

Figure 4.2: The open shutter contribution (K_O) to A_p as a function of azimuthal scattering angle ϕ. Data points are given by closed circles and theoretical values of A_p from Table 4.2 are given by open circles. There are two mirrors at different polar scattering angles θ for $\phi = 0°$ and $\phi = 180°$. The solid (dashed) line is the fit of equation 4.3 (4.2) to K_O. Fit results are listed in Table 4.3.

procedure, dilution factors, and K_C are summarized in Table 4.4.

The final result for the elastic $\vec{e}$-p scattering asymmetry is

$$A_p(Q^2 = 0.1(\mathrm{GeV/c})^2) = -5.61 \pm 0.67 \pm 0.88 \text{ ppm}. \tag{4.4}$$

This should be compared with the previously published value of A_p for this same data set, $A_p = -4.92 \pm 0.61 \pm 0.73$ ppm [Spa00]. The published value of A_p assumes that $K_C = 0$, but assigns a systematic error to the open shutter contribution from each mirror to account for the behavior of the shutter closed asym-

Source	Relative Error (%)
Beam Parameter Correction	$\delta A_O^C/A_O^C = 6.0$
Beam Polarization	$\delta P_B/P_B = 4.2$
EM Radiative Correction	$\delta R_c/R_c = 3.0$
Elastic Fraction	$\delta f_e/f_e = 4.0$
Pion Fraction	$\delta f_\pi/(1-f_\pi) = 2.4$
Closed Shutter Asymmetry	$\delta K_C/A_p = 12.7$
Total	$\delta A_p(\text{syst.})/A_p = 15.7$

Table 4.4: Table of systematic errors applied to A_p. The total error is found by adding the contributions together in quadrature.

metry data. As shown in Table 3.11, the values of R_c used to extract that result were $(4 \pm 4)\%$ lower on average than the results employed in this work. Also, no correction was made to that result to account for the fraction of the signal due to pions, a $(4.5 \pm 2.5)\%$ effect. If the PRL result is inflated by these two factors there is good agreement with the result of this work ($-5.35 \pm 0.66 \pm 0.79$ ppm). The discrepancy in the systematic error is due to the different methods of handling the contribution of the closed shutter data.

4.1.2 Asymmetry from Deuterium

In the summer of 1999 the SAMPLE collaboration performed an experiment to measure A_d by scattering polarized electrons from a target of liquid deuterium [Has00a]. The same apparatus was used to perform the deuterium experiment with two minor modifications. The deuterium measurement required the installation of some gas recovery tanks to contain the deuterium in the event of a target boil off. Additional neutron shielding, in the form of sheets of borated

polyethylene, was installed around and between the target and the Čerenkov photomultiplier tubes.

The experimental procedure for the deuterium measurement was the same as for the hydrogen measurement, as were the details of extracting the physics asymmetry from the measured asymmetry; however, there are some nuclear effects in the deuteron experiment that must be accounted for. The deuteron asymmetry after the helicity correlated parameter difference corrections and dilution factors have been applied, but before corrections due to nuclear effects, is denoted A_d^M. After averaging over all mirrors the measured deuteron asymmetry is $A_d^M = -6.89 \pm 0.64 \pm 0.55$ ppm, representing 133 Coulombs of electrons delivered to the SAMPLE target. [Has00a, Pit01].

The nuclear effects that must be accounted for are threshold disintegration of the deuteron and elastic scattering from the deuteron as a whole. Both of these processes exhibit a parity violating asymmetry that can obscure the quasielastic parity violating asymmetry. The measured deuteron asymmetry is related to the three parity violating asymmetries via the following relation:

$$A_d^M = \frac{A_d^{QE}\sigma_{QE} + A_d^E\sigma_E + A_d^{TD}\sigma_{TD}}{\sigma_{QE} + \sigma_E + \sigma_{TD}} \tag{4.5}$$

where $\sigma_{QE/E/TD}$ is the quasielastic/elastic/threshold disintegration cross section and $A_d^{QE/E/TD}$ is the quasielastic/elastic/threshold disintegration parity violating asymmetry.

There have been theoretical calculations of the elastic and threshold disinte-

gration asymmetries. A calculation by Pollock determined the elastic deuteron asymmetry [Pol90]:

$$A_d^E = \frac{G_F Q^2}{4\pi\alpha\sqrt{2}} \left(4\sin^2\theta_W + \frac{2G_M^s}{\mu_d} F_T \right) \tag{4.6}$$

where μ_d is the deuteron's magnetic moment and F_T is the fraction of the elastic cross section due to magnetic scattering. For the SAMPLE kinematics, $\frac{2F_T}{\mu_d}$ is approximately 0.87. Using the original SAMPLE result of 0.23 for G_M^s from Ref. [Mue97a] yields $A_d^E = 10.3$ ppm. Musolf and Donnelly calculated the PV asymmetry for threshold electrodisintegration assuming that the M1 transition from the deuteron ground state ${}^3S_1(T=0)$ to the lowest lying ${}^1S_0(T=1)$ excited state is the dominant transition [MD92]:

$$\begin{aligned} A_d^{TD} = &- \frac{G_F Q^2}{\pi\alpha\sqrt{2}} \times \\ &\left[\left(\frac{1}{2} - \sin^2\theta_W \right) + \frac{v_T'}{v_T} (1 - 4\sin^2\theta_W) \left(\frac{M_N}{q} \right) \left(\frac{G_A^e(T=1)}{2G_M^{T=1}} \right) \right] \end{aligned} \tag{4.7}$$

where v_T and v_T' are kinematic factors. It is found to have the value -12.8 ppm assuming the theoretical value of $G_A^e(T=1)$ from Ref. [MH90].

The quasielastic cross section is 47 nb/sr and the elastic cross section is 1 nb/sr at the kinematics of the SAMPLE experiment. The threshold disintegration cross section is extrapolated from data taken by Simon *et al.* [Sim79]. The measured cross section is found to be fairly constant over a 10 MeV window near threshold; integrating over this window results in a value of $\sigma_{TD} = 4$ nb/sr. The quasielastic deuteron asymmetry after applying equation 4.5 is $A_d = A_d^{QE} = -6.79 \pm 0.64 \pm 0.55$ ppm [Has00a].

This result does not include a correction for the closed shutter contribution K_C, which was consistent with zero and well described by a distribution constant in ϕ. There was no correction for the fraction of the Čerenkov signal due to pions, f_π. The fraction due to charged pions* was measured to be $f_{\pi^\pm} = (1.6 \pm 0.2)\%$ [Has00b]. The production rate of π^0 relative to $\pi^\pm$ is unknown, but the pion fraction due to π^0 is assumed to be 1%, the same as in the hydrogen case, leading to $f_\pi = f_{\pi^\pm} + f_{\pi^0} = 2.6\%$. The electromagnetic radiative corrections used to extract A_d^M came from the same code used to calculate R_c(PRL) in Table 3.11. The new values of R_c in that table are approximately 4% higher than R_c(PRL); it is assumed that a new calculation of the deuterium R_c will result in a 4% increase as well. To account for the measured pion fraction and the improved calculation of R_c the following correction was applied to A_d^M:

$$A_d^M \rightarrow \lambda A_d^M \tag{4.8}$$

$$\lambda = \frac{(1.04)}{(1 - 0.026)} = 1.07 \tag{4.9}$$

with an additional 7% systematic error. The new value for A_d^M is

$$A_d^M(Q^2 = 0.1(\mathrm{GeV/c})^2) = -7.37 \pm 0.68 \pm 0.75 \text{ ppm}, \tag{4.10}$$

resulting in a quasielastic $\vec{e}$-d scattering asymmetry of

$$A_d(Q^2 = 0.1(\mathrm{GeV/c})^2) = -7.28 \pm 0.68 \pm 0.75 \text{ ppm}. \tag{4.11}$$

*Positively and negatively charged pions can be generated by scattering from the deuteron.

4.1.3 G_M^s and $G_A^e(T=1)$

Equations 1.65 and 1.71 can now be combined with the experimental measurements of A_p and A_d to extract G_M^s and $G_A^e(T=1)$. In order to accomplish this the theoretical expressions for the proton and deuteron asymmetries were evaluated at the central angle of each mirror as given in Table 2.2*. The four equations for A_p (one for each value of θ) and for A_d were averaged together using the statistical error on the measurement of the asymmetry for each mirror as a weighting factor. The result was the following pair of equations:

$$A_p = [-5.78 + 1.60 G_A^e(T=1) + 3.52 G_M^s] \text{ ppm} \tag{4.12}$$

$$A_d = [-7.27 + 1.78 G_A^e(T=1) + 0.75 G_M^s] \text{ ppm}. \tag{4.13}$$

The equation for A_d is from Ref. [Has00a].

After solving this pair of equations for G_M^s and $G_A^e(T=1)$ the measured values of A_p and A_d were used to extract these results:

$$G_M^s \left(Q^2 = 0.1(\text{GeV/c})^2\right) = 0.06 \pm 0.32 \pm 0.39 \pm 0.03 \tag{4.14}$$

$$G_A^e(T=1) \left(Q^2 = 0.1(\text{GeV/c})^2\right) = -0.03 \pm 0.48 \pm 0.54 \pm 0.12 \tag{4.15}$$

The last error on each result is due to the uncertainty in the EM form factors and $G_A^e(T=0)$. These errors were arrived at by systematically varying each form factor, calculating new values of the coefficients in equations 4.12 and 4.13, and

*The deuteron asymmetry must be averaged over the quasielastic peak resulting in a slight reduction in the theoretical asymmetry.

determining the new values for G_M^s and $G_A^e(T=1)$. Based on these studies it was discovered that only the uncertainties in $G_m^{\gamma n}$ and $G_A^e(T=0)$ contributed significantly to G_M^s and $G_A^e(T=0)$. The error on $G_A^e(T=1)$ contains a contribution of 0.05 from $G_M^{\gamma n}$ and 0.11 from $G_A^e(T=0)$; G_M^n is the only form factor that contributes to the error on G_M^s.

These values for G_M^s and $G_A^e(T=1)$ should be compared with the results from Ref. [Has00a]:

$$G_M^s\left(Q^2 = 0.1(\mathrm{GeV/c})^2\right) = 0.14 \pm 0.29 \pm 0.31 \tag{4.16}$$

$$G_A^e(T=1)\left(Q^2 = 0.1(\mathrm{GeV/c})^2\right) = 0.22 \pm 0.45 \pm 0.39. \tag{4.17}$$

The reasons for the differences between the results derived in this work and the results of Ref. [Has00a] were discussed in Sections 4.1.1 and 4.1.2. A new calculation of the electromagnetic radiative corrections R_c and a correction for the pion fraction are the primary reasons for the change in the values of G_M^s and G_A^e. The different treatment of the shutter closed asymmetry in the proton measurement and an assessment of the EM form factor dependence accounts for the residual discrepancy in the systematic error.

4.2 Comparison with Predictions

4.2.1 G_M^s

The predictions for G_M^s discussed in Section 1.3.1 were performed at the $Q^2 = 0$ limit, $\mu_s \equiv G_M^s(Q^2 = 0)$. In order to compare the experimental result with theory it is necessary to either extrapolate the experimental result to $Q^2 = 0$ $(\mathrm{GeV/c})^2$ or the theoretical predictions to $Q^2 = 0.1$ $(\mathrm{GeV/c})^2$. The results from HBχPT discussed in Section 1.3.1 provide a means for extrapolating G_M^s at a finite Q^2 back to μ_s. The authors of that paper extrapolated the first published SAMPLE result of $G_M^s(Q^2 = 0.1(\mathrm{GeV/c})^2) = 0.23 \pm 0.37 \pm 0.15 \pm 0.19$ to a range for μ_s of 0.03 – 0.18 n.m. [Mue97a, HMS98]. To extract μ_s from the new result the difference between the published result and and the average theoretical μ_s is subtracted from equation 4.14 and a theoretical error bar corresponding to the above range is applied:

$$\mu_s = -0.06 \pm 0.32 \pm 0.39 \pm 0.07 \text{ n.m.} \tag{4.18}$$

The systematic error due to the measurements of A_p and A_d have been combined in quadrature with the error due to the uncertainty in the form factors in this result.

Figure 4.3 is a graph of the theoretical predictions for μ_s tabulated in Table 1.4. A band corresponding to the measured value of μ_s has been overlaid on this plot. It is clear from this figure that the measured value is in good agreement with

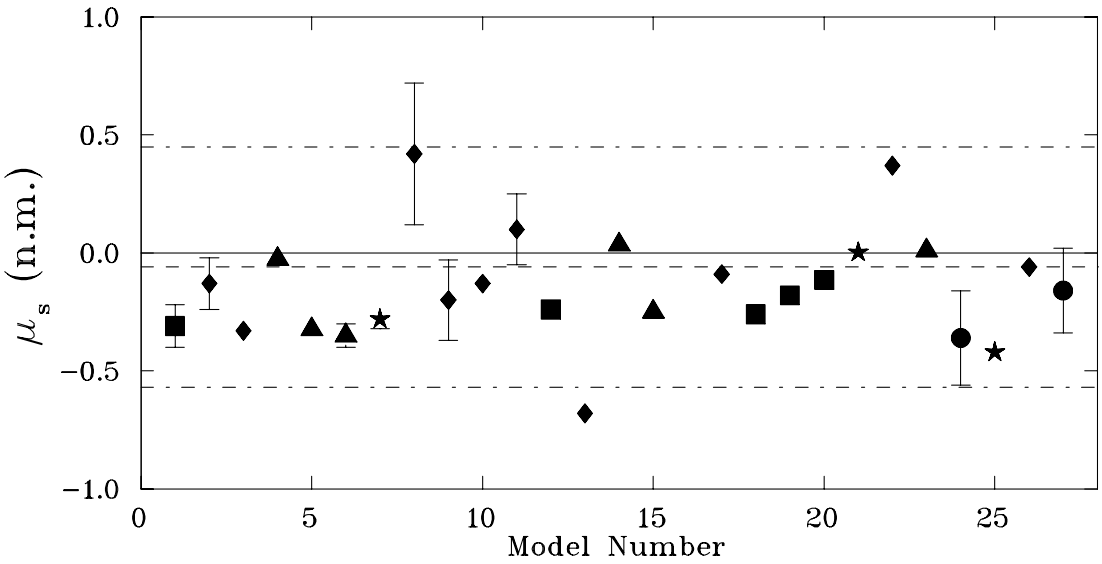

Figure 4.3: A graph of various model predictions for $\mu_s \equiv G_M^s(Q^2 = 0)$. Squares are poles model predictions, triangles are loops model predictions, stars are loops and poles model predictions, diamonds are predictions from other models, and circles are lattice QCD predictions. See Table 1.4 for the models and values of particular data points. The dashed line corresponds to the result for μ_s presented in this work. The dotted-dashed lines are the statistical, systematic, and theoretical errors added in quadrature.

all of the theoretical predictions. There is not enough resolution in the experiment nor enough discrepancy between predictions to make definitive remarks about the validity of the models. More data are necessary to further constrain μ_s.

4.2.2 $G_A^e(T = 1)$

The lone theoretical prediction for $G_A^e(T = 1)$, -0.83 ± 0.26, is roughly 1σ away from the experimental result, as can be seen in Figure 4.4 [Zhu00]. The experimental result indicates that there is a strong cancellation between the tree level Z exchange diagrams and the higher order radiative correction diagrams, $R_A^1 \approx -1$

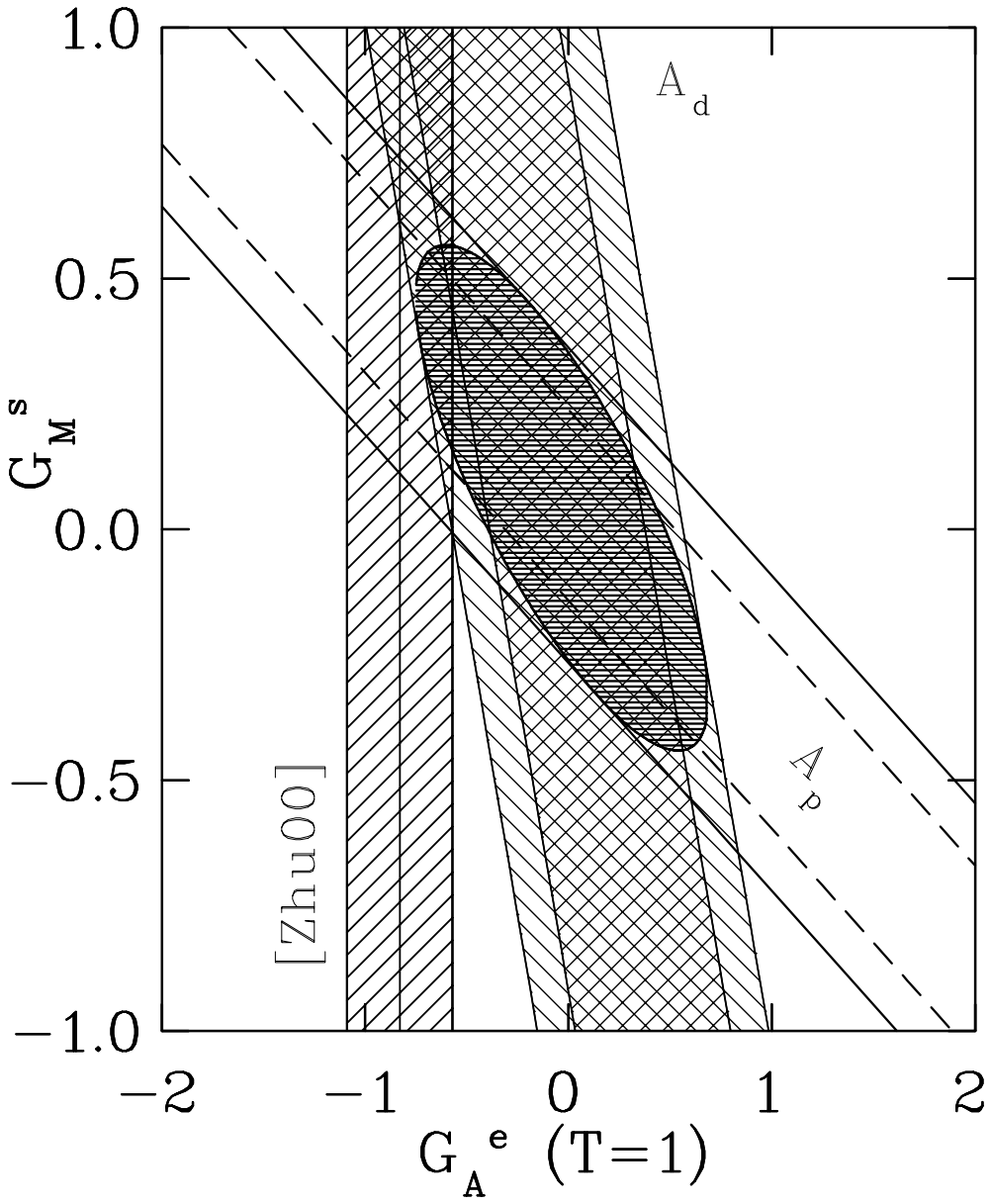

Figure 4.4: This figure shows the region in G_M^s versus $G_A^e(T=1)$ space allowed by the measurements of A_p and A_d reported here. The pair of slanting, intersecting bands correspond to the measured values of A_p and A_d with all errors added in quadrature and the filled ellipse is the region allowed at the 1σ level. The vertical band is the theoretical prediction for $G_A^e(T=1)$ from Ref. [Zhu00]. All results are reported at a Q^2 of 0.1 (GeV/c)^2.

(see equation 1.70). Most of the uncertainty associated with the theoretical calculation of R_A^1 is due to many quark effects of which diagrams attributable to the anapole moment are a contributor. One possible interpretation of the discrepancy between theory and measurement is a larger than expected contribution from the nucleon anapole moment but this issue is still unresolved theoretically.

4.3 Future Prospects

There are several approved experiments at accelerators around the world with the goal of exploring the strange content of the nucleon via parity violating electron scattering. Despite the similar physics goals there is great variety in the techniques used to perform the measurements.

The SAMPLE experiment has been approved to run again at Bates with a deuterium target and a beam energy of 120 MeV, 80 MeV lower than for the results reported here [Ito00]. The motivation for repeating this measurement at a lower beam energy is to take advantage of the substantially different systematic effects to verify the result at 200 MeV. The measured asymmetry will be smaller, but the signal-to-background ratio is expected to be improved. If the value of A_d measured in the new experiment yields a value of $G_A^e(T=1)$ in agreement with the published result, then a measurement of $G_A^e(T=1)$ that disagrees with the theoretical value at the 2σ level can be performed with 110 Coulombs of beam. This is comparable to the amount of data reported on in this work.

There is an active parity violation program at the Thomas Jefferson National Accelerator Facility in Newport News, Virginia in experimental halls A and C. In 1998 and 1999 the HAPPEX collaboration used forward angle parity violating elastic $\vec{e}$-p scattering to measure A_p at a Q^2 of 0.48 (GeV/c)^2 [Ani00, Ani99]. They used the existing pair of High Resolution Spectrometers (HRS) in Hall A to separate elastic electrons from inelastic events and detected the electrons with Čerenkov detectors. Due to the high count rates in the experiment they employed integrating electronics similar to the SAMPLE data acquisition. At this momentum transfer A_p is sensitive to G_M^s and G_E^s, but not to $G_A^e(T=1)$. Their result was [Ani00]

$$\frac{(G_E^s + 0.392 G_M^s)}{(G_M^p/\mu_p)} = 0.069 \pm 0.056 \pm 0.039 \tag{4.19}$$

where the first error is experimental and the second is due to uncertainties in the EM form factors.

The HAPPEX collaboration intends to repeat their forward angle measurement, but at the SAMPLE Q^2 of 0.1 (GeV/c)^2 [Kum99]. By employing the same experimental technique at the reduced Q^2 HAPPEX II will be able to measure an asymmetry sensitive to the linear combination $\rho_s + \mu_p \mu_s$ where $\rho_s = \frac{\mathrm{d}G_E^s(\tau)}{\mathrm{d}\tau}$ as $\tau \propto Q^2 \to 0$ (see equation 1.29). A complementary experiment to measure the asymmetry in elastic scattering of polarized electrons from ^{4}He at the same Q^2 will result in an independent measurement of ρ_s [Arm00]. The combination of the two experiments will result in a determination of $G_M^s(Q^2 = 0.1(\mathrm{GeV/c})^2)$

independent of the SAMPLE result and of $G_A^e(T=1)$.

A separate experiment to measure G_E^s in Hall A at a Q^2 of 0.6 (GeV/c)^2 using the ^{4}He technique has also been proposed [Bei01]. This experiment will also use a cryogenic helium target and the HRS, but the counting rate will be low enough that integration electronics will not be necessary. Particle tracking will be used to separate signal from background.

The goal of the G0 experiment in Hall C is to determine G_M^s and G_E^s over a range of Q^2 from 0.1 to 1.0 (GeV/c)^2 [Bec00]. In order to achieve this a series of forward and backward angle elastic $\vec{e}$-p scattering measurements must be performed. A large toroidal spectrometer magnet and dedicated detector will be employed in conjunction with a specially designed cryogenic target. In forward angle mode the recoil protons will be detected in scintillating detectors using counting electronics; the scattered electrons will be detected when the backward angle measurements are taken. This experiment is also sensitive to $G_A^e(T=1)$ when running in backward angle mode.

Finally, there is a proposal at the Mainz Microtron (MAMI) in Germany to measure the forward angle asymmetry in elastic $\vec{e}$-p scattering [Har01]. The A4 collaboration will probe a linear combination of G_M^s and G_E^s at a Q^2 of 0.225 (GeV/c)^2 using a large acceptance (0.8 sr) calorimetric detector. Their goal is to have sufficient energy resolution to reject inelastic electron scattering and other background events.

4.4 Conclusions

Parity violating electron scattering is a powerful tool for exploring the flavor composition of the nucleon. Its sensitivity to strange quark observables makes it an excellent probe of the low energy properties of the quark sea. Measurements of the backward angle proton and deuteron asymmetries were performed at a Q^2 of 0.1 $(\mathrm{GeV/c})^2$ with the following results:

$$A_p = -5.61 \pm 0.67 \pm 0.88 \text{ ppm} \tag{4.20}$$

$$A_d = -7.28 \pm 0.68 \pm 0.75 \text{ ppm.} \tag{4.21}$$

where the first error is due to the statistics of the measurement and the second is due to systematic effects. A comparison of the measured result with theoretical calculations of A_p and A_d make it possible to extract the strange magnetic form factor of the proton G_M^s, the contribution of the strange quarks to the magnetic moment of the proton:

$$G_M^s \left(Q^2 = 0.1(\mathrm{GeV/c})^2\right) = 0.06 \pm 0.32 \pm 0.39 \pm 0.03 \tag{4.22}$$

The final error is due to the uncertainty in $G_M^{\gamma n}(Q^2 = 0.1(\mathrm{GeV/c})^2$. At a Q^2 of 0, the strange magnetic form factor becomes

$$\mu_s = -0.06 \pm 0.32 \pm 0.39 \pm 0.07 \text{ n.m.} \tag{4.23}$$

This result is in good agreement with calculations of this quantity based on various hadronic models and using lattice QCD. It implies that the strange quarks

contribute very little to the magnetic moment of the proton and neutron, less than 6% and 9% respectively.

The weak magnetic form factors of the proton G_M^{Zp} and neutron G_M^{Zn} can be written in terms of the EM magnetic form factors of the nucleon and G_M^s (equation 1.68 and 1.69):

$$G_M^{Zp}\left(Q^2 = 0.1(\mathrm{GeV/c})^2\right) = 1.55 \pm 0.32 \pm 0.39 \pm 0.03 \tag{4.24}$$

$$G_M^{Zn}\left(Q^2 = 0.1(\mathrm{GeV/c})^2\right) = -2.21 \pm 0.32 \pm 0.39 \pm 0.03. \tag{4.25}$$

The result for G_M^{Zp} is in agreement with the value of $1.36 \pm 0.36 \pm 0.16 \pm 0.20$ reported in Ref. [Mue97a]*; G_M^{Zn} has not been reported previously. The magnetic form factors of the two lightest quark flavors can be extracted from G_M^{Zp} and the EM form factors (equations 1.48 and 1.49)†:

$$G_M^{u}\left(Q^2 = 0.1(\mathrm{GeV/c})^2\right) = 2.89 \pm 0.32 \pm 0.39 \pm 0.03 \tag{4.26}$$

$$G_M^{d}\left(Q^2 = 0.1(\mathrm{GeV/c})^2\right) = -0.74 \pm 0.32 \pm 0.39 \pm 0.03. \tag{4.27}$$

The isovector axial form factor of the nucleon $G_A^e(T=1)$ can also be determined from A_p and A_d:

$$G_A^e(T=1)\left(Q^2 = 0.1(\mathrm{GeV/c})^2\right) = -0.03 \pm 0.48 \pm 0.54 \pm 0.12 \tag{4.28}$$

where the final error is due to the uncertainty in G_M^n and $G_A^e(T=0)$. This result differs from the theoretical prediction of -0.83 ± 0.26 by roughly 1σ [Zhu00]. One

*There is a factor of four difference in the definition of G_M^{Zp} in the two works.

†G_M^{Zp} and G_M^{Zn} must be recalculated assuming $R_V^p = R_V^n = R_V^{(0)} = 0$.

possible explanation for the discrepancy would be a non-zero nucleon anapole moment analogous to the nuclear anapole moment recently measured using atomic parity violation in ^{137}Cs [Woo97]. However, there are many unresolved theoretical issues surrounding this interpretation and the error bars are too large to make definitive statements. Future experiments at Bates, Jefferson Lab, and MAMI should improve these measurements of G_M^s and $G_A^e(T=1)$ as well as constrain the strange electric form factor G_E^s.

Appendix A

Feedback Mechanisms

This experiment employs a variety of feedback mechanisms to ensure that the electron beam's properties are stable in the long term and in the short term. Long term stability can apply on a time scale from several seconds to several days. Short term stability usually implies stability from one pulse to the next. Both kinds of stability are important, providing confidence that background levels are the same throughout the experiment and that helicity correlated beam parameter differences are minimized. This appendix will discuss three different feedback systems.

A.1 Energy

Energy feedback is an example of a long and short term feedback mechanism. The goal is to keep the beam energy stable, implying stability throughout the experiment between pulses and between days. In particular, the electron beam

energy tends to drift due to 60 Hz AC line noise and to fluctuations in the environment variables such as temperature [Bar00]. The 60 Hz noise shows up as a change in energy from one time slot to the next due to the pulse structure of the electron beam (Section 2.2). Since experimental asymmetries are formed between pulses separated by $\frac{1}{60}$ of a second AC line noise fluctuations are not particularly troublesome; the fluctuation is not helicity dependent. Longer term drifts in beam energy can be troublesome because of the potential for scrape off on the slits in the ECS chicane (Section 2.2.2). Scraping on the energy slits is an important source of background in the experiment; therefore a long term drift in the beam energy can lead to long term changes in the experimental background. As discussed in Section 2.7 the background has to be measured separately from the main data collection, therefore it is an important requirement that the background remain stable in the long term.

A.1.1 Principle

The twelve klystrons that constitute the linear accelerator are tuned* in such a way that the crest of the RF field in a given cavity corresponds to the arrival of a pulse of electrons (Section 2.2). One of the klystrons in the linac is detuned so that the RF crest and the arrival of electrons do not coincide. The phase

*Tuning refers to the adjustment of the phase of a cavity's RF field with respect to a common reference.

ϕ of this klystron can be rapidly adjusted to compensate for changes in phase throughout the rest of the accelerator. The beam energy is measured on a pulse-by-pulse basis in the magnetic chicane at the end of the linear accelerator. This monitor is used to determine how much the phase of the detuned klystron needs to be adjusted to keep the energy E stable; the amount of adjustment required is determined by the relation

$$\Delta\phi \equiv -\Delta E \left(\frac{\partial E}{\partial \phi}\right)^{-1}. \tag{A.1}$$

The energy slope $\left(\frac{\partial E}{\partial \phi}\right)$ is measured by varying the phase in a controlled way and measuring the energy, then it is input as a parameter to the feedback.

A.1.2 Implementation

The energy feedback system consists of three parts: the beam position monitor that measures the energy, the fast phase shifter that adjusts the klystron phase, and the CAMAC based interface between the two [Bar00]. The type of BPM used as the energy monitor is discussed in Section 2.2.3. The output voltage is integrated over the length of the beam pulse and digitized by a 16 bit ADC like the rest of the SAMPLE electronics. This signal is read in by the data acquisition portion of the interface and analyzed. The analyzer accumulates data for a set number of beam pulses, usually about a 1000 (100 in each time slot), and computes the average energy deviation ΔE_n in each time slot n. Equation A.1 is applied to extract the necessary phase adjustment for each time slot $\Delta\phi_n$.

The phase adjustments are stored in a memory module and sent to the phase shifter far enough in advance that the klystron phase has stabilized before the pulse arrives. For further details on the energy feedback system see Ref. [Bar00].

A.1.3 Results

The energy feedback system is very successful in reducing both 60 Hz and long term energy drifts. As Figure A.1 illustrates, the drift in energy from time slot to time slot is reduced an order of magnitude from 0.3% to 0.02% [Bar00]. Similarly, the ability of the system to remove long term drifts in the energy, over a period of a couple hours in this case, is shown in Figure A.2.

A.2 Position

Position feedback is a short term mechanism for reducing helicity correlated beam position differences. As was discussed in Section 3.2 it is important to remove helicity correlated beam parameter differences because they can lead to false asymmetries in the final measurement.

Helicity correlated differences in beam position originate in the polarized source from the laser beam striking different points on the GaAs crystal depending on the helicity. There are two different mechanisms by which the laser beam can shift position on the crystal [Ave99]: angular steering by the Pockels cell and differential transmission through the optics. The latter effect is caused by the

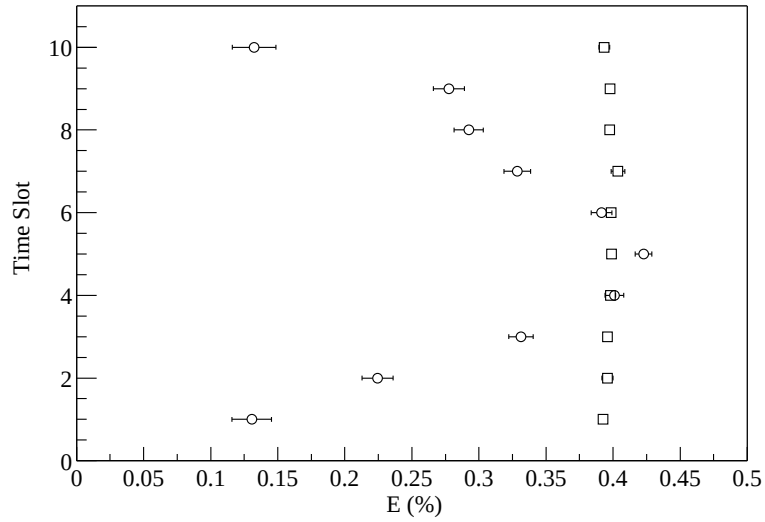

Figure A.1: Measured beam energy in each time slot with (squares) and without (circles) energy feedback turned on [Bar00]. The averages in each time slot represent approximately 10 s worth of data. Energy feedback was set to a value of 0.4% above the central energy.

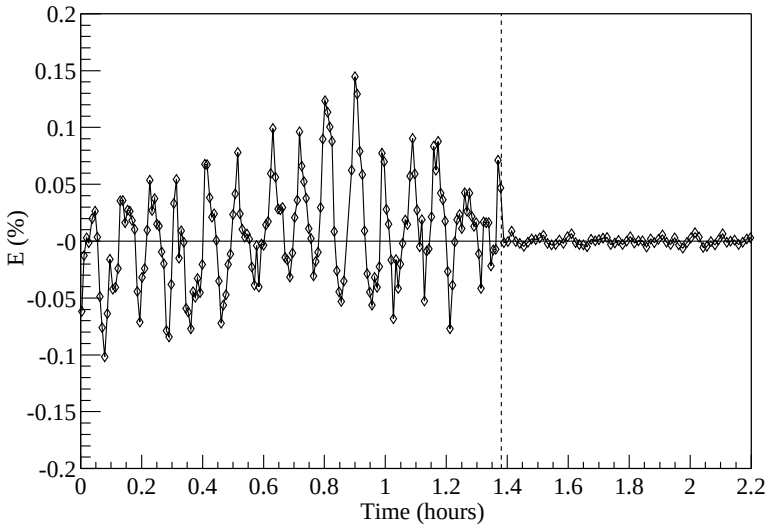

Figure A.2: Measured beam energy as a function of time before and after energy feedback was enabled [Bar00]. The dashed line indicates the point at which energy feedback was activated. These data were collected from a single time slot.

different reflectivities of the optical mirrors to the residual linear polarization of the laser beam after passing through the helicity generation Pockels cell (HPC). Prior to 1998 the polarized source was reconfigured in such a way that there are no longer any mirrors after the HPC (Figure 2.2), therefore this can no longer be a source of beam parameter differences. However, the HPC itself can steer the laser and generally does so differently for the two helicity states. Since the laser light has to travel a significant distance (a few meters) after leaving the HPC before striking the crystal a small angular displacement between the two helicity states can lead to a large position difference on the crystal. In turn this position difference can propagate through the accelerator into the experimental area. Without any kind of feedback system in place these position differences in the North Hall were measured to be $\Delta X = -44.2 \pm 4.2$ nm and $\Delta Y = 102.4 \pm 3.3$ nm over the period of time in 1998 when the feedback system was not in use ("Piezo Off" in Table 3.3).

A.2.1 Principle

In order to correct this beam parameter difference a feedback system is installed on the laser table in the polarized source (Figure 2.2). This system operates on the principle that transmitted light can undergo a transverse, not angular, displacement after passing through a piece of optical glass that is not precisely perpendicular to the incident light. This transverse displacement δ is proportional

to the thickness of the glass t and the angle of the glass with respect to the laser θ [Ave99]:

$$\delta = \left(1 - \frac{n_a}{n_g}\right) t\theta \tag{A.2}$$

where $n_{a(g)}$ is the index of refraction of air (glass). The glass angle θ is adjusted between pulses of different helicity in the same time slot such that the transverse displacement compensates for the steering due to the Pockels cell.

A.2.2 Implementation

The feedback system consists of two pieces: the piezo-electric glass tilting mechanism and the control system. A 6 mm thick optical flat of glass is mounted on a commercial piezo-electric tilting mechanism (Polytec PI Model S-311.10) [Ave99]. This tilting mechanism consists of three stacks of piezo-electric crystals, the thicknesses of which vary depending on the applied voltage. By applying different voltages to each of the three stacks the optical flat can be tilted angularly with respect to the incident laser light. The bottom two stacks operate as a pair to tilt the glass in x and the top stack provides the steering in y. This piezo-electric device is mounted on the laser table with a two-axis mount so that it can be precisely aligned with the laser. The control system applies the necessary voltages V_1 and V_2 to the piezo-electric stacks in a helicity correlated manner.

The North Hall beam position differences are measured for eight hours, long enough to determine them at the 25 nm level. The piezoelectric control system

is adjusted to remove the measured difference until another adjustment is made after eight hours of data collection. The differences in X and Y measured in the North Hall are not simply related to x and y on the laser table due to the transmission characteristics of the linac. A 2×2 matrix is used to convert the differences measured in the hall, ΔX and ΔY, into the voltages V_1 and V_2 necessary for the piezo-electric device:

$$\begin{pmatrix} V_1 \\ V_2 \end{pmatrix} = M \begin{pmatrix} \Delta X \\ \Delta Y \end{pmatrix}. \tag{A.3}$$

The matrix M^{-1} is measured by setting the voltages to certain values and measuring the resulting set of position differences. Representative calibration data are shown in Figure A.3. For more details on the piezo-electric position feedback system see Ref. [Ave99].

A.2.3 Results

The piezo-electric feedback system was not used for the first few weeks of the experiment in 1998 so there is a good baseline of position difference data with which to compare the corrected beam position. Figure 3.3 shows the average beam position difference over time for each setting of the helicity reversal plate. The first few weeks without feedback clearly has a significant non-zero position difference in both X and Y (-44.2 ± 4.2 nm and 102.4 ± 3.3 nm as mentioned previously). After the feedback was activated the average differences for the

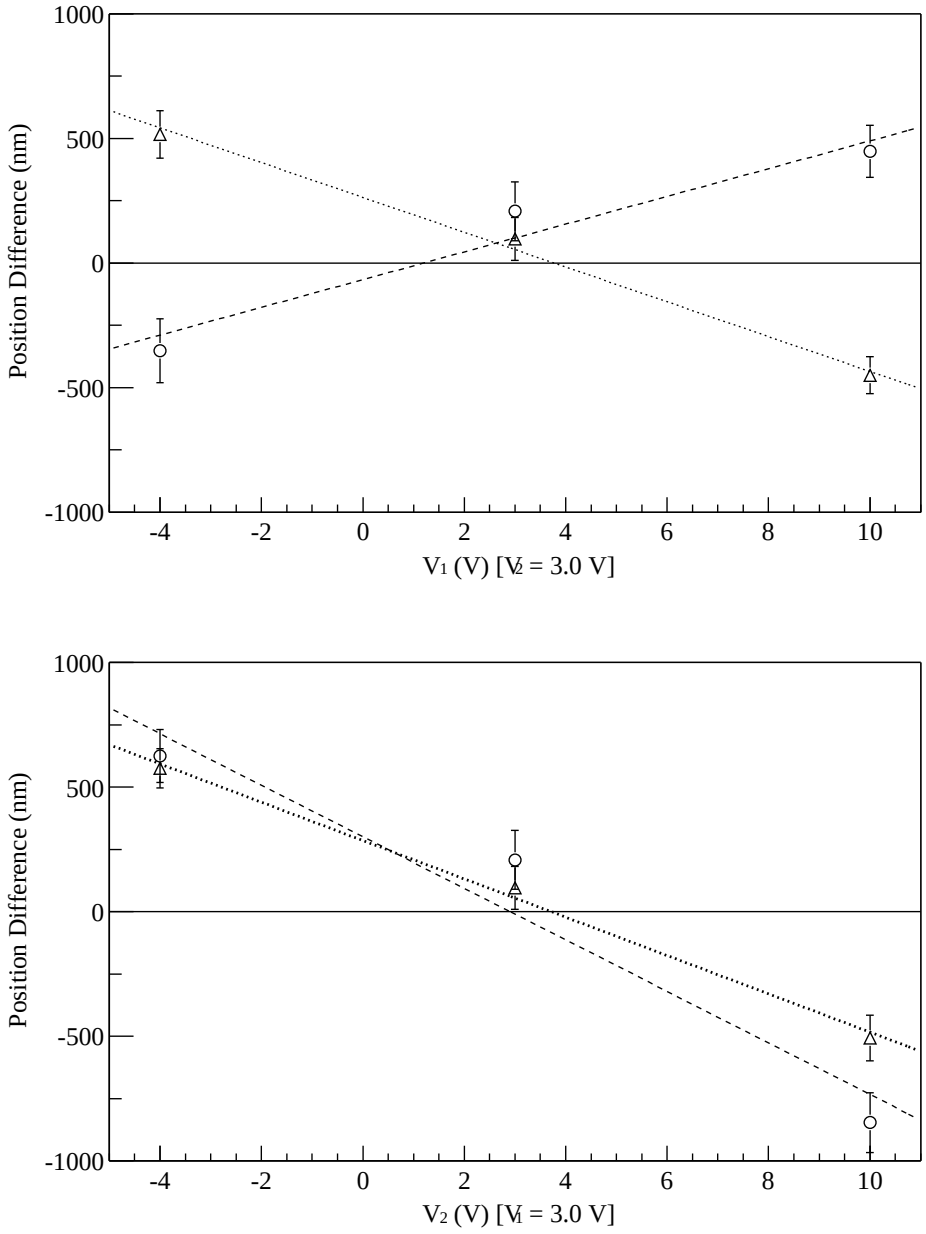

Figure A.3: Calibration data for the piezo-electric position feedback apparatus. In the top graph V_1 is varied as V_2 is held constant at 3 V; in the bottom graph the opposite is true. Average positions measured by the NH2X(Y) BPMs are represented by open circles (triangles); linear fits to the X (Y) data are represented by dashed (dotted) lines.

entire experiment dropped to $\Delta X = 7.8 \pm 2.3$ nm and $\Delta Y = -1.7 \pm 1.4$ nm ("Piezo On" in Table 3.3).

A.3 Polarization Induced Transport Asymmetry

Polarization induced transport asymmetry (PITA) feedback is a short term feedback mechanism for reducing helicity correlated differences in the beam charge. This feedback was implemented by the ^{12}C parity violation experiment [Kum90, Mic88]. At that time the polarized source was set up in such a way that beam charge differences could be generated via a mechanism similar to that which makes position feedback necessary (Section A.2). The HPC does not generate perfectly circular polarized light; there are residual linear components which tend to be different for the two circularly polarized states. The linear components would be transported through other optical elements differently, resulting in a difference in intensities between the two states when the light strikes the crystal. The number of ejected electrons is proportional to the incident light intensity therefore there is a difference in beam charge. In the present configuration there are no optical elements between the HPC and the GaAs crystal so this is not a valid mechanism for the generation of charge differences.

Helicity correlated beam charge differences are particularly irksome because

they impact multiple aspects of the experiment. The charge difference can show up as a false asymmetry in the measured yield once the yield has been normalized to beam charge. It can also lead to a helicity correlated beam energy difference because of the difference in beam loading through the linac for different amounts of charge. The trajectory through the chicane can be different as well resulting in differential scraping on the energy defining slits and a helicity dependent background asymmetry. This confluence of effects makes it important to reduce PITA as much as possible.

A.3.1 Principle

In order to compensate for beam charge asymmetries it is necessary to adjust the laser intensity in a helicity correlated way such that the effects of differential transport are canceled out. This is accomplished by measuring the beam charge asymmetry in the accelerator and adjusting the voltage applied to a Pockels cell to modulate the laser intensity accordingly.

A.3.2 Implementation

When the PITA effect was first investigated, and a feedback mechanism implemented, it was determined that the PITA asymmetry could be altered by

adjusting the high voltage on the helicity Pockels cell between the two states:

$$V_{\pm} = V_0 \pm \Delta \tag{A.4}$$

$$V_+ + V_- = 2V_0 \tag{A.5}$$

where $V_{\pm}$ is the high voltage in the positive (negative) helicity state, Δ is the offset chosen to alter the PITA asymmetry, and V_0 is the baseline voltage necessary to create circularly polarized light. PITA was found to be linearly proportional to Δ, the correlation was determined and used to correct PITA by measuring the charge asymmetry in the accelerator for approximately three minutes and adjusting Δ appropriately.

During the spring of 1997 the SAMPLE collaboration carried out its own investigation of PITA effects and discovered that the PITA feedback mechanism had the unwanted side effect of altering the laser trajectory in a helicity correlated way [Pit01]. This in turn led to helicity correlated beam position differences in the North Hall. As a result of these studies a new feedback mechanism was implemented: the intensity modulation was moved to a different Pockels cell, the corrections Pockels cell (CPC), placed before the HPC (Figure 2.2). This change made it possible to change the laser intensity prior to the light being made circularly polarized and reduced the steering in the HPC.

The feedback system used during the 1998 data run is shown in Figure 2.2. It consisted of a linear polarizer followed by a $\lambda/10$ retardation plate. The purpose of this plate was to allow reasonable intensity modulation using low voltages (0

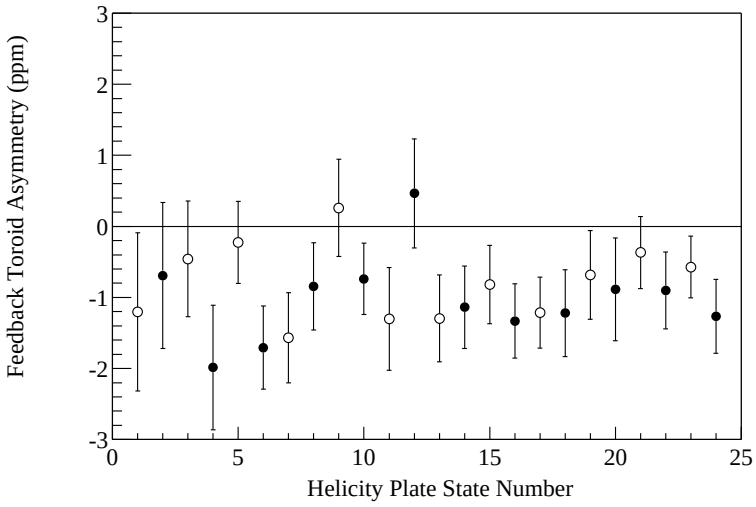

Figure A.4: Charge asymmetry measured on the feedback toroid as a function of helicity plate setting (each setting represents approximately 24-48 hours). Filled (empty) circles correspond to the helicity plate being in (out). This asymmetry does not reverse sign as the helicity plate is inserted or removed, which would be an indication that the asymmetry was helicity dependent. The average asymmetry for the entire experiment was -0.90 ± 0.12 ppm.

to 10 volts) on the Pockels cell. During the 1999 SAMPLE experiment with deuterium the $\lambda/10$ plate was removed and the CPC was operated at a large bias voltage. A final linear polarizer set in the same orientation as the first completed the system.

A.3.3 Results

Figure A.4 shows the charge asymmetry measured on the accelerator toroid used to drive PITA feedback over the course of the experiment. Unlike helicity dependent asymmetries this one does not reverse sign as the helicity plate is inserted or

removed, but the measured asymmetry is decidedly non-zero, -1.06 ± 0.18 ppm for the helicity plate in data and -0.76 ± 0.17 for the out data. This result is not ideal, but any false asymmetry generated in the main detector is removed by the corrections procedure discussed in Section 3.2.

Appendix B

Detector Slopes

Table B.1: Average yield slopes C_k for each mirror sorted by open/closed shutter, helicity plate in/out, and piezo on/off/all. The units are PE/nC/Q where Q is mm for X and Y, mr for θ_X and θ_Y, % for E, and nC for I.

	Piezo	Open Shutters		Closed Shutters	
P_k	Data Set	C_k (In)	C_k (Out)	C_k (In)	C_k (Out)
			Mirror 1		
	Off	−0.5325(15)	−0.1139(13)	−0.1408(17)	0.1273(19)
X	On	−0.3092(7)	−0.2208(7)	−0.1489(8)	0.0146(7)
	All	−0.3458(6)	−0.1952(6)	−0.1475(7)	0.0291(7)
	Off	2.2566(23)	2.3688(22)	−0.8814(19)	0.0130(18)
Y	On	1.1572(13)	−0.7667(9)	−0.3722(11)	−1.4676(12)
	All	1.4187(11)	−0.3105(9)	−0.4995(9)	−1.0351(10)
	Off	15.5097(769)	6.6102(610)	1.9863(727)	1.3591(746)
θ_X	On	11.9488(266)	17.7106(322)	2.0348(255)	−1.3414(316)
	All	12.3305(252)	15.2983(285)	2.0295(241)	−0.9300(291)
	Off	−13.1362(56)	−15.2545(73)	0.8249(118)	−2.5895(83)
θ_Y	On	−6.7588(15)	−4.0720(59)	0.9485(58)	7.3896(60)
	All	−7.1830(15)	−8.5560(46)	0.9240(52)	3.9713(49)
	Off	0.1163(43)	−3.3114(43)	−0.4390(56)	−0.7605(51)
E	On	−2.1488(32)	−0.5204(20)	−0.3867(28)	−0.1451(24)
	All	−1.3435(25)	−1.0182(18)	−0.3968(25)	−0.2569(22)
	Off	−0.2529(16)	−0.2703(14)	−0.0565(14)	−0.0653(13)
I	On	−0.1870(7)	−0.2335(8)	−0.0305(7)	−0.0444(8)
	All	−0.1978(6)	−0.2419(7)	−0.0357(6)	−0.0499(7)

continued on next page

P_k	Piezo Data Set	Open Shutters C_k (In)	Open Shutters C_k (Out)	Closed Shutters C_k (In)	Closed Shutters C_k (Out)
			Mirror 2		
X	Off	−1.2438(14)	−0.9298(12)	0.3137(18)	0.1447(19)
	On	−1.0690(6)	−0.9630(7)	−0.2815(8)	−0.2128(7)
	All	−1.0985(6)	−0.9549(6)	−0.1814(7)	−0.1657(7)
Y	Off	2.1132(20)	2.3301(20)	−1.6090(19)	−1.0504(19)
	On	0.3337(12)	−1.6945(8)	0.0848(11)	−1.6515(12)
	All	0.7709(10)	−1.0868(8)	−0.3553(10)	−1.4727(10)
θ_X	Off	12.3865(691)	2.3690(552)	−2.7960(735)	0.8467(767)
	On	11.4164(244)	12.2224(295)	1.7452(264)	−3.2586(326)
	All	11.5241(230)	10.0392(260)	1.2258(248)	−2.6302(300)
θ_Y	Off	−8.0926(51)	−9.4059(66)	3.9248(118)	−2.0886(85)
	On	−6.0733(14)	−6.6945(54)	−2.0360(61)	7.7141(62)
	All	−6.2129(13)	−7.7976(42)	−0.7889(54)	4.3327(50)
E	Off	−1.3762(38)	−2.3366(39)	−0.2257(57)	−0.9801(53)
	On	−1.4770(29)	−0.8146(18)	−0.5046(28)	−0.2210(25)
	All	−1.4401(23)	−1.0932(17)	−0.4497(25)	−0.3588(22)
I	Off	−0.2082(14)	−0.2843(12)	−0.0949(14)	−0.1104(13)
	On	−0.1658(6)	−0.1840(7)	−0.0319(7)	−0.0437(8)
	All	−0.1730(6)	−0.2075(6)	−0.0448(6)	−0.0613(7)
			Mirror 3		
X	Off	−0.8125(11)	−0.4484(9)	−0.0988(12)	0.0375(14)
	On	−0.6543(5)	−0.6901(5)	−0.1634(6)	−0.0074(5)
	All	−0.6808(5)	−0.6308(5)	−0.1521(5)	−0.0013(5)
Y	Off	3.0118(16)	4.4594(16)	−0.7876(14)	−0.3003(13)
	On	0.9319(9)	0.2944(7)	−0.1483(8)	−1.1643(9)
	All	1.4471(8)	0.9232(6)	−0.3126(7)	−0.9018(7)
θ_X	Off	10.4256(548)	4.8637(436)	0.9636(523)	1.2886(536)
	On	13.3478(196)	11.1449(235)	1.4340(189)	−0.8330(234)
	All	13.0179(184)	9.7291(207)	1.3799(178)	−0.4927(215)
θ_Y	Off	−7.9805(40)	−11.3072(52)	1.4053(85)	−0.8644(60)
	On	−3.3684(11)	−2.4702(43)	−0.5899(43)	5.7560(44)
	All	−3.6906(11)	−6.0955(33)	−0.1805(39)	3.4147(36)
E	Off	−1.4005(30)	−1.8100(31)	−0.1146(41)	−0.5537(37)
	On	−1.3526(23)	−2.1556(15)	−0.1557(20)	0.0288(18)
	All	−1.3702(18)	−2.0921(13)	−0.1476(18)	−0.0813(16)
I	Off	−0.1296(11)	−0.1567(10)	−0.0421(10)	−0.0286(9)
	On	−0.1335(5)	−0.1316(5)	−0.0117(5)	−0.0270(6)
	All	−0.1329(5)	−0.1376(5)	−0.0179(5)	−0.0274(5)

continued on next page

P_k	Piezo Data Set	Open Shutters C_k (In)	Open Shutters C_k (Out)	Closed Shutters C_k (In)	Closed Shutters C_k (Out)
			Mirror 4		
X	Off	−0.1092(20)	0.0811(17)	−0.2456(23)	0.0771(25)
	On	0.1494(9)	0.3813(9)	−0.1944(10)	−0.0429(10)
	All	0.1072(8)	0.3096(8)	−0.2030(10)	−0.0274(9)
Y	Off	2.4075(29)	0.8568(29)	−0.4273(25)	0.2429(24)
	On	0.4502(16)	0.7164(12)	−0.2777(14)	−1.2714(16)
	All	0.9152(14)	0.7369(11)	−0.3149(13)	−0.8266(13)
θ_X	Off	25.1245(995)	11.1876(791)	1.4710(977)	1.6216(993)
	On	9.9218(344)	8.2027(416)	3.4331(343)	−2.4544(424)
	All	11.5445(325)	8.8496(368)	3.2183(323)	−1.8250(390)
θ_Y	Off	−16.9953(73)	−11.4720(94)	−0.5755(158)	−3.6303(111)
	On	−11.0440(19)	−5.0630(77)	0.2331(78)	5.1483(80)
	All	−11.4370(19)	−7.6309(60)	0.0740(70)	2.1212(65)
E	Off	−1.8957(55)	−2.7702(56)	−0.4855(76)	−0.8737(68)
	On	−2.7725(41)	−1.0317(26)	−0.3669(37)	−0.3042(32)
	All	−2.4582(33)	−1.3401(23)	−0.3898(33)	−0.4093(29)
I	Off	−0.2950(21)	−0.3017(18)	−0.0268(19)	−0.0691(17)
	On	−0.2683(9)	−0.3121(10)	−0.0465(9)	−0.0424(10)
	All	−0.2727(8)	−0.3097(9)	−0.0426(8)	−0.0495(9)
			Mirror 5		
X	Off	0.1753(14)	−0.4516(11)	−0.3166(23)	0.0994(25)
	On	−0.1226(6)	−0.2189(7)	−0.1336(11)	0.0862(10)
	All	−0.0704(6)	−0.2786(6)	−0.1672(10)	0.0881(9)
Y	Off	2.6540(20)	3.4605(19)	−3.1075(25)	−1.0236(24)
	On	0.3585(12)	−1.2787(8)	−0.6516(15)	−1.9086(16)
	All	0.9585(10)	−0.5084(8)	−1.3188(13)	−1.6191(13)
θ_X	Off	10.9653(666)	9.2269(528)	1.2081(949)	2.8760(971)
	On	13.1786(246)	13.7833(296)	3.3966(359)	−2.1026(444)
	All	12.9133(231)	12.6944(258)	3.1234(335)	−1.2410(404)
θ_Y	Off	−4.5163(49)	−14.9973(63)	2.7651(154)	−0.0082(108)
	On	−11.6973(14)	−3.5367(55)	1.9785(82)	8.5071(84)
	All	−11.1422(14)	−8.4932(41)	2.1524(72)	5.3143(66)
E	Off	−0.7793(37)	−2.6393(37)	0.0455(75)	−0.8590(67)
	On	−1.1770(29)	−2.1845(18)	−0.3921(38)	−0.2177(33)
	All	−1.0255(23)	−2.2746(17)	−0.3021(34)	−0.3461(30)
I	Off	−0.1394(14)	−0.2159(12)	−0.0966(18)	−0.0597(17)
	On	−0.1574(6)	−0.1152(7)	−0.0663(10)	−0.0531(11)
	All	−0.1541(6)	−0.1402(6)	−0.0728(9)	−0.0550(9)

continued on next page

P_k	Piezo Data Set	Open Shutters C_k (In)	Open Shutters C_k (Out)	Closed Shutters C_k (In)	Closed Shutters C_k (Out)
			Mirror 6		
X	Off	−0.7826(12)	−0.8332(10)	−0.6171(21)	−0.1397(23)
	On	−0.7145(5)	−0.7070(6)	−0.4101(10)	−0.1980(9)
	All	−0.7256(5)	−0.7374(5)	−0.4455(9)	−0.1902(8)
Y	Off	1.7004(18)	1.8874(17)	−1.4282(23)	−0.4990(22)
	On	0.1360(10)	−1.2260(7)	−0.5786(13)	−1.8511(15)
	All	0.5162(9)	−0.7604(7)	−0.7952(12)	−1.4400(12)
θ_X	Off	7.8170(603)	5.9883(478)	1.9538(884)	4.1213(897)
	On	10.5799(212)	6.7063(255)	2.6374(316)	−1.4676(392)
	All	10.2755(200)	6.5469(225)	2.5601(297)	−0.5707(359)
θ_Y	Off	−6.2515(44)	−8.5757(57)	2.8779(143)	−0.9863(100)
	On	−10.6843(12)	−1.2000(47)	0.2513(72)	8.9190(74)
	All	−10.3809(12)	−4.1911(36)	0.7852(65)	5.4209(60)
E	Off	−0.7403(33)	−2.0568(34)	−0.2144(69)	−1.0372(61)
	On	−1.1458(25)	−1.4991(16)	−0.4371(34)	−0.0074(30)
	All	−0.9990(20)	−1.6003(14)	−0.3941(30)	−0.2009(27)
I	Off	−0.1429(12)	−0.1842(11)	−0.0777(17)	−0.0575(16)
	On	−0.1325(6)	−0.1214(6)	−0.0523(9)	−0.0515(9)
	All	−0.1342(5)	−0.1361(5)	−0.0575(8)	−0.0532(8)
			Mirror 7		
X	Off	−1.8929(13)	−0.8978(11)	−0.0892(15)	−0.0931(17)
	On	−0.9039(6)	−0.8170(6)	−0.1863(7)	−0.0857(6)
	All	−1.0588(5)	−0.8357(5)	−0.1705(6)	−0.0866(6)
Y	Off	−0.0662(19)	2.6920(19)	−0.0263(17)	−0.0319(16)
	On	−0.3405(11)	−0.7939(8)	−0.3086(9)	−0.9870(10)
	All	−0.2779(9)	−0.3034(7)	−0.2409(8)	−0.7181(8)
θ_X	Off	5.0781(662)	5.3809(526)	1.5881(643)	0.9529(652)
	On	−5.9162(224)	5.8269(270)	−0.1261(220)	−1.1776(271)
	All	−4.7901(212)	5.7339(240)	0.0529(208)	−0.8632(250)
θ_Y	Off	−9.6048(49)	−8.1625(63)	0.1909(104)	−1.0016(73)
	On	−14.1271(12)	−0.2692(50)	0.7381(50)	5.1348(51)
	All	−13.8477(12)	−3.3353(39)	0.6346(45)	3.0932(42)
E	Off	−1.0723(37)	−0.8635(37)	−0.3194(50)	−0.5262(44)
	On	−1.5468(27)	−1.8221(17)	−0.2531(24)	−0.2686(21)
	All	−1.3815(22)	−1.6600(15)	−0.2655(22)	−0.3146(19)
I	Off	−0.2072(14)	−0.2355(12)	−0.0347(12)	−0.0350(11)
	On	−0.1896(6)	−0.2158(6)	−0.0256(6)	−0.0262(7)
	All	−0.1924(5)	−0.2202(6)	−0.0274(5)	−0.0284(6)

continued on next page

P_k	Piezo Data Set	Open Shutters C_k (In)	Open Shutters C_k (Out)	Closed Shutters C_k (In)	Closed Shutters C_k (Out)
			Mirror 8		
X	Off	0.3446(11)	−0.3064(9)	−0.0864(12)	0.0399(13)
	On	0.3545(5)	0.2890(5)	−0.1239(5)	0.0060(5)
	All	0.3529(5)	0.1474(5)	−0.1174(5)	0.0105(5)
Y	Off	1.6343(16)	1.9007(16)	−1.3142(13)	−0.7652(12)
	On	−0.9461(9)	−0.9811(7)	−0.2771(7)	−1.2876(8)
	All	−0.3269(8)	−0.5540(6)	−0.5377(6)	−1.1300(7)
θ_X	Off	13.1970(553)	8.6786(439)	3.2405(495)	0.2465(507)
	On	21.9922(193)	21.5050(233)	1.9725(177)	−0.4372(220)
	All	21.0421(182)	18.6953(206)	2.1160(166)	−0.3286(202)
θ_Y	Off	−4.6378(41)	−14.5120(52)	2.8936(80)	0.9702(57)
	On	2.0094(11)	0.8620(43)	0.2671(41)	5.5632(42)
	All	1.5563(11)	−5.3356(33)	0.7985(36)	3.9503(34)
E	Off	−0.3920(30)	−1.7689(31)	0.0779(39)	−0.3614(35)
	On	−0.9191(23)	−1.8938(14)	−0.1314(19)	0.1364(17)
	All	−0.7305(18)	−1.8715(13)	−0.0910(17)	0.0433(15)
I	Off	−0.1511(11)	−0.1701(10)	−0.0497(10)	−0.0261(9)
	On	−0.1560(5)	−0.1416(5)	−0.0164(5)	−0.0280(5)
	All	−0.1551(5)	−0.1482(5)	−0.0231(4)	−0.0275(5)
			Mirror 9		
X	Off	−0.5881(13)	−0.6423(11)	−0.2073(15)	−0.0099(16)
	On	−0.1657(6)	−0.3938(6)	−0.2502(7)	−0.0823(7)
	All	−0.2407(5)	−0.4593(5)	−0.2425(6)	−0.0721(6)
Y	Off	2.0414(19)	1.7277(18)	−2.4440(16)	−1.5375(16)
	On	−0.9680(11)	−1.8318(8)	−0.7559(10)	−1.6620(11)
	All	−0.1928(9)	−1.2101(7)	−1.2118(8)	−1.6225(9)
θ_X	Off	13.5226(633)	8.7523(495)	1.0686(619)	1.4494(648)
	On	22.6870(232)	20.5547(279)	0.4915(231)	−2.9491(287)
	All	21.6024(218)	17.7120(243)	0.5622(217)	−2.2250(263)
θ_Y	Off	−0.2645(46)	−12.6299(59)	5.1928(100)	0.6100(71)
	On	−3.4936(13)	2.8560(52)	1.2291(53)	7.3713(54)
	All	−3.2550(13)	−3.8704(39)	2.1096(47)	4.8981(43)
E	Off	−0.1503(35)	−2.5211(35)	0.0411(48)	−0.6817(44)
	On	−0.6281(27)	−2.3530(17)	−0.3688(25)	−0.0735(22)
	All	−0.4489(22)	−2.3863(16)	−0.2847(22)	−0.1906(19)
I	Off	−0.1676(13)	−0.2508(11)	−0.0969(12)	−0.0621(11)
	On	−0.1716(6)	−0.1471(7)	−0.0439(6)	−0.0440(7)
	All	−0.1709(6)	−0.1730(6)	−0.0553(6)	−0.0490(6)

continued on next page

P_k	Piezo Data Set	Open Shutters C_k (In)	Open Shutters C_k (Out)	Closed Shutters C_k (In)	Closed Shutters C_k (Out)
			Mirror 10		
X	Off	−1.2740(16)	−1.0090(13)	−0.2002(17)	−0.0141(18)
	On	−0.7875(7)	−0.8044(8)	−0.2388(8)	−0.0659(7)
	All	−0.8673(6)	−0.8536(7)	−0.2322(7)	−0.0590(7)
Y	Off	2.4912(23)	4.2054(23)	−1.7684(18)	−1.1517(18)
	On	−1.9216(13)	−1.0680(10)	−0.6092(11)	−1.9030(12)
	All	−0.8548(11)	−0.2856(9)	−0.9004(9)	−1.6781(10)
θ_X	Off	16.6974(792)	6.4267(630)	4.1540(711)	1.4072(726)
	On	34.5623(279)	22.4479(335)	0.2372(252)	−1.8324(313)
	All	32.5940(263)	18.9235(296)	0.6754(238)	−1.3233(288)
θ_Y	Off	−15.1515(59)	−13.5189(75)	2.8452(116)	1.4297(81)
	On	−5.6209(16)	2.3420(62)	0.1577(58)	8.9471(59)
	All	−6.2521(15)	−4.1052(48)	0.6964(52)	6.3268(48)
E	Off	−1.0487(43)	−2.8289(44)	0.0695(55)	−0.8559(50)
	On	−1.3032(33)	−2.5655(21)	−0.2489(27)	0.1202(24)
	All	−1.2110(26)	−2.6129(19)	−0.1879(24)	−0.0613(21)
I	Off	−0.2037(16)	−0.2609(14)	−0.0695(14)	−0.0457(13)
	On	−0.2457(7)	−0.2160(8)	−0.0330(7)	−0.0329(8)
	All	−0.2387(7)	−0.2264(7)	−0.0403(6)	−0.0363(6)

Table B.2: Average yield slopes C_k for each luminosity monitor sorted by helicity plate in/out and piezo on/off/all. The units are mV/Q where Q is mm for X and Y, mr for θ_X and θ_Y, % for E, and nC for I. The average yield in the luminosity monitors is 274 mV for the left monitor and 307 mV for the right one.

P_k	Piezo Data Set	C_k (In)	C_k (Out)
		Left Luminosity Monitor	
X	Off	−0.9888(6)	−1.0916(6)
	On	−2.6194(4)	−2.6615(4)
	All	−2.1674(3)	−2.0865(3)
Y	Off	−0.4058(40)	−0.5213(36)
	On	−1.6693(20)	−0.6548(21)
	All	−1.4266(18)	−0.6197(18)
θ_X	Off	9.1722(187)	0.7574(150)
	On	1.8658(144)	−1.3228(162)
	All	4.5745(114)	−0.2031(110)

continued on next page

P_k	Piezo Data Set	C_k (In)	C_k (Out)
	Off	−16.8085(155)	−17.5564(137)
θ_Y	On	−10.3919(84)	−14.2689(107)
	All	−11.8580(74)	−15.5113(84)
	Off	−0.7997(24)	−1.0709(23)
E	On	−1.1546(15)	−1.5026(16)
	All	−1.0541(13)	−1.3583(13)
	Off	−0.2693(2)	−0.3230(2)
I	On	−0.4330(1)	−0.4990(1)
	All	−0.3856(1)	−0.4368(1)
		Right Luminosity Monitor	
	Off	2.4718(14)	2.3141(13)
X	On	2.0445(4)	2.1765(4)
	All	2.0764(4)	2.1911(4)
	Off	−3.6404(92)	−3.0928(75)
Y	On	−1.0756(22)	−0.6178(21)
	All	−1.2169(22)	−0.7937(20)
	Off	19.6488(431)	5.8063(333)
θ_X	On	15.0312(149)	13.8993(169)
	All	15.5225(141)	12.2455(150)
	Off	−25.1224(363)	−26.0134(312)
θ_Y	On	−5.2074(101)	−3.5035(106)
	All	−6.6483(98)	−5.8523(101)
	Off	−1.0577(58)	−1.3784(52)
E	On	−0.8805(16)	−1.1231(17)
	All	−0.8924(15)	−1.1473(16)
	Off	−0.8589(4)	−0.8227(4)
I	On	−0.6621(1)	−0.7177(1)
	All	−0.6770(1)	−0.7295(1)

Appendix C

1998 SAMPLE Hydrogen Collaboration

D. T. Spayde[3], T. Averett*[1] D. Barkhuff[4], D. H. Beck[2], E. J. Beise[3], C. Benson[2], H. Breuer[3], R. Carr[1], S. Covrig[1], J. DelCorso[5], G. Dodson[4], K. Dow[4], C. Eppstein[1], M. Farkhondeh[4], B. W. Filippone[1], P.Frazier[1], R. Hasty[2], T. M. Ito[1], C. E. Jones[1], W. Korsch[6], S. Kowalski[4], P. Lee[1], E. Maneva[1], K. McCarty[1], R. D. McKeown[1], J. Mikell[2], B. Mueller[7], P. Naik[2], M. Pitt[5], J. Ritter[2], V. Savu[1], M. Sullivan[1], R. Tieulent[3], E. Tsentalovich[4], S. P. Wells[8], B. Yang[4], and T. Zwart[4]

[1] Kellogg Radiation Laboratory, California Institute of Technology Pasadena, CA 91125, USA

[2] Department of Physics, University of Illinois at Urbana-Champaign, Urbana, Illinois 61801

[3] Department of Physics, University of Maryland, College Park, Maryland 20742

[4] Bates Linear Accelerator Center, Laboratory for Nuclear Science and Department of Physics,
Massachusetts Institute of Technology, Cambridge, Massachusetts 02139

[5] Department of Physics, Virginia Polytechnic Institute and State University, Blacksburg, VA 24061-0435

[6] Department of Physics and Astronomy, University of Kentucky, Lexington, KY 40506

[7] Physics Division, Argonne National Laboratory, Argonne, IL 60439, USA

[8] Department of Physics, Louisiana Tech University, Ruston, LA 71272, USA

*Present address: Department of Physics, College of William and Mary, Williamsburg, VA 23187, USA

Appendix D

1999 SAMPLE Deuterium Collaboration

R. Hasty[2], A. M. Hawthorne-Allen[5], T. Averett[9] D. Barkhuff[4], D. H. Beck[2], E. J. Beise[3], A. Blake[1], H. Breuer[3], R. Carr[1], S. Covrig[1], A. Danagoulian[2], G. Dodson[4], K. Dow[4], M. Farkhondeh[4], B. W. Filippone[1], J. Gao[1], M. C. Herda[3], T. M. Ito[1], C. E. Jones[1], W. Korsch[6], K. Kramer[9], S. Kowalski[4], P. Lee[1], R. D. McKeown[1], B. Mueller[7], M. Pitt[5], J. Ritter[5], J. Roche[9], V. Savu[1], D. T. Spayde[3], R. Tieulent[3], E. Tsentalovich[4], S. P. Wells[8], B. Yang[4], and T. Zwart[4]

[1] Kellogg Radiation Laboratory, California Institute of Technology Pasadena, CA 91125, USA

[2] Department of Physics, University of Illinois at Urbana-Champaign, Urbana, Illinois 61801

[3] Department of Physics, University of Maryland, College Park, Maryland 20742

[4] Bates Linear Accelerator Center, Laboratory for Nuclear Science and Department of Physics,
Massachusetts Institute of Technology, Cambridge, Massachusetts 02139

[5] Department of Physics, Virginia Polytechnic Institute and State University, Blacksburg, VA 24061-0435

[6] Department of Physics and Astronomy, University of Kentucky, Lexington, KY 40506

[7] Physics Division, Argonne National Laboratory, Argonne, IL 60439, USA

[8] Department of Physics, Louisiana Tech University, Ruston, LA 71272, USA

[9] Department of Physics, College of William and Mary, Williamsburg, VA 23187, USA

BIBLIOGRAPHY

[Ack99] K. Ackerstaff et al., Phys. Lett. B **464** (1999), 123.

[Ade98] B. Adeva et al., Phys. Lett. B **420** (1998), 180.

[Ani99] K. A. Aniol et al., Phys. Rev. Lett. **82** (1999), 1096.

[Ani00] K. A. Aniol et al., accepted for publication in Phys. Lett. B, Los Alamos Preprint nucl-ex/0006002 (http://xxx.lanl.gov), 2000.

[Arm00] TJNAF proposal E00-114, (D. S. Armstrong and R. Michaels, spokespersons), 2000.

[Arr92] J. Arrington et al., Nucl. Instr. and Meth. A **311** (1992), 39.

[Ave98] T. D. Averett, *Mirror Edge Effect Corrections for SAMPLE Pulse Counting*, SAMPLE Internal Report, 1998.

[Ave99] T. Averett et al., Nucl. Instr. and Meth. A **438** (1999), 246.

[Bar00] D. H. Barkhuff et al., Nucl. Instr. and Meth. A **450** (2000), 187.

[Bec89] D. H. Beck, Phys. Rev. D **39** (1989), 3248.

[Bec00] TJNAF proposal E00-006, (D. H. Beck, spokesperson), 2000.

[Bei96] E. J. Beise et al., Nucl. Instr. and Meth. A **378** (1996), 383.

[Bei00] E. J. Beise, private communication, 2000.

[Bei01] TJNAF proposal PR01-003, (E. J. Beise, spokesperson), 2001.

[BR92] P. R. Bevington and D. K. Robinson, *Data Reduction and Error Analysis for the Physical Sciences*, second ed., McGraw-Hill, Boston, 1992.

[BR96] R. Brun and F. Rademakers, Nucl. Inst. and Meth. A **389** (1996), 81; see also http://root.cern.ch/.

[CD71] T. P. Cheng and R. Dashen, Phys. Rev. Lett. **26** (1971), 595.

[CFN93] T. D. Cohen, H. Forkel, and M. Nielsen, Phys. Lett. B **316** (1993), 1.

[CJ01a] J.-W. Chen and X. Ji, Phys. Lett. B **501** (2001), 209.

[CJ01b] J.-W. Chen and X. Ji, University of Maryland Preprint UMD-PP-01-018, Los Alamos Preprint hep-ph/0011239 (http://xxx.lanl.gov), 2001.

[DLW98] S. J. Dong, K. F. Liu, and A. G. Williams, Phys. Rev. D **58** (1998), 074504.

[DSvK01] L. Diaconescu, R. Schiavilla, and U. van Kolck, Phys. Rev. C **63** (2001), 044007.

[EJ74a] J. Ellis and R. Jaffe, Phys. Rev. D **9** (1974), 1444.

[EJ74b] J. Ellis and R. Jaffe, Phys. Rev. D **10** (1974), 1669E.

[Far76] Z. D. Farkas et al., *Recent Developments in Microwave Beam-Position Monitors at SLAC*, SLAC Preprint SLAC-PUB-1823, 1976.

[Far99] M. Farkhondeh et al., *Electron Scattering with Polarized Beams at MIT-Bates Accelerator Center*, Proceedings of the Fifteenth International Conference on Applications of Accelerators in Research and Industry (AIP Conf. Proc. CP475) (J. L. Duggan and I. l. Morgan, eds.), AIP I-56396-825-8/99, 1999, p. 261.

[FJ01] B. W. Filippone and X. Ji, Kellogg Radiation Laboratory Preprint MAP-274, Los Alamos Preprint hep-ph/0101224 (http://xxx.lanl.gov), 2001.

[FK72] J. T. Friedman and H. W. Kendall, *Deep Inelastic Electron Scattering*, Ann. Rev. Nucl. Science (E. Segrè, J. R. Grover, and H. P. Noyes, eds.), vol. 22, Annual Reviews Inc., 1972, p. 203.

[FK80] V. V. Flambaum and I. B. Khriplovich, Sov. Phys. JETP **52** (1980), 835.

[FKS84] V. V. Flambaum, I. B. Khriplovich, and O. P. Sushkov, Phys. Lett. B **146** (1984), 367.

[Fla91] J. B. Flanz et al., *Energy Compression System Design for the MIT-Bates Accelerator Center*, Conference Record of the 1991 IEEE Particle Accelerator Conference, 1991, p. 601.

[For97] H. Forkel, Phys. Rev. C **56** (1997), 510.

[For98] T. A. Forest, *A Measurement of the Proton Weak Magnetic Form Factor (G_M^Z) at Q^2=0.1 GeV^2/c^2*, Ph.D. thesis, University of Illinois at Urbana-Champaign, 1998.

[Fow75] G. R. Fowles, *Introduction to Modern Optics*, second ed., Dover, New York, 1975.

[FS33] R. Frisch and O. Stern, Zeit. Physik **85** (1933), 4.

[Gal71] S. Galster et al., Nucl. Phys. B **32** (1971), 221.

[GI97] P. Geiger and N. Isgur, Phys. Rev. D **55** (1997), 299.

[GLS91] J. Gasser, H. Leutwyler, and M. E. Sainio, Phys. Lett. B **253** (1991), 252.

[Gro86] Group MP-1, *Q - User's Information Manual*, Los Alamos National Laboratory, 1986.

[Gro94] CERN Application Software Group, *GEANT Detector Description and Simulation Package Version 3.21*, 1994; see also http://wwwinfo.cern.ch/asd/geant/.

[Gro00] Particle Data Group, D. E. Groom et al., Eur. Phys. J. C **15** (2000), 1.

[Har01] Mainz proposal A4, (D. von Harrach, spokesperson), 2001.

[Has00a] R. Hasty et al., Science **290** (2000), 2117.

[Has00b] R. D. Hasty, private communication, 2000.

[Hax97] W. C. Haxton, Science **275** (1997), 1753.

[HD95] H.-W. Hammer and D. Drechsel, Zeit. Phys. A **353** (1995), 321.

[HKM99] T. R. Hemmert, B. Kubis, and U.-G. Meißner, Phys. Rev. C **60** (1999), 045501.

[HM84] F. Halzen and A. D. Martin, *Quarks and Leptons: An Introductory Course in Modern Particle Physics*, John Wiley & Sons, New York, 1984.

[HMD96] H.-W. Hammer, Ulf-G. Meißner, and D. Drechsel, Phys. Lett. B **367** (1996), 323.

[HMS98] T. R. Hemmert, U.-G. Meißner, and S. Steininger, Phys. Lett. B **437** (1998), 184.

[Höh76] G. Höhler et al., Nucl. Phys. B **114** (1976), 505.

[HP93] S.-T. Hong and B.-Y. Park, Nucl. Phys. A **561** (1993), 525.

[HPD92] E. Hadjimichael, G. I. Poulis, and T. W. Donnelly, Phys. Rev. C **45** (1992), 2666.

[HPM97] S.-T. Hong, B.-Y. Park, and D.-P. Min, Phys. Lett. B **414** (1997), 229.

[HRG00] L. Hannelius, D. O. Riska, and L. Ya. Glozman, Nucl. Phys. A **665** (2000), 353.

[HRM99] H.-W. Hammer and M. J. Ramsey-Musolf, Phys. Rev. C **60** (1999), 045205.

[Ito95] H. Ito, Phys. Rev. C **52** (1995), R1750.

[Ito99] T. M. Ito, *More on STIME*, SAMPLE Internal Report, 1999.

[Ito00] Bates proposal 00-04, (T. Ito, spokesperson), 2000.

[Jac75] J. D. Jackson, *Classical Electrodynamics*, second ed., John Wiley & Sons, New York, 1975.

[Jac01] K. Jacobs, private communication, 2001.

[Jaf89] R. L. Jaffe, Phys. Lett. B **229** (1989), 275.

[Jai88] P. Jain et al., Phys. Rev. D **37** (1988), 3252.

[KHP92] W. Koepf, E. M. Henley, and S. J. Pollock, Phys. Lett. B **288** (1992), 11.

[KL81] T. Kinoshita and W. B. Lindquist, Phys. Rev. Lett. **47** (1981), 1573.

[KM88] D. B. Kaplan and A. Manohar, Nucl. Phys. B **310** (1988), 527.

[KR57] A. A. Kresnin and L. N. Rosentsveig, Sov. Phys. JETP **5** (1957), 288.

[KS83] T. V. Kuchto and N.M. Shumeiko, Nucl. Phys. B **219** (1983), 412.

[Kum90] K. S. Kumar, *Parity Violation in Elastic Electron Carbon Scattering*, Ph.D. thesis, Syracuse University, 1990.

[Kum99] TJNAF proposal E99-115, (K. S. Kumar and D. Lhuillier, spokespersons), 1999.

[KWG97] H.-C. Kim, T. Watabe, and K. Goeke, Nucl. Phys. A **616** (1997), 606.

[Lei95] D. B. Leinweber, Nucl. Phys. A **585** (1995), 341.

[Lei96] D. B. Leinweber, Phys. Rev. D **53** (1996), 5115.

[Leo94] W. R. Leo, *Techniques for Nuclear and Particle Physics Experiments*, second revised ed., Springer-Verlag, Berlin, 1994.

[LHH82] S.-P. Li, E. M. Henley, and W.-Y. P. Hwang, Ann. Phys. **143** (1982), 372.

[Lie99] A. Liesenfeld et al., Phys. Lett. B **468** (1999), 19.

[LT00] D. B. Leinweber and A. W. Thomas, Phys. Rev. D **62** (2000), 074505.

[MB94] M. J. Musolf and M. Burkhardt, Zeit. Phys. C **61** (1994), 433.

[McK89a] Bates proposal 89-06, (R. D. McKeown and D. H. Beck, spokespersons), 1989.

[McK89b] R. D. McKeown, Phys. Lett. B **219** (1989), 140.

[MD92] M. J. Musolf and T. W. Donnelly, Nucl. Phys. A **546** (1992), 509.

[Mei97] U.-G. Meißner et al., Phys. Lett. B **408** (1997), 381.

[MH90] M. J. Musolf and B. R. Holstein, Phys. Lett. B **242** (1990), 461.

[Mic88] R. W. Michaels, *Parity Violation in the Elastic Scattering of Polarized Electrons from* ^{12}C *at 250 MeV*, Ph.D. thesis, Yale University, 1988.

[MM97] M. Malheiro and W. Melnitchouk, Phys. Rev. C **56** (1997), R2373.

[MMD96] P. Mergell, Ulf-G. Meißner, and D. Drechsel, Nucl. Phys. A **596** (1996), 367.

[Møl32] C. Møller, Ann. Phys. **14** (1932), 531.

[MR90] W. J. Marciano and J. L. Rosner, Phys. Rev. Lett. **65** (1990), 2963.

[MT69] L. W. Mo and Y.S. Tsai, Rev. Mod. Phys. **41** (1969), 205.

[Mue97a] B. Mueller et al., Phys. Rev. Lett. **78** (1997), 3824.

[Mue97b] B. A. Mueller, *Measurement of the Strange Quark Contribution to the Magnetic Moment of the Proton*, Ph.D. thesis, California Institute of Technology, 1997.

[Mus94] M. J. Musolf et al., Phys. Rep. **239** (1994), 1.

[NMW88] M. C. Noecker, B. P. Masterson, and C. E. Wieman, Phys. Rev. Lett. **61** (1988), 310.

[NO82] Y. Nogami and N. Ohtsuka, Phys. Rev. D **26** (1982), 261.

[OM59] H. Olsen and L. C. Maximon, Phys. Rev. **114** (1959), 887.

[Pit01] M. L. Pitt, private communication, 2001.

[Pol90] S. J. Pollock, Phys. Rev. D **42** (1990), 3010.

[PS94] S. C. Phatak and S. Sahu, Phys. Lett. B **321** (1994), 11.

[PSW91] N. W. Park, J. Schechter, and H. Weigel, Phys. Rev. D **43** (1991), 869.

[RMI97] M. J. Ramsey-Musolf and H. Ito, Phys. Rev. C **55** (1997), 3066.

[Sim79] G. G. Simon et al., Nucl. Phys. A **324** (1979), 277.

[Spa00] D. T. Spayde et al., Phys. Rev. Lett. **84** (2000), 1106.

[Tie98] R. Tieulent, *Mirror Edge Effect Study in Pulse Counting Mode*, SAMPLE Internal Report, 1998.

[Tsa71] Y. S. Tsai, *Radiative Corrections to Electron Scattering*, SLAC Preprint SLAC-PUB-848, 1971.

[TTM80] S. Théberge, A. W. Thomas, and G. A. Miller, Phys. Rev. D **22** (1980), 2838.

[TTM81] A. W. Thomas, S. Théberge, and G. A. Miller, Phys. Rev. D **24** (1981), 216.

[Vet95] P. A. Vetter et al., Phys. Rev. Lett. **74** (1995), 2658.

[Wei72] V. F. Weisskopf, *Physics in the Twentieth Century: Selected Essays*, MIT Press, Cambridge, 1972.

[Wei95] H. Weigel et al., Phys. Lett. B **353** (1995), 20.

[Wel01] S. P. Wells et al., Phys. Rev. C **63** (2001), 064001.

[Woo97] C. S. Wood et al., Science **275** (1997), 1759.

[Zel57] I. B. Zeldovich, Sov. Phys. JETP **6** (1957), 1184.

[Zhu00] S.-L. Zhu et al., Phys Rev. D **62** (2000), 033008.